



HAL
open science

Structural and chemical characterization of single Co-implanted ZnO nanowires by a hard X-ray nanoprobe

Manh-Hung Chu

► **To cite this version:**

Manh-Hung Chu. Structural and chemical characterization of single Co-implanted ZnO nanowires by a hard X-ray nanoprobe. Mechanics of materials [physics.class-ph]. Université de Grenoble, 2014. English. NNT : 2014GRENY016 . tel-01558381

HAL Id: tel-01558381

<https://theses.hal.science/tel-01558381>

Submitted on 7 Jul 2017

HAL is a multi-disciplinary open access archive for the deposit and dissemination of scientific research documents, whether they are published or not. The documents may come from teaching and research institutions in France or abroad, or from public or private research centers.

L'archive ouverte pluridisciplinaire **HAL**, est destinée au dépôt et à la diffusion de documents scientifiques de niveau recherche, publiés ou non, émanant des établissements d'enseignement et de recherche français ou étrangers, des laboratoires publics ou privés.



UNIVERSITÉ DE GRENOBLE

THÈSE

Pour obtenir le grade de

DOCTEUR DE L'UNIVERSITÉ DE GRENOBLE

Spécialité : **Physique des Matériaux**

Arrêté ministériel : 7 août 2006

Présentée par

Manh-Hung CHU

Thèse dirigée par **Dr. Gema Martínez-Criado** et **Dr. José Baruchel**

préparée à l'**European Synchrotron Radiation Facility**
dans l'**École Doctorale de Physique de Grenoble**

Structural and Chemical Characterization of Single Co-Implanted ZnO Nanowires by a Hard X-ray Nanoprobe

Thèse soutenue publiquement le **02 Juillet 2014**
devant le jury composé de :

M. Hubert RENEVIER

Professeur, Institut polytechnique de Grenoble, Président

Mme. Angela RIZZI

Professeur, Georg August Universität Göttingen, Rapporteur

Mme. Núria GARRO

Professeur, Universitat de València, Rapporteur

M. Rolando PÉREZ ALVAREZ

Professeur, Universidad Autónoma del Estado de Morelos, Examineur

Mme. Gema MARTÍNEZ-CRIADO

Chargé de Recherche, European Synchrotron Radiation Facility, Co- Directeur de thèse

M. José BARUCHEL

Chargé de Recherche, European Synchrotron Radiation Facility, Directeur de thèse



Acknowledgements

First and foremost, I would like to thank my direct advisor Dr. Gema Martínez-Criado for her patient help and instruction with regards to both my professional and personal development. Her passion for work, insight into physics, and scientific integrity has brought to me a deep impression and taught me how a good scientist should be. I am lucky and happy to have been her student. I would like also thank to my second advisor Dr. José Baruchel. Although he did not directly guide me but his experience and suggestions were always worth for me.

I would like to thank Prof. Angela Rizzi and Prof. Núria Garro for accepting to be referees of my dissertation, as well as Prof. Hubert Renevier and Prof. Rolando Pérez Alvarez for agreeing to be a part of the jury of my thesis defense. Many thanks for your time and help devoted to carefully read my thesis. All your comments and suggestions are very valuable to improve the quality of my thesis.

Together with my direct supervisor, Dr. Jaime Segura-Ruiz also helped me a lot for performing the experiments based on the sophisticated instruments/techniques at the European Synchrotron Radiation Facility. He has also instructed me in detail to process the data and also interpretation of the results. Thank you very much Dr. Jaime Segura-Ruiz.

Many thanks to Prof. Carsten Ronning and Dr. Sebastian Geburt at University of Jena in Germany for providing me the excellent nanowire samples that were studied in this thesis. In addition, discussion with them was always interesting and useful to understand deeply into the growth of the nanowires. Therefore, the interpretation of the experimental data has been more easily and clearly. Thank you for such excellent cooperation.

I would like to thank all the staff of the beamline ID22, especially with Dr. Remi Tucoulou, Dr. Julie Villanova, and technician Sylvain Laboure for their kind help with the experimental setup. I also thank to Dr. Irina Snigireva for her willingness to help with SEM imaging and to Dr. Armando

Solé to guide and help me to solve some problems with data processing by using PyMca software.

I am grateful to the European Synchrotron Radiation Facility for beam time allocated and to the NANOWIRING Marie Curie ITN for granting me during three years of my study.

Life outside work never been boring thanks to my Vietnamese friends in Grenoble for sharing with me good moments, playing sport, and for discovering the life in France together. These are really useful for me to refresh after the hard work days.

Deeply from my heart, I acknowledge the continuous encouragement from my both families: my parent, my parent-in-law, my sisters, my sister and brothers-in-law. Special thanks to my wife Thu-Hang NGUYEN and my son Manh-Hai CHU who was born during this period of my study for their love and always beside me to support and encourage me to overcome all the difficulties in the work and the life.

Abstract

The PhD dissertation focuses on the investigation of single Co-implanted ZnO nanowires using X-ray fluorescence, X-ray absorption spectroscopy, and X-ray diffraction techniques with nanometer resolution at the beam-line ID22 of the European Synchrotron Radiation Facility. The ZnO nanowires were grown on *p*-Si (100) substrates using vapor-liquid-solid mechanism. The synthesized ZnO nanowires were doped with Co via an ion implantation process. For the first time, the combined use of these techniques allows us to study the dopant homogeneity, composition, short- and large-range structural order of individual nanowires. The nano-X-ray fluorescence results indicate the successful and homogeneous Co doping with the desired concentrations in the ZnO nanowires by an ion implantation process. The nano-X-ray absorption spectroscopy and X-ray diffraction data analyses provide new insights into the lattice distortions produced by the structural defect formation generated by the ion implantation process. These findings highlight the importance of the post-implantation thermal annealing to recover the structure of single ZnO nanowires at the nanometer length scale. Complementary micro-photoluminescence and cathodoluminescence measurements corroborate these results. In general, the methodologies used in this work open new avenues for the application of synchrotron based multi-techniques for detailed study of single semiconductor nanowires at the nanoscale.

Key words: Co-implanted ZnO, nanowires, X-ray fluorescence, X-ray absorption near edge structure, extended X-ray absorption fine structure, and X-ray diffraction.

Résumé

Ce travail de thèse porte sur l'analyse de nanofils de ZnO dopés au cobalt par implantation ionique, en utilisant la fluorescence des rayons X, la spectroscopie d'absorption des rayons X et les techniques de diffraction des rayons X à l'échelle nanométrique sur la ligne de lumière ID22 de l'Installation Européenne de Rayonnement Synchrotron. Les nanofils sont obtenus par croissance catalysée sur des substrats de *p*-Si (100). Les nanofils de ZnO synthétisés ont été dopés avec du cobalt par d'implantation ionique. Pour la première fois, l'utilisation combinée des techniques de caractérisation par rayons X citées ci-dessus nous permet d'étudier l'homogénéité de la distribution des dopants, la composition, ainsi que l'ordre structural à courte et grande distance de nanofils individuels. Les résultats de la nano-fluorescence des rayons X indiquent que le dopage au cobalt par implantation ionique dans les nanofils de ZnO est homogène, avec les concentrations désirées. La spectroscopie d'absorption de rayons X et l'analyse des données de diffraction de rayons X fournissent de nouvelles informations sur la distorsion du réseau cristallin produite par l'introduction de défauts structuraux par le processus d'implantation ionique. Ces résultats soulignent l'importance du recuit thermique après l'implantation pour récupérer la structure des nanofils de ZnO à l'échelle du nanomètre. Les mesures complémentaires de microphotoluminescence et cathodo-luminescence corroborent ces résultats. En conclusion, les méthodes utilisées dans cette thèse ouvrent de nouvelles voies pour l'application de mesures multi-techniques basées sur le rayonnement synchrotron pour l'étude détaillée des nanofils semi-conducteurs à l'échelle nanométrique.

Mots clés: ZnO dopé au cobalt, nanofils, fluorescence des rayons X, Spectroscopie d'absorption des rayons X: XANES, EXAFS, diffraction des rayons X.

List of Acronyms

CL: Cathodoluminescence

CCD: Charge-Coupled Device

EXAFS: Extended X-ray Absorption Fine Structure

FWHM: Full Width at Half Maximum

KB: Kirkpatrick-Baez

LDA: Local Density Approximation

Linac: Linear accelerator

MBE: Molecular Beam Epitaxy

MDL: Minimum Detection Limit

NWs: Nanowires

PL: Photoluminescence

PyMCA: Python MultiChannel Analyzer

SEM: Scanning Electron Microscopy

SRM: Standard Reference Material

SR: Synchrotron Radiation

TEM: Transmission Electron Microscopy

VLS: Vapor-Liquid-Solid

XANES: X-ray Absorption Near Edge Structure

XAS: X-ray Absorption Spectroscopy

XBIC: X-ray Beam Induced Current

XEOL: X-ray Excited Optical Luminescence

XRD: X-Ray Diffraction

XRF: X-Ray Fluorescence

0. LIST OF ACRONYMS

Contents

List of Acronyms	vii
I Overview	1
1 Introduction	3
1.1 Semiconductor nanowires	3
1.1.1 ZnO nanowires	4
1.1.2 Co-implanted ZnO nanowires	7
1.1.3 InGaN nanowires	9
1.2 Sample synthesis	10
1.2.1 Growth of ZnO nanowires	10
1.2.2 Ion implantation process	11
1.2.3 Growth of InGaN nanowires	12
1.3 Synchrotron nanoprobe	12
1.3.1 Synchrotron radiation	12
1.3.2 X-ray nanofocusing optics	14
1.3.3 Interaction of X-rays with matter	17
1.3.4 X-ray fluorescence	18
1.3.5 X-ray absorption spectroscopy	28
1.3.6 X-ray diffraction	34
1.4 Complementary characterization tools	37
1.4.1 Scanning electron microscopy	37
1.4.2 Transmission electron microscopy	37
1.4.3 Optical characterization	38
1.5 Key challenges and scientific goals	39

CONTENTS

2	Conclusions and Perspectives	43
2.1	Conclusions	43
2.2	Perspectives	44
	References	49
II	Dissertation related papers	65
3	Synchrotron fluorescence nanoimaging of a single Co-implanted ZnO nanowire	67
4	Nano-X-ray absorption spectroscopy of single Co-implanted ZnO nanowires	71
5	Local lattice distortions in single Co-implanted ZnO nanowires	79
6	Structural order in single Co-implanted ZnO nanowires	85
7	Nano-X-ray diffraction study of single Co-implanted ZnO nanowires	91
8	Intense intra-$3d$ luminescence and waveguide properties of single Co-doped ZnO nanowires	97
A	Synchrotron nanoimaging of single In-rich InGaN nanowires	103
B	Radial composition of single InGaN nanowires: a combined study by EDX, Raman spectroscopy, and X-ray diffraction	109

Part I

Overview

1

Introduction

This chapter presents some general background on the topics covered in this thesis, including the basic material properties of ZnO NWs and more specifically background information on the Co *3d*-impurities in ZnO NWs, as well as InGaN NWs. In addition, the chapter provides briefly the background and principles of several synchrotron based techniques such as X-ray fluorescence, X-ray absorption spectroscopy and X-ray diffraction, which are primary characterization tools used in the work. Some information about the instrumentation and setup used for the complementary optical and structural characterizations are also included. The end of the chapter describes some key challenges and scientific goals achieved in this thesis.

1.1 Semiconductor nanowires

Semiconductor NWs are quasi-one-dimensional structures with diameters typically in the range of tens and hundreds of nanometers, and lengths in the range from a few to tens of microns. They offer unique advantages compared to the semiconductor bulk. First, the diameters can set the radial dimension of these structures at the characteristic length scale of various fundamental solid state phenomena: the exciton Bohr radius, critical size of magnetic domains, exciton diffusion length, and others [1–3]. As a consequence, the physical properties of semiconductors change significantly within the NWs [1]. Second, their large surface to volume ratio enhances their interaction with the environment, turning them into optimal chemical and biological sensors [1, 4]. Finally, their anisotropic geometry makes their optical and electrical properties drastically dependent on their orientation, allowing their use as polarization-sensitive devices [5–7]. Therefore, semiconductor NWs have been intensively investigated for a broad range of potential applications, including electronic

1. INTRODUCTION

(diodes, field effect transistor, logic circuits) [8–12], energy (solar cell, thermoelectric generators) [1, 13], magnetic (spintronic, memory) [14–16], optoelectronic devices [17, 18], and sensors [19, 20]. As a result, the number of semiconductor NWs related publications has rapidly increased during past two decades. In particular, most of the activities and developments on the semiconductor NWs related topics (growth, NWs based devices, applications, and so on) have happened in the last ten years [21]. But, to date most NWs applications rely on the ability not only to grow, but also to characterize structurally, optically and electronically individual and collections of NWs, although it is rather difficult to find single probes covering simultaneously all of the above properties. For these reasons, this dissertation is devoted to the study of single NWs using a hard X-ray nanoprobe.

1.1.1 ZnO nanowires

Among semiconductor NWs, ZnO NWs are one of the most attractive materials due to the wide band gap energy of 3.37 eV that is suitable for short wavelength optoelectronic applications [22]. The large exciton binding energy of 60 meV [22] is higher than the thermal energy at room temperature (26 meV), which allows intense excitonic light emission in the near ultra-violet region at room temperature [23]. Therefore, ZnO NWs have attracted much attention for light emitting diodes and photonic waveguides [24–27]. Within the NW lasing application, an evidence of the transition from amplified spontaneous emission to laser oscillations in optically pumped single ZnO NWs was observed at room temperature [28]. However, it has been shown a high lasing threshold ($10 - 300 \text{ kWcm}^{-2}$), that limits the development of the ZnO NW based lasing device applications [29]. The incorporation of optical active *3d*-ions into the ZnO NWs is expected to further lower lasing threshold, as well as to obtain intense intra *3d*-luminescence in the NWs. More details about this subject are presented in following sections.

In order to ground the main results obtained in this thesis, a review of some of the most important structural and optical properties of ZnO is described.

Crystal structure

ZnO is a direct II-VI semiconductor, which crystallizes in the wurtzite structure at ambient pressure and room temperature as shown in Figure 1.1 [30]. This hexagonal structure belongs to the space group $P6_3mc$ with lattice parameters $a = b = 3.25 \text{ \AA}$ and $c = 5.21 \text{ \AA}$ [31]. Each Zn ion is surrounded by four oxygen anions at the

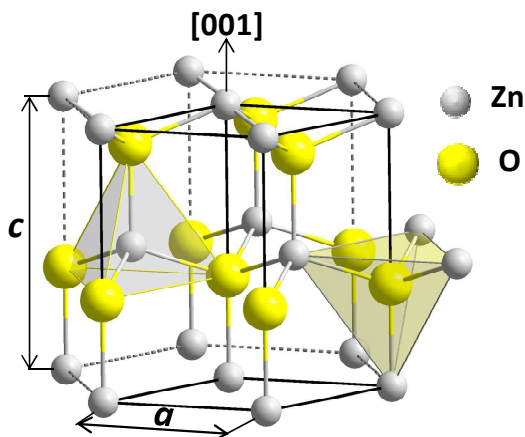


Figure 1.1: The wurtzite crystal structure of ZnO, showing the tetrahedral coordination of a Zn atom with four O atoms and viceversa (Figure adapted from Ref. [30]).

corner of a tetrahedron, and viceversa (see Figure 1.1). This tetrahedral coordination in ZnO forms a noncentrosymmetric structure with polar symmetry along the hexagonal axis, which is not only responsible for the characteristic piezoelectricity and spontaneous polarization, but also plays a key role in the crystal growth and defect generation in ZnO [22]. The tetrahedral coordinated bond of this compound is formed by sp^3 -hybrid orbitals with covalent bonding character. However, the Zn-O bond also possesses very strong ionic character, and therefore ZnO lies on the borderline between being classed as a covalent and ionic compound.

Electronic band structure

The knowledge of the electronic band structure is crucial for understanding the physical properties and device applications of semiconductors. So far several theoretical methods have been applied to calculate the band structure of ZnO [31–35]. Figure 1.2 (a) shows representative results of the electronic band structure calculated using the LDA, incorporating atomic self-interaction corrected pseudopotentials to accurately account for the Zn $3d$ electrons [32]. The figure shows that the valence band maxima and the conduction band minima were obtained at Γ point $k = 0$, which indicates that ZnO is a direct band gap semiconductor. The bottom bands around -9 eV represent Zn $3d$ levels. The next six bands from -5 eV to 0 eV represent O $2p$ bonding states. Finally, the first two conduction band states correspond to Zn $4s$ levels. The band gap determined from this method is 3.77 eV, which is in much better agreement with experiments compared to other methods (e.g., standard LDA calculation gives value of 0.23 eV) [22, 32]. It is also worth to mention that the ZnO valence band is

1. INTRODUCTION

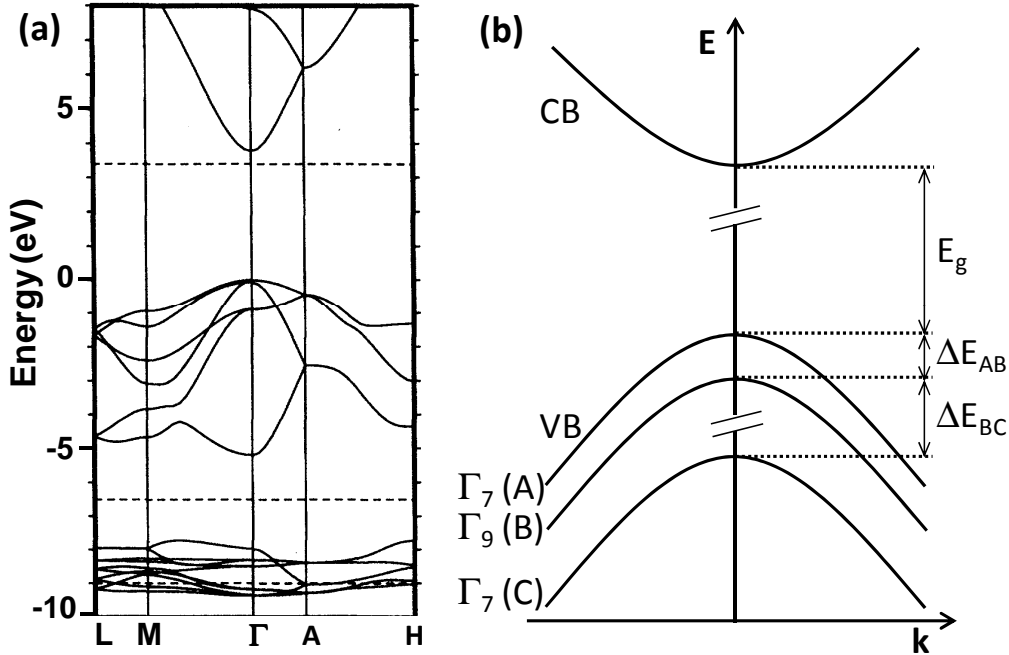


Figure 1.2: (a) The LDA band structure of bulk wurtzite ZnO calculated using dominant atomic self-interaction-corrected pseudopotentials. Image adapted with permission from Ref. [32]. (b) Representation of the conduction and spin-orbit splitting of the valence band of ZnO into three subband states A, B, C at Γ point.

split by the crystal field and spin orbit interaction into three states named A, B and C under the wurtzite symmetry, as shown in Figure 1.2 (b). The A and C subbands are known to have Γ_7 symmetry, while the middle band B presents Γ_9 symmetry [36]. The band gap has a temperature dependence up to 300K and shrinks with increasing temperature given by the relationship [37]:

$$E_g(T) = E_g(T = 0) - \frac{5.5 \times 10^{-4} T^2}{900 - T}, \quad (1.1)$$

where $E_g(T = 0)$ is close to zero.

Optical properties of ZnO

The optical properties of semiconductor are linked to both intrinsic and extrinsic effects [38, 39]. The electronic transitions between the conduction band and valence band are usually treated as intrinsic optical transitions, in which the excitonic effects due to the Coulomb interaction between electrons and holes plays a crucial role. For ZnO the binding energy of the excitons (60 meV) is larger than the thermal energy at room temperature ($k_B T \approx 26$ meV), therefore allowing the observation of the excitonic

emissions even at the room temperature. On the other hand, extrinsic properties are related to the electronic states created in the bandgap by either dopants, impurities or point defects and complexes in ZnO, which usually influence both optical absorption and emission processes. For instance, the excitons can be bound to neutral or charged donors and acceptors, called bound excitons. The electronic states of these bound excitons strongly depend on the band structure. For a shallow neutral donor bound exciton, for instance, the two electrons in the bound exciton state are assumed to pair off into a two-electron state with zero spin. The additional hole is then weakly bound in the net hole-attractive Coulomb potential set up by this bound two-electron aggregate. Similarly, neutral shallow acceptor bound excitons are expected to have a two-hole state derived from the topmost valence band and one electron interaction [39]. Other extrinsic transitions could be seen in the optical spectra such as free-to-bound (electron-acceptor) and bound-to-bound (donor-acceptor).

1.1.2 Co-implanted ZnO nanowires

Doping of semiconductor NWs is a critical step to produce materials with novel properties and functionalities for new devices [40, 41]. In the context of spintronic nanodevices, transition metals doped ZnO NWs have attracted much attention due to their predicted ferromagnetic behavior at room temperature [42, 43]. In addition to the attractive magnetic properties, Co doped ZnO NWs have promising optical properties because of Co *3d* intra-shell transitions for future optoelectronic applications [44]. The incorporation of cobalt into the ZnO host crystal results in a multiple splitting of the degenerated *3d*-shell states of the free ion as shown in Figure 1.3 [45, 46]. The resulting electronic structure of Co²⁺ in ZnO can be approximated by the Hamiltonian [47]:

$$H = H_{free\ ion} + H_{CF} + H_{SO} + H_v + H_{JT}, \quad (1.2)$$

where the perturbation terms $H_{free\ ion}$ is the Hamiltonian of free ion with multi-electron interaction according to the Hund's rule, H_{CF} is the Hamiltonian of the crystal field (Stark effect), H_{SO} is the Hamiltonian of spin-orbit interaction, H_v and H_{JT} are the Hamiltonian of vibrational contributions and electron-phonon coupling namely Jahn-Teller coupling, respectively. However, the electronic structure is mainly affected by the Stark effect of the crystal field and the spin-orbit interaction. Vibrational contributions and Jahn-Teller interactions play minor roles in the electronic structure of the free ions as the Co²⁺ ions are stabilized by the axial crystal field components in ZnO [45].

1. INTRODUCTION

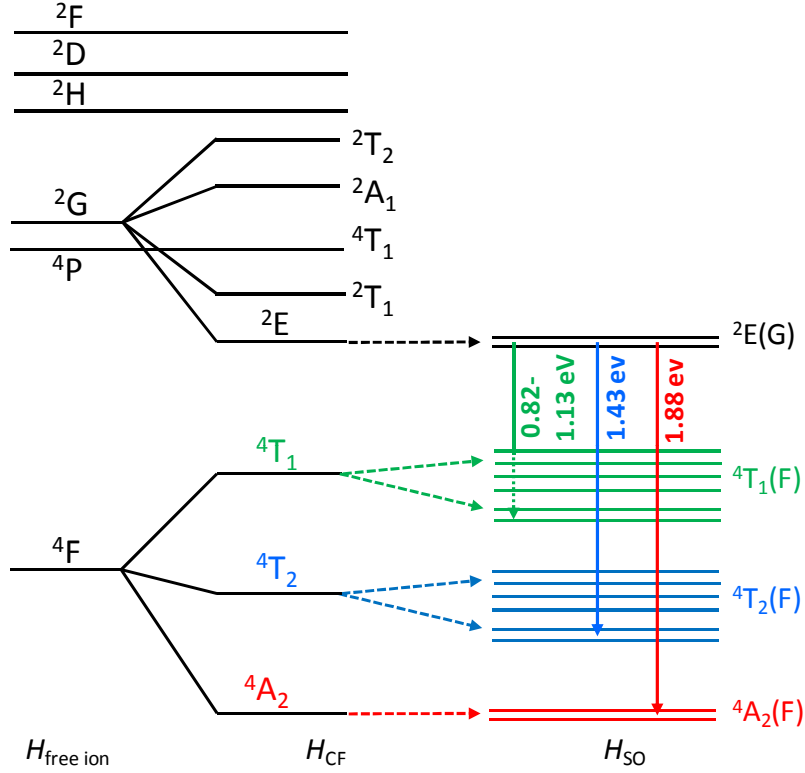


Figure 1.3: Energy levels of a $\text{Co}^{2+} 3d^7$ ion split under the influence of the ZnO crystal field (showed by H_{CF} term) and the spin-orbit interaction (H_{SO}). Several common Co^{2+} intra- $3d^7$ emissions are also shown from the visible to near infrared range. The energy differences are not to scale (Figure adapted from Ref. [46, 48]).

In Figure 1.3, the Co^{2+} free ion levels consist of the ^4F ground state followed by the ^4P as well as the ^2G excited state and ^2H , ^2D , ^2F states. We shall concentrate primarily on first three free-ion levels. Due to the Stark effect of the tetrahedral coordinated crystal field (T_d symmetry), the free-ion ground state ^4F splits into the $^4\text{T}_1(\text{F})$ term at 0.78 – 1.13 eV and the $^4\text{T}_2(\text{F})$ term at 0.45 – 0.55 eV above the $^4\text{A}_2(\text{F})$ ground term. The crystal field states further split by spin-orbit coupling as sketched in Figure 1.3 [45, 46, 48, 49]. The ^4P is not split by the crystal field, but transforms into $^4\text{T}_1(\text{P})$, which degenerates under the influence of the spin-orbit interaction into at least six sublevels at 2.01 – 2.12 eV above the ground term (not included in Figure) [45, 46]. The ^2G excited state splits into the four levels under the influence of the tetragonal crystal field. Namely, the $^2\text{E}(\text{G})$ level at 1.88 eV and the $^2\text{T}_1(\text{G})$ at 1.93 – 1.98 eV are below the $^4\text{T}_1(\text{P})$ level, while the $^2\text{A}_1(\text{G})$ at 2.19 eV and the $^2\text{T}_2(\text{G})$ at 2.24 – 2.36 eV are located above. These states are also split by the spin-orbit interaction except the $^2\text{A}_1(\text{G})$ state [48, 49].

As a result, transitions between these $3d$ -shell states become partly allowed and show very sharp lines in PL spectrum [45–47]. The common Co^{2+} emissions in ZnO are detected in the visible to near infrared range, which could be assigned to the different transitions indicated in Figure 1.3. For instance, the ${}^2\text{E}(\text{G})$ to ${}^4\text{A}_2(\text{F})$ transition creates the Co^{2+} emission at $1.74 - 1.88$ eV, while the emission at $0.82 - 1.13$ eV is assigned to the ${}^2\text{E}(\text{G})$ to ${}^4\text{T}_1(\text{F})$ transition [45, 48].

1.1.3 InGaN nanowires

In this dissertation, apart from the main topic on Co-implanted ZnO NWs, we have also characterized $\text{In}_x\text{Ga}_{1-x}\text{N}$ NWs by synchrotron hard X-ray nanoprobe. Thus, a brief introduction is presented to review some unique properties of the $\text{In}_x\text{Ga}_{1-x}\text{N}$ NWs, as well as the motivation of the study.

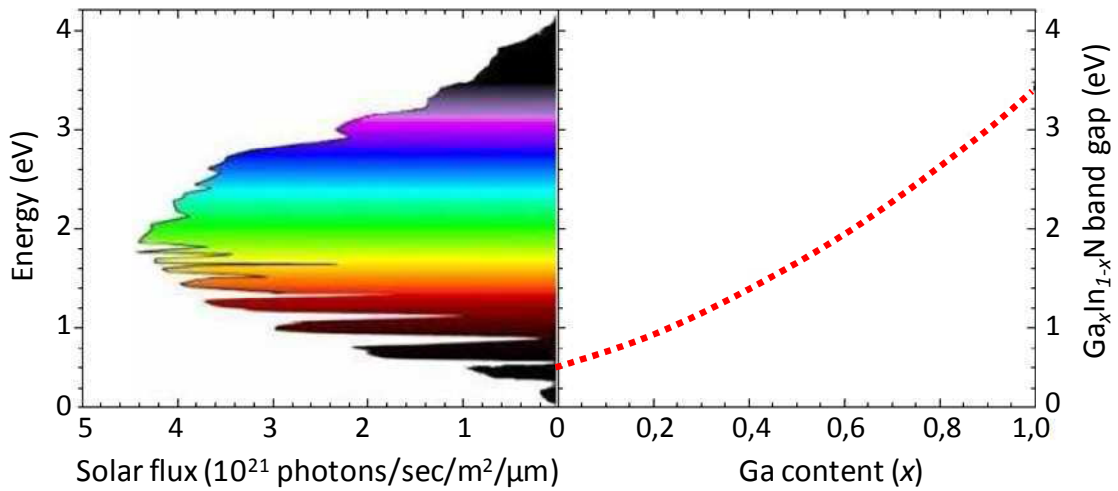


Figure 1.4: The solar spectrum represents the intensity and spectral distribution of incoming sunlight for a given location and atmospheric conditions on the earth (left panel). Band-gap energies of the $\text{Ga}_x\text{In}_{1-x}\text{N}$ alloy as a function of Ga content (right panel), which cover the greater part of the solar spectrum (Figure adapted from Ref. [50]).

InN and GaN have band gap energies of about 0.7 eV and 3.4 eV [51], respectively. For a ternary alloy $\text{In}_x\text{Ga}_{1-x}\text{N}$, if x varies from 0 to 1, the energy of the optical emission can be changed from the near-ultraviolet to the near-infrared region (covering most part of the solar spectrum as shown in Figure 1.4), which could be exploited in high-efficiency photovoltaics [52, 53] and color-tunable-light emitting/laser diodes [54, 55]. In addition to these properties, the NW geometry offers additional advantages to enhance the performance of these devices [56–59]: (1) a decoupling of the absorption axis from the carrier collection axis; (2) photonic effects that can

1. INTRODUCTION

enable enhanced light trapping due to nanoscale optical index changes, which cause scattering and reduced reflection; (3) elastic strain relief, allowing higher indium mole fractions and lower defect concentrations. As a consequence, the growth of $\text{In}_x\text{Ga}_{1-x}\text{N}$ NWs has attracted much attention in recent years, and $\text{In}_x\text{Ga}_{1-x}\text{N}$ NWs have been synthesized successfully by MBE [60, 61], low-temperature halide chemical vapour deposition technique [62], and metal-organic chemical vapor deposition [63]. However, these NWs suffer from compositional modulation for high In content and are not well oriented. Thus, the investigation of these individual NWs is crucial to understand the mechanism driving its growth and the resulting properties that could be responsible for performance of the nanodevices. Despite there are few reports on characterization of individual $\text{In}_x\text{Ga}_{1-x}\text{N}$ NWs at the nanometer length scale, which reveal Ga and In element segregation along the axial direction of single NWs [64], some questions remain: How is the variation of the alloy composition along the radius of single $\text{In}_x\text{Ga}_{1-x}\text{N}$ NWs? How does the elemental modulation affect to the local and long-range atomic structure of the single $\text{In}_x\text{Ga}_{1-x}\text{N}$ NWs? These issues are addressed in the annex 1 and 2 of this dissertation using synchrotron hard X-ray nanoprobe.

1.2 Sample synthesis

Although the crystal growth and doping of ZnO NWs and InGaN NWs were not carried out by the candidate, but by the group of Prof. Carsten Ronning at Jena University, and Prof. Angela Rizzi at Goettingen University, respectively, some basic information about their synthesis are described in this section.

1.2.1 Growth of ZnO nanowires

The VLS is an one-dimensional crystal growth mechanism that is assisted by a metal catalyst [65]. It results in the creation of whiskers, rods, and wires [65]. One-dimensional crystal growth was initially developed nearly 50 years ago for Si whisker and the growth mechanism was suggested for wider use by Wagner in 1964 [66]. Using VLS process, substrates covered with the catalyst (typically gold as thin film with less than 10 nm thickness or colloid) are heated up to a temperature between the melting point of source material and the one for the catalyst. The catalyst becomes liquid and forms nanometer sized droplets. Source material under gas phase form is preferentially absorbed at the surface of the catalyst droplet and forms the eutectic solution. The source material then nucleates as solid phase, typically by hetero-nucleation at

the interface between catalyst droplet and growth substrate. The solubility of the catalyst is typically very low, therefore nearly no catalyst is incorporated, but remains on top of the rods or wires. The diameter is determined approximately by the size of the catalyst droplet, whereas the length can be controlled by the time of source material vapour is supplied.

For the VLS synthesis of the ZnO NWs on *p*-Si (100) substrate, ZnO powder (99.9 % purity) as a source material was put into an alumina boat and placed at the centre of a tube furnace, which was heated up at a rate of 200 °C/hour. At 600 °C, argon gas flow of 50 sccm with a pressure of 150 mbar was switched on, the gas stream flowed over the substrate first and passing through the source material to prevent the contamination and oxidation of the substrate. The substrate covered with a 5 nm thick Au film was put in a colder region downstream the furnace tube. After reached the temperature of 1350 °C at the center of the furnace where the ZnO powder source was put, while the substrate temperature was around 950 – 1100 °C, the Ar gas flow was switched to the growth direction (from source powder to substrate). Finally, ZnO NWs were grown on the Si substrate during 30 minutes. The synthesized ZnO NWs possessed a spaghetti-type morphology.

1.2.2 Ion implantation process

In order to obtain a successful Co doping into NWs by an ion implantation process, the group of Prof. Carsten Ronning at the Solid State Institute of the University of Jena needed to adjust the Co ion energy in order to match the ion range with the NW diameter. Furthermore, the Co ion fluence must be set for the desired doping concentration. These ion energy and fluence were simulated by the Monte-Carlo code *iradina* [67]. This program simulates the transport of ions through a target, consisting of a number of cells as well as taking into account the three dimensional NW morphology [67]. From the simulation results, a combination of ion energies from 60 to 300 keV and a Co ion fluence of $1.57 \times 10^{16} \text{ cm}^{-2}$ were obtained to have a homogeneous doping concentration in the range of 0.2 – 0.9 at. %.

Co ion beam doping of the ZnO NWs was performed at room and high temperature for different studies, using the 400 keV ion implanter ROMEIO [48]. The ion energy and fluence applied were the values obtained from the simulation. The ion beam current was kept below $3 \mu\text{A}/\text{cm}^2$ to avoid any damage of NWs by heating. Due to the different angles between the ion beam and the randomly aligned NWs, each implanted NW exhibits slightly different concentrations. Additionally, some

1. INTRODUCTION

wires may be affected by shadowing effects due to an overlapping of NWs during the implantation process. For characterization of single NWs, the nanowire ensemble was transferred to clean Si substrates via an imprint technique in order to obtain isolated NWs [68]. For comparison, some ZnO NWs implanted with Co at room temperature were annealed at 750 °C in air for four hours (labeled annealed ZnO:Co NWs), and others do not undergo the thermal treatment (labeled as-implanted ZnO:Co NWs). Some ZnO NWs were implanted with Co ion at high temperature (700 °C) and followed a thermal annealing at 750 °C in air for four hours [labeled high temperature (HT) implanted ZnO].

1.2.3 Growth of InGaN nanowires

$\text{In}_x\text{Ga}_{1-x}\text{N}$ NWs were grown on bare n -Si (111) substrates using a Veeco GEN II MBE-system in the group of Prof. Angela Rizzi at the Goettingen University [69]. The n -Si (111) substrate was cleaned with acetone and isopropanol in an ultrasonic bath for two min before mounting. Afterwards, the substrate was outgassed *in-situ* at 600 °C for 10 hours and at 1000 °C for 40 minutes. The resulting 7×7 reconstruction of the surface was monitored by reflection high-energy electron diffraction and was used as an indication of an oxygen-free Si surface. In order to limit the nitridation of the substrate, the plasma was turned on for five minutes before the growth [70]. Then, the NWs were grown on such substrate under nitrogen rich conditions required to obtain a NW morphology, with a growth time of 200 minutes. The substrate temperature (determined by pyrometry) and the Ga/(Ga + In) flux ratio used during the growth were 462 °C and 0.07, respectively [69]. For the synchrotron characterization, single NWs were also transferred to an Al-covered sapphire substrate, having a gold grid prepared by lithography [69].

1.3 Synchrotron nanoprobe

1.3.1 Synchrotron radiation

SR is an electromagnetic radiation emitted when electrons, moving at a relativistic speed, i.e., close to the velocity of light, are forced to change direction by a magnetic field [71]. Namely, the SR is emitted in a narrow cone in the forward direction, at a tangent to the electron's orbit. SR facilities typically consist of an injection system (an electron gun, linac, and booster ring), a storage ring (bending magnets, insertion devices, radio frequency cavities, and focusing magnets) and beamlines as

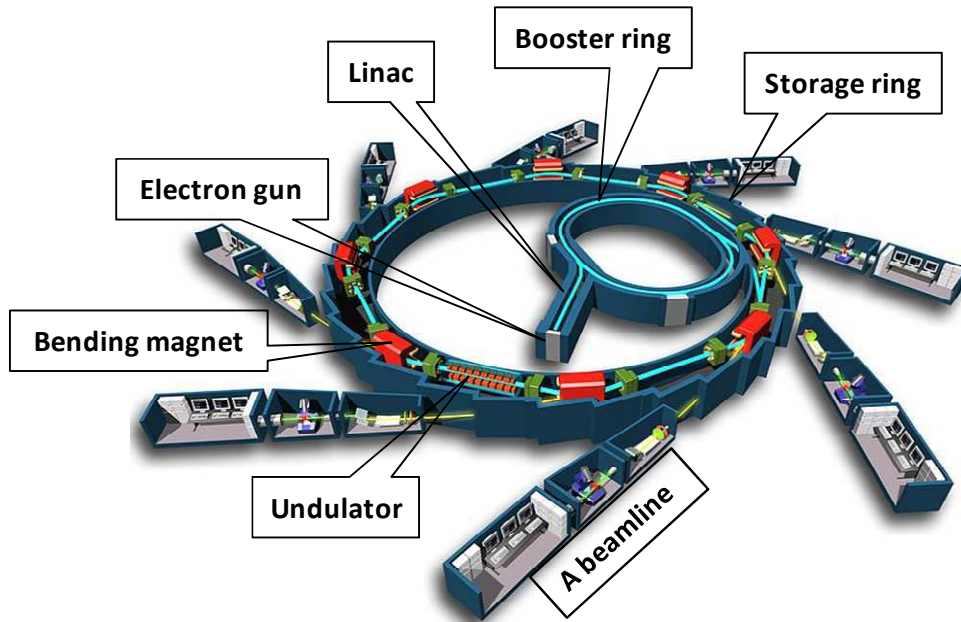


Figure 1.5: Schematic of a synchrotron facility which typically consists of an injection system, a storage ring, and beamlines. The injection system includes an electron gun, a linac, and a booster. The storage ring consists of radio frequency cavities, bending magnets, and undulators or wigglers (Figure adapted from Ref. [72]).

shown in Figure 1.5 [73]. In the injection system, electrons are produced first by an electron gun. These electrons are packed in “bunches” and accelerated to approach the speed of light by a linac. The electrons are then transferred to a booster ring, where they are accelerated to reach final energy before entering into the storage ring. At ESRF, the electrons are accelerated to reach a nominal energy of 6 billion electronvolts (GeV) [73]. In the storage ring, the electrons travel for hours close to the speed of light within an evacuated tube at extremely low pressure (around 10^{-9} mbar at ESRF). As they travel round the ring, they pass through different types of magnets, mainly bending magnets, undulators or wigglers. SR is emitted when an electron received centripetal force in the magnetic field of the bending magnets. This light is emitted tangentially to the curved electron beam and collimated into a narrow, intense beam. However, a higher intense synchrotron light is produced by insertion devices such as undulators or wigglers which are made up of a series of small magnets with alternating polarity, the base of of third generation SR sources [73, 74]. The storage ring also consists of radio-frequency cavities and focusing magnets which are used to restore the energy of electron lost because of the emission of SR, and keep the electron beam size as small as possible [73]. The X-ray beam produced by a synchrotron facility has a number of unique properties. These include [75–79]:

1. INTRODUCTION

- High brilliance ($10^{21} \text{phot/s}/0.1\% \text{band width}/\text{mrad}^2/\text{mm}^2$): It can be hundred of thousands of times more intense than that from conventional X-ray sources, allowing trace-element sensitivity study.

- Energy tunability (ranging from infrared lights to gamma rays).

- High degree of polarization: The synchrotron emits highly polarized radiation, which can be linear, circular or elliptical.

- Timing structure: Pulses emitted are typically less than a nanosecond, enabling time-resolved studies.

- Low emittance [HxV: 4nm x 3pm (uniform filling mode at ESRF)].

- High collimation (small angular divergence of the beam).

Taking the unique properties of the synchrotron radiation, and the multiple photon-matter interactions, the use of nanometre-sized X-ray beam provides further advantages [80, 81]: i) high spatial resolution (around $50 \times 50 \text{ nm}^2$) which allows to investigate elemental composition, local chemistry, local structure, and defects of small or heterogeneous samples (e.g., nanostructures, quantum dots) or objects with clusters or nanoagregates; ii) deeper information depths that allow to characterize thick samples and buried sample volumes in their natural or extreme environments, without complex sample preparation procedures; iii) site- and orbital-selectivity, with simultaneous access to K absorption edges and X-ray fluorescence emission lines of medium, light and heavy elements.

1.3.2 X-ray nanofocusing optics

Along with the development of third generation SR sources providing higher brilliance ($10^{21} \text{phot/s}/0.1\% \text{band width}/\text{mrad}^2/\text{mm}^2$) [76, 77], and lower emittances (HxV: 4nm x 3pm) [76], the improvement of X-ray focusing optics has played an important role in order to reduce the X-ray beam size from millimeters down to several tens of nanometers. As mentioned in Section 1.3.1, the use of nanometer-sized X-ray beams presents unique advantages. Nowadays, there are many focusing devices available to focus the X-ray beam down to nanometer length scale such as KB mirrors [82, 83], compound refractive lenses [84, 85], Fresnel zone plates [86, 87], X-ray capillary optics [88, 89], multilayer Laue lens [90, 91], adiabatically focusing lens [92], and Kinoform Fresnel lenses [93]. The use of each device depends on the application, for example, the KB is not only focused the X-ray beam down to few nanometers (7 nm at 20 keV), but it is also achromatic [80, 83]. These characteristics are critical for X-ray absorption spectroscopy and the study of nanostructures. In this thesis,

1.3 Synchrotron nanoprobe

therefore, a hard X-ray beam was focused using KB multilayer coated Si mirrors, which are described in more detail later.

Nevertheless, it is worth to mention some basic concepts. For an X-ray lens, the diffraction limited resolution is estimated by the Rayleigh's criterion [94]:

$$S_{DL} = \alpha \frac{\lambda}{NA}, \quad (1.3)$$

where λ is the wavelength of X-ray beam, α equals 0.44 for the two-dimensional focusing by a flat rectangular lens [82], while a round lens gives α value of 0.61 [80]. $NA = n \sin \theta$ is the numerical aperture with an opening angle 2θ and n is the complex index of refraction expressed by:

$$n = 1 - \delta + i\beta, \quad (1.4)$$

where δ describes the dispersion in the material, having the value of around 10^{-8} in air and around 10^{-5} in solid materials [94]. β describes the absorption, which is usually much smaller than δ . So, the n index is smaller than the unity due to the weak interaction of X-ray beam with the material. The low achievable numerical aperture, therefore, is still a drawback in X-ray optics.

In addition to the diffraction limit, the minimum achievable spot size is limited by the geometrical source demagnification, given by [82]:

$$S_G = S \frac{q}{p}, \quad (1.5)$$

where S is the size of the source, p is the distance from the source to the focusing device, and q distance from the focusing element to the focal spot. This equation implies that the smaller spot size can be obtained by increasing the distance between the source and focusing element.

Apart from the these two factors: the diffraction limit S_{DL} and geometrical source demagnification S_G , we have to take into account imperfections of real optics (S_I) that is also affected the achievable beam size. These imperfections are aberrations, mirror shape errors, nonuniform areas, as well as further experimental issues such as vibrations, drifts, etc. [80, 95, 96]. Therefore, the FWHM limit of the resolution (S) is a combination of these three factors:

$$S = \sqrt{S_{DL}^2 + S_G^2 + S_I^2}. \quad (1.6)$$

1. INTRODUCTION

Kirkpatrick-Baez mirrors

KB optics [97] consists of two orthogonal placed mirrors as shown in Figure 1.6. The first mirror focuses the X-ray beam in the vertical plane, while the second one in the horizontal plane. The focusing principle is based on the total external reflection (single layer) or on the Bragg law fulfilled by multilayer coatings deposited on the mirrors [82]. The total external reflection can occur when the grazing angle is smaller than a critical angle $\theta_c < \sqrt{\delta}$, where δ is the decrement of the index of refraction. Usually, the mirror surface is coated with a heavy material in order to obtain a larger electron density, which produces a larger critical angle for total reflection [80].

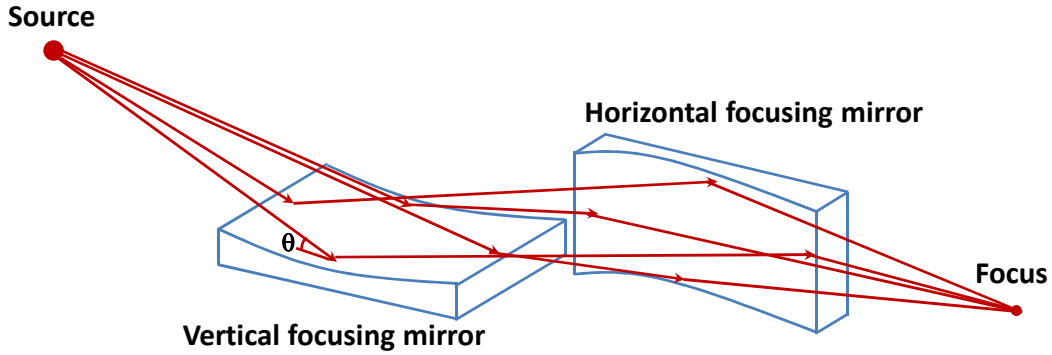


Figure 1.6: Schematic of a Kirkpatrick-Baez mirror system. Two orthogonally placed mirrors focus the incident beam vertically and horizontally. θ is an angle between the incident beam and the mirror.

The generic lens shape for a point-to-point focusing geometry is an ellipse if the phase shifts on reflection is neglected [82]. In the case of a single elliptic total reflection mirror, the grazing angle is limited by the critical angle of total external reflection θ_c expressed as [82]:

$$\sin \theta_c = \sqrt{2\delta}, \quad (1.7)$$

since δ is very small, so that the aperture 2θ is very limited. An estimation of the diffraction limit of a total reflection mirror system [$S_{DL}(TRM)$] is shown by assuming a full opening of up to half of critical angle $4\theta \leq \theta_c$ [82]:

$$S_{DL}(TRM) \approx \frac{1.76\lambda}{\sqrt{2\delta}} = 1.76\sqrt{\frac{\pi}{r_0\rho_e}}, \quad (1.8)$$

where r_0 is the classical electron radius, λ is the wavelength of the radiation, and ρ_e is the electron density of the material. Thus, the focusing power of a total reflection mirror strongly depends on the material properties [82].

The multilayers, on the other hand, consist of different layers of low and high refractive index materials [98]. If the period Λ of the multilayer structure satisfies the modified Bragg equation

$$\Lambda = \frac{\lambda}{2\sqrt{n^2 - \cos^2 \theta}}, \quad (1.9)$$

at any point along the mirror, constructive interference will happen, improving the reflectivity up to values that can reach 90% or more [98]. Therefore, the Bragg angle of a multilayer coated mirror can be several times larger than the critical angle of a total reflection mirror. An estimation of the diffraction limit of the multilayer mirror [$S_{DL}(RML)$] obtained by assuming $\theta \approx \lambda/2\Lambda$, is

$$S_{DL}(RML) \approx \frac{0.88}{1/\Lambda_2 - 1/\Lambda_1}, \quad (1.10)$$

where, $\Lambda_{1,2}$ indicates the multilayer d -spacings at the respective edges of the mirror. The resolution is therefore limited only by the lateral d -spacing gradient of the reflective multilayers [82]. For instance, with a short period and a strong gradient, focal spots of about 5 nm full width of half maximum appear realistic.

In order to achieve a preferable spot size, the KB mirrors are bent statically or dynamically to a specific shape (elliptical shape). Recent developments in the technology of shaping, polishing, mounting, and aligning of KB mirrors have brought a focusing X-ray beam with a spot sized of less than 10 nm at 20 keV [83, 99]. One of the important advantages of these mirrors compared to the others is the achromaticity, meaning that the focal length is independent of the energy, which is critical for X-ray absorption spectroscopy. The disadvantages, on the other hand, are the low acceptance, relatively expensive, and that the mechanics for dynamical bending of the mirrors is complex.

1.3.3 Interaction of X-rays with matter

When an X-ray beam passes through matter, a fraction of the light is transmitted, while a fraction is absorbed inside the material, and a fraction is scattered away from the original path with and without loss of energy, called Compton and Rayleigh scatters, respectively, as illustrated in Figure 1.7. The intensity I_0 of the incident X-ray beam passing through a layer of thickness t (cm) and density ρ is reduced to an intensity $I(t)$ according to the *Lambert-Beer's* law [75, 100]:

$$I(t) = I_0 e^{-\mu t}, \quad (1.11)$$

1. INTRODUCTION

where μ (cm^{-1}) is the linear attenuation coefficient. It can be formulated as follows:

$$\mu = \sigma_a \frac{N_A}{A} \rho_m, \quad (1.12)$$

where σ_a is the attenuation cross section, N_A is Avogadro's number, A is the atomic weight, and ρ_m is the mass density. The attenuation coefficient can be described as the linear attenuation coefficient (Equation 1.11) and as mass attenuation coefficient (μ_m). The first one μ (cm^{-1}) is critical for X-ray optics since it quantifies the amount of X-rays absorbed per unit length and depends on the physical and chemical states of the absorber as well as on the energy of the incident photons. The second one μ_m (cm^2g^{-1}), on the other hand, quantifies how many X-ray photons are absorbed per unit mass of material [75]:

$$\mu_m = \frac{\mu}{\rho_m} = \sigma_a \frac{N_A}{A}. \quad (1.13)$$

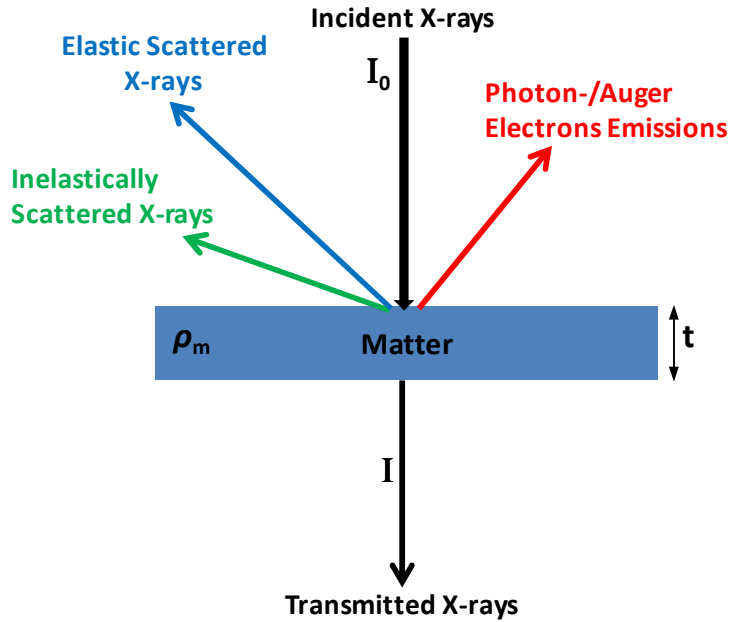


Figure 1.7: Interaction of X-ray photons with matter

1.3.4 X-ray fluorescence

Synchrotron XRF is a very useful technique for qualitative and quantitative elemental analysis of materials. Synchrotron XRF has three main advantages: non-destructive, multi-elemental and fast technique. Based on a focused X-ray beam, this method provides a high spatial resolution and low detection limits, allowing the study of very

small samples (e.g., quantum dots, nanostructures), as well as elemental traces analysis below parts per million level.

i) Basic principle of XRF

The classical model of an atom is a positively charged nucleus surrounded by negatively charged electrons which are grouped in shells or orbitals. The innermost shell is called the K-shell, followed by L-shells, M-shells etc. as one moves outwards. The L-shell has three sub-shells called L_1 , L_2 and L_3 , while M-shell has five sub-shells M_1 , M_2 ... M_5 as illustrated in Figure 1.9 [101]. Each shell contains a certain maximum number of electrons determining by the Pauli exclusion principle [102]. It is well known that each electron could be described through four following quantum numbers that uniquely define it and specify the shell it may occupy [102, 103]:

- The principal quantum number (n) describes the electron shell, or energy level of an atom. The values of $n = 1, 2, 3, \dots$ that correspond to K-shell, L-shell, M-shell,...
- The azimuthal quantum number (l) describes the subshell (angular momentum). This is related to the shape of the orbital. The value of $l = 0, 1, 2, \dots, n-1$.
- The magnetic quantum number (m_l) describes the specific orbital (or “cloud”) within that subshell, and yields the projection of the orbital angular momentum along a specified axis. The value of m_l ranges from $-l$ to l , with integer steps between them.
- The spin quantum number (m_s) describes the spin (intrinsic angular momentum) of the electron within that orbital (spin up or spin down). The value of m_s is independent of the three quantum numbers above. It has only two values: $+1/2$ or $-1/2$.

The Pauli exclusion principle states that it is impossible for two electrons of an atom to have the same values of the four quantum numbers (n, l, m_l and m_s). According to this principle, maximum numbers of electrons on each shell can be determined. For example, consider K shell, i.e. $n = 1$. The electron will have only one value of the azimuthal quantum number which is $l = 0$ and one value of the magnetic quantum number, which is $m_l = 0$ but it can have two values of m_s , either $+1/2$ or $-1/2$. Therefore, the maximum electron number of the K-shell is two electrons (first one with $n = 1, l = 0, m_l = 0$ and $m_s = +1/2$; second one with $n = 1, l = 0, m_l = 0$ and $m_s = -1/2$). Similarly, the L-, and M-shells can contain eight and 18 electrons, respectively [101, 103].

When a sample is irradiated with X-rays, the X-rays may undergo either scattering or absorption by atoms of the sample. In the case of absorption, the incident X-rays with sufficient energy will eject an electron from an inner shell of the atom, leaving a

1. INTRODUCTION

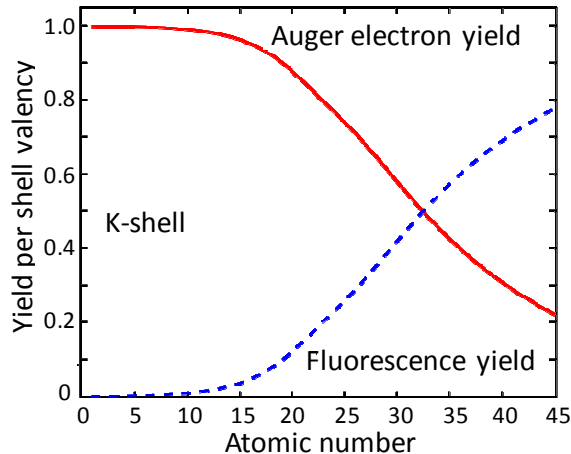


Figure 1.8: Fluorescence and Auger electron yields as a function of atomic number for K shell vacancies. Auger transitions (red curve) are more probable for lighter elements, while fluorescence yield (dotted blue curve) becomes dominant at higher atomic numbers (Figure adapted from Ref. [104]).

vacancy (hole) in the core shell. The hole state of the core shell has a finite lifetime of $\sim 10^{-15}$ sec [105, 106] and it, therefore, is refilled quickly by an electron from an outer shell. This transition from the outer shell to the inner shell occurs via two competitive processes, the X-ray fluorescence and Auger effects [100, 107]. In the X-ray fluorescence, which is subjected to selection rules, the electrons with energy E_m from the outer shell will move down to the inner shell with energy E_n to fill into the vacancies. This process will create the emission of a characteristic X-ray photon (fluorescence) with energy (E) that is the difference between two binding energy of two shells:

$$E = E_n - E_m. \quad (1.14)$$

In addition to the X-ray fluorescence emission, the transition from the outer shell to the inner shell can also induce the emission of Auger electrons via the Auger effect [104, 107]. The probability of X-ray fluorescence emission is called the fluorescence yield, while the Auger electron yield is for emission of Auger electrons. Both depend on the element's atomic number and the shell in which the vacancy occurred. The X-ray fluorescence and Auger electron yields for K-shell as a function of atomic number is shown in Figure 1.8. This figure clearly shows that the Auger effect is dominant for light elements, whereas emission of X-ray fluorescence is more likely for heavier elements [107]. Each atom has its unique characteristic X-rays spectrum dominated by the selection rules. The allowed transitions for the XRF emission induced by photoelectric effect are specified by three quantum selection rules [100, 107, 108]:

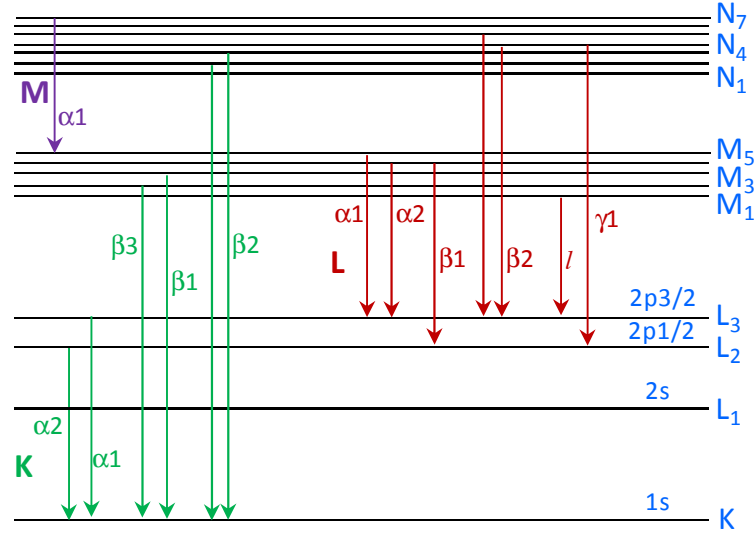


Figure 1.9: Electric-dipole allowed transitions and different X-ray fluorescence emission lines in an atom after K-shell ionization.

- $\Delta n \geq 1$ where n is the principal quantum number.
- $\Delta l = \pm 1$ where l is the azimuthal quantum number.
- $\Delta j = \pm 1$ or 0 where the quantum number j is the total momentum $j = l + s$, where s is the spin quantum number.

Based on these rules, for instance, only one type of electron transition (p -orbital \rightarrow s -orbital) is possible to fill an ionized K-shell ($1s$). Possible transitions include: $2p$ (L-shell), $3p$ (M-shell), and $4p$ (N-shell) to $1s$ (K-shell), yielding three main X-ray characteristic lines. Figure 1.9 represents the most common X-ray characteristic lines with their allowed transitions. The Greek letters in Figure 1.9 represent the nomenclature applied to the most probable electron transitions to the K, L, and M shells, and the resulting characteristic X-ray emissions. The energy of each transition (X-ray characteristic line) from an atomic level m to an atomic level n is proportional to the square of its atomic number as given by Moseley's law [100, 107]:

$$E_{mn} = R_H(Z - \sigma)^2 \left(\frac{1}{n^2} - \frac{1}{m^2} \right), \quad (1.15)$$

where R_H is the Rydberg constant relating to atomic spectra, σ is the screen constant for the repulsion correction due to other electrons in the atom, and Z is the atomic number. Every element has its own characteristic X-rays that is its fingerprint.

ii) Qualitative and quantitative XRF analysis

Qualitative analysis: Based on Moseley's law, the qualitative analysis is done using tabulated energy values of characteristic X-rays. Therefore, the existence of

1. INTRODUCTION

elements in a sample can be identified from the energy of peaks, which are present in an XRF spectrum. The assignment of the XRF lines should follow the selection rules already presented in previous section and take into account that every element may be composed by a group of X-ray lines that have certain intensity ratio. Details of the X-ray fluorescence lines are presented in Figure 1.9. The qualitative XRF analysis needs to consider also background and a number of spectral artifacts, which become specially important for trace element analysis [100, 107]. The background is mainly due to coherent and incoherent scattering of the excitation radiation by the sample. The shape can be very complex and depends both on initial shape of the excitation spectrum and on the sample composition [100]. Occurrence of some processes due to the scattering of the incoming X-rays by the sample and the emitted X-rays impacting the detector may lead to additional peaks that are not taken into account in the actual X-ray fluorescence process. Therefore, in order to evaluate the XRF spectrum correctly, the origin of these peaks needs to be defined [100, 107]:

- *Escape peaks*: Resulting from the escape of Si K photons from the detector after photoelectric absorption of the impinging X-ray photon near the edge region of Si material. Because of this process, the energy deposited in the detector equals to the difference value between the energy of the impinging X-rays and the Si K_α photons. The positions of the escape peaks are thus expected at 1.74 keV (Si K_α) below the parent peaks. The width of the escape peaks is smaller than the one of the parent peaks and corresponding to the spectrometer resolution at the energy of the escape peak. The escape fraction (f) is determined as a ratio of the number of the counts in the escape peak (N_e) over the number of detected counts from escape and parent (N_p) peaks and $f = N_e/(N_p + N_e)$ [100].

- *Sum peaks (pile-up)*: Occuring when two or more X-ray photons impact the detector at a same time. The respective electron pulse created and measured is the sum of all these X-ray energies which will lead to a characteristic line with a multiple of energy of the true X-ray fluorescence energy of the probing element. The intensity of sum peaks is count-rate dependent, and they can be reduced and virtually eliminated by performing the measurement with lower incident beam intensity.

- *Compton and Rayleigh scattering*: When X-rays irradiate a sample, a part of the incident X-rays is scattered instead of producing characteristic radiation. Namely, some photons hit electrons in the sample and bounce away depending on the scattering angle which is the angle between the incoming photon direction and the outgoing photon direction. This process is called Compton or incoherent scattering [101]. On the other hand, when photons interact elastically with electrons, the latter oscillate

at the frequency of the incoming X-Rays. As a consequence, the sample will emit radiation at the same frequency as the incident X-rays. This process is called Rayleigh or coherent scattering [101]. Therefore, a sample with light elements gives rise to high Compton and low Rayleigh scattering because a light element contains many loosely bound electrons. In contrast, a sample with heavy elements gives rise mostly to Rayleigh scattering due to the existence of strongly bound electrons in the sample.

Quantitative analysis: When continuous radiation is used to excite the characteristic X-rays of an element i in a completely homogeneous flat and smooth sample of thickness d (neglecting enhancement effects due to an extra excitation of the element of interest by the characteristic radiation of other elements in the sample), the intensity of the X-ray fluorescent radiation (I_i) is given by [69, 100]:

$$I_i = I_0 \cdot G \cdot C_i \cdot \int_0^d e^{-\left[\frac{\mu(h\nu)}{\sin \theta_1} + \frac{\mu(E_i)}{\sin \theta_2}\right] \rho x} dx, \quad (1.16)$$

$$= \frac{I_0 \cdot G \cdot C_i \cdot (1 - e^{-\rho d \left[\frac{\mu(h\nu)}{\sin \theta_1} + \frac{\mu(E_i)}{\sin \theta_2}\right]})}{\rho \left[\frac{\mu(h\nu)}{\sin \theta_1} + \frac{\mu(E_i)}{\sin \theta_2}\right]}, \quad (1.17)$$

where I_0 is the number of incoming photons; the factor G accounts for the XRF yield, solid angle, and detection efficiency; C_i is the concentration of the element i in the material; ρ is the sample density; μ is the total mass attenuation coefficient; E_i and $h\nu$ are the energies of the XRF and incoming radiation, respectively, while θ_1 and θ_2 are their respective angles relative to the sample surface. This approach neglects also the roughness of the sample surface and sample shape (only consider the flat sample).

Based on Equation 1.16, the concentration of an element i can be estimated. However, the intensity of characteristic X-rays in Equation 1.16 is modified by the effects of the incident (primary) $\mu(h\nu)$ and X-ray fluorescence (secondary) $\mu(E_i)$ absorption in the sample. These are major sources of the so-called matrix effects in XRF analysis. These effects are caused by absorption and enhancement of X-ray radiation in the specimen. The primary and secondary absorption occur if the elements in the sample absorb the primary and characteristic radiation, respectively. A strong absorption is observed if the sample contains an element with absorption edge of slightly lower energy than the energy of the characteristic line of the analyte element. When matrix elements emit characteristic radiation of slightly higher energy than the energy of analyte absorption edge, the analyte is excited to emit characteristic radiation in

1. INTRODUCTION

addition to that excited directly by the X-ray source [109]. Therefore, the intensity I_i is not only a function of the i element concentration, but also depends on that of the other constituents.

However, in case of thin samples and angles (θ_1, θ_2) that are not too small, the quantity $\rho d[\mu(h\nu)/\sin\theta_1 + \mu(E_i)/\sin\theta_2] \ll 1$, and the exponential function in Equation 1.16 can be approximated by the first two terms in its Taylor expansion [100]. Thus, the intensity of the characteristic X-rays, I_i^{thin} , depends linearly on the concentration of i element according to the equation:

$$I_i^{thin} = I_0 \cdot G \cdot C_i \cdot d. \quad (1.18)$$

This also indicates that for the thin-samples, the matrix effects can be neglected.

For thick samples, on the other hand, if the total mass per unit area ρd is sufficiently large, the exponential function in Equation 1.16 becomes negligible, thus Equation 1.16 is simplified to:

$$I_i^{thick} = \frac{I_0 \cdot G \cdot C_i}{\rho \left[\frac{\mu(h\nu)}{\sin\theta_1} + \frac{\mu(E_i)}{\sin\theta_2} \right]}. \quad (1.19)$$

The equation shows that the I_i^{thick} depends nonlinearly on the concentration of i element and depends also on matrix effects.

iii) Minimum detection limits

Besides the high spatial resolution, the MDL is also an important parameter for a synchrotron XRF measurement. The MDL is the lowest concentration at which an element can be detected in an experimental setup. This parameter is necessary to be known prior each sample measurement. It can be determined by the peak-to-background ratio, concentration of an element of a reference sample [110]. Usually, the MDL is determined by measuring SRM with well known elemental composition, following by the equation:

$$C_{MDL,i} = \frac{3\sqrt{I_{B,i}}}{I_i} C_i, \quad (1.20)$$

where $C_{MDL,i}$ is the minimum detection limit of element i in at.%. $I_{B,i}$ and I_i are the measured background and characteristic X-ray intensity of element i in counts. C_i is the concentration of element i in the standard reference sample in at.% unit. For instance, the MDL of our XRF measurements were determined by measuring the XRF of SRM 1577b (bovine liver) at 17 keV in pink beam and in 7/8 + 1 filling modes as shown in Figure 1.10. The MDL of Co and Zn are the ones of interest for

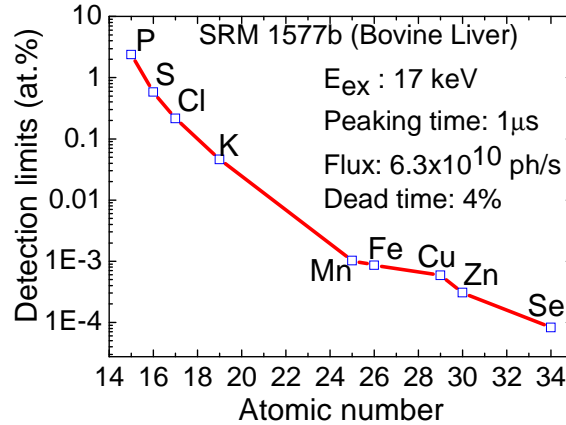


Figure 1.10: Detection limits of the XRF measurements calculated using the signal from the standard reference material 1577b (Bovine Liver) at 17 keV.

this thesis, which are about 7×10^{-4} and 3×10^{-4} at.%, respectively.

iv) XRF data acquisition, fitting and quantification

The XRF measurements were performed at the beamline ID22 (new beamline ID16B) using an in-vacuum undulator U23 with the setup shown in Figure 1.11. The X-ray beam coming from an insertion device U23 passes through high power slits and intensity attenuators [111] (not shown in the figure). The beam then is horizontally reflected at 0.14° by a Si mirror coated with Pd, Si and Pt layers, which produces a pink beam with different cut-off energies. A double crystal Si (111) monochromator is used afterwards to set the energy with a resolution of about 1 eV (monochromatic beam). For XRF measurements, however, we do not use the monochromator, but only the mirror to have a photon flux of about 10^{12} photons/second with an energy bandwidth $\Delta E/E \approx 10^{-2}$ (pink beam mode). Before interacting with the sample, the X-ray beam is focused by a pair of KB mirrors, which can focus the beam down to $50 \times 50 \text{ nm}^2$ at 17 keV. More details about the setup and instrumentation at the beamline ID22 are found elsewhere [95, 112]. For data collection, the emitted X-ray fluorescence signal from the sample was collected using an energy dispersive Si drift detector placed at 15° with respect to the substrate surface. XRF maps were also obtained by scanning sample with a piezo stage on the nanobeam with a step size of $25 \times 25 \text{ nm}^2$ and integration time of 500 ms per point. The working distance between the sample and the detector integrated with a Mo collimator is about 17 mm, but this distance may be varied, depending on the strength of the X-ray fluorescence signal of the element of interest. During the data acquisition, several parameters of the Si

1. INTRODUCTION

drift detector such as dead time, peaking time, and solid angle need to be taken into account since they also strongly affect the quality of the XRF measurement.

Dead-time correction and solid angle: Whenever the detector detects an X-ray photon, it needs some times to analyze and process the signal. Within this period, called the dead-time, no other X-ray photons are detected and are thus lost. This dead-time is of the order of a few microseconds [100]. The counting losses are thus dependent on the actual count rate. It means the greater the count rates, the greater losses during the measurement. The measured count rate R_m is always lower than the actual count rate R_T following the expression [100]:

$$R_T = \frac{R_m}{1 - \tau_d R_m}, \quad (1.21)$$

where τ_d is the dead-time. The actual count rate is determined by the detector's solid angle (Ω) that can be obtained by [113]: $\Omega = A/r^2$, where A is the surface area of the detector, and r is the sample to detector distance. If the solid angle is large, meaning high actual count rates, therefore the higher photons are not detected. As a result, a dead-time correction should be made in the measurement setup, for instance, moving the detector backward or inserting an attenuator. The XRF data were analyzed using a non-linear least-squares fitting routine PyMca [114]. The program allows to do XRF spectrum fitting and quantification.

XRF Spectrum fitting: The characteristic radiation of a particular X-ray line has a Lorentz distribution. Peak profiles observed with most solid-state detectors are the convolution of this Lorentz distribution with the nearly Gaussian detector response function [100]. A Gaussian peak is characterized by three parameters: the position, width, and height or area. The non-linear least-square fit PyMCA is able to determine these parameters during the fitting. The XRF peaks observed in the spectrum are directly related to the elements present in the sample. The peak fitting function in the PyMCA is written in terms of energy of these elements rather than channel number. Defining *ZERO* as the energy of channel 0 and expressing the spectrum *GAIN* in eV/channel, the energy of channel i is given by [114]:

$$E(i) = ZERO + GAIN \times i. \quad (1.22)$$

The non-linear least-square fit PyMCA optimizes *ZERO* and *GAIN* for the entire fitting region, thus for all peaks simultaneously. As a result, the actual position of the peaks is obtained through their energies calculated by Equation 1.21. However, for the best XRF spectrum fitting, it is necessary to take into account the continuum/background, sum and escape peaks. The background can be estimated through

an iterative procedure in which the content of each channel is compared against the average of the content of its neighbors at a distance of i channel. If the content is above the average, it is replaced by the average. To speed up the procedure, i can be taken as a fraction of the peaks FWHM at the beginning of the iterative process, being one of the end of it [114]. Concerning the escape peak, its fraction f is defined as $f = N_e/(N_p + N_e)$. PyMCA assumes normal incidence to the detector and considers the escape only from the front surface. For a Si detector, the escape peaks could be modeled by a Gaussian at 1.74 keV below the parent lines. The escape peaks are not fitted as independent peaks, but they are part of the multiplet [114]. Concerning the sum peaks, since any of the peaks can be detected simultaneously with any other peaks, one can calculate the summing contribution of channel i , simply shifting the whole calculated spectrum by i channels and multiplying it by the calculated content of the channel times a fitted parameter. This will be then repeated for all the points of the spectrum. The physical meaning of that parameter, for a time acquisition of one second, could be interpreted as the minimum time, measured in seconds, needed by the acquisition system to distinguish two photons individually and not considering them as a single photon [114].

Estimation of elemental concentration: Once the peak identification and energy calibration are done, the peak intensity can provide the elemental concentrations. Indeed, the intensity of the characteristic X-rays of element i is linearly dependent on its concentration (C_i) according to Equation 1.18 because the thickness of the NWs studied in this work is small (150 – 250 nm), relative to their lengths from several to tens of microns. Based on Equation 1.18 and taking into account the thickness profile of the NWs, the only unknown terms to calculate the concentration are the incident intensity and the detector efficiency. Using the PyMCA, the concentration can be estimated by two following methods:

- 1) The fundamental parameter method works if the two unknown parameters (incident intensity and detector efficiency) are determined and then used as input parameters. This can be done by analyzing the XRF data of a SRM with well-known elemental concentrations. The measurement conditions for XRF data acquisition of the SRM should be identical for the data acquisition of the sample under investigation. Due to the concentration of each element in the SRM is known, PyMCA will allow to determine the fundamental parameters such as the incident intensity and detector efficiency. Such known fundamental parameters are inputted into the PyMCA program for the XRF quantification of the studied sample. Therefore, the concentration of each element of interest in the sample will be calculated [114].

1. INTRODUCTION

2) The matrix composition method is an indirect method to determine the two unknown parameters above. By this method, one of the matrix elements of the sample is selected as an internal reference. Thus, the mass concentration of a wanted element can be estimated by using the PyMCA. Namely, the mass fraction of the wanted element as well as the selected reference element calculated from the chemical formula of the sample are inserted into the PyMCA. The XRF fitting/quantification will be performed iteratively until the inserted value be identical to the value obtained from the fitting [114].

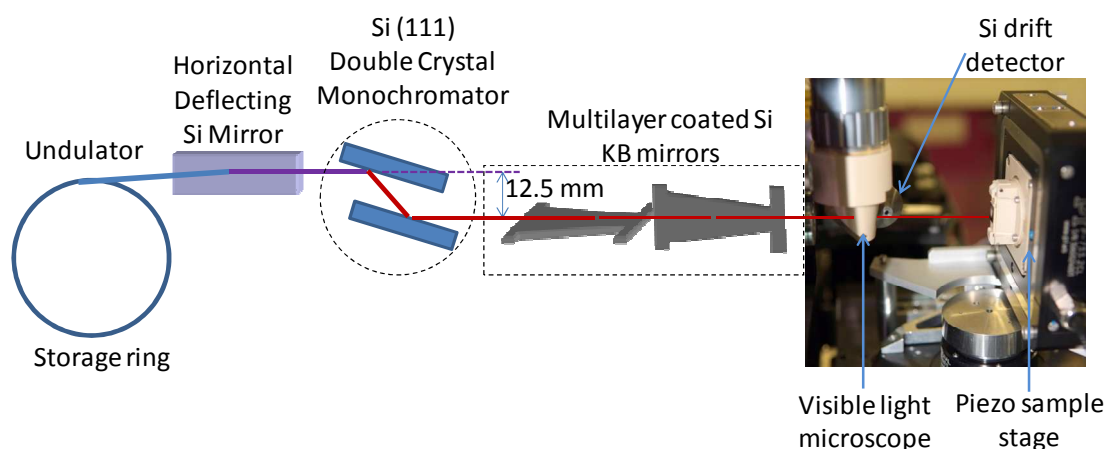


Figure 1.11: Schematic of the experimental setup for recording X-ray fluorescence and X-ray absorption using a synchrotron X-ray nanobeam at the beamline ID22. The vertical mirror is a Si crystal coated with Si, Pd, Pt used at 2.5 mrad to remove high harmonics. The Si (111) monochromator allows the selection of the working energy with a spectral resolution of 1 eV. Multilayer coated KB mirrors are used to focus the X-ray beam down to nanometer length scale. The XRF data are collected by an energy dispersive Si drift detector.

1.3.5 X-ray absorption spectroscopy

XAS is a powerful tool for studying short-range order and/or electronic structure of a broad range of crystalline and amorphous materials. Namely, it can provide quantitative structural information at the atomic scale about the local environment around the absorbing atom, i.e., near-neighbor species, interatomic distances, coordination chemistry, valence state and coordination number [115]. In principle, XAS information can be obtained for every elements, as long as atoms have core level electron transitions [116]. This section introduces XAS and its principles as well as discusses how information can be extracted from X-ray absorption spectra.

1.3 Synchrotron nanoprobe

The X-ray absorption process is based on the photoelectric effect. Thus, a transition between two quantum states: from an initial state (with an X-ray, a core electron, and no photoelectron) to a final state (with no X-ray, a core hole and a photo-electron). Namely, when tuning the energy of incident photons to a value that is equal or larger than the binding energy of an atom, an electron from an inner core level is ejected to a vacant excited state or to the continuum. The ejected electron is called photo-electron and has a kinetic energy (E_k):

$$E_k = h\nu - E_b = \frac{\hbar^2 k^2}{2m} = \frac{2\hbar^2 \pi^2}{m\lambda^2}, \quad (1.23)$$

where $E = h\nu$ is the incoming photon energy, and E_b is the binding energy of the atom. This phenomenon results in a sharp rise in the absorption intensity, which is called an absorption edge. Thus, the absorption edge energy (E_0) corresponds to the binding energy E_b . As mentioned in previous sections, the absorption edges are labeled in order of increasing energy such as K, L₁, L₂, L₃, ..., corresponding to the excitation of an electron from $1s$ ($^2S_{1/2}$), $2s$ ($^2S_{1/2}$), $2p$ ($^2P_{1/2}$), $2p$ ($^2P_{3/2}$), ..., orbitals (states), respectively. Transitions corresponding to these edges are illustrated in Figure 1.12 (a). Following the absorption process, the ejected electron left a hole at core level of an atom. Therefore the atom is now in an excited state, which will decay typically within a few femtoseconds. In the hard X-ray regime, the dominant mechanism of the decay of the excite state is the X-ray fluorescence, discussed in Section 1.3.2.

XAS is the measurement of the X-ray absorption coefficient $\mu(E)$ of a material as a function of energy. The energy dependence of the absorption coefficient $\mu(E)$ can be measured either in transmission and X-ray fluorescence modes. The transmission mode is typically used for a concentrated sample in which the element of interest is the major component ($> 10\%$), while the X-ray fluorescence mode is used for a material with a lower concentration (down to parts per million level). In this work, we used the X-ray fluorescence mode for all the XAS measurements (schematic of experimental setup is shown in Figure 1.11). The absorption coefficient $\mu(E)$ in this case can be obtained through the expression:

$$\mu(E) = \frac{I_f}{I_0}, \quad (1.24)$$

where I_f is the intensity of the X-ray fluorescence lines, I_0 is the intensity of incoming X-rays. Figure 1.12 (b) shows an example of XAS spectrum measured in the X-ray fluorescence configuration for a sample studied in this thesis: a Co-implanted ZnO

1. INTRODUCTION

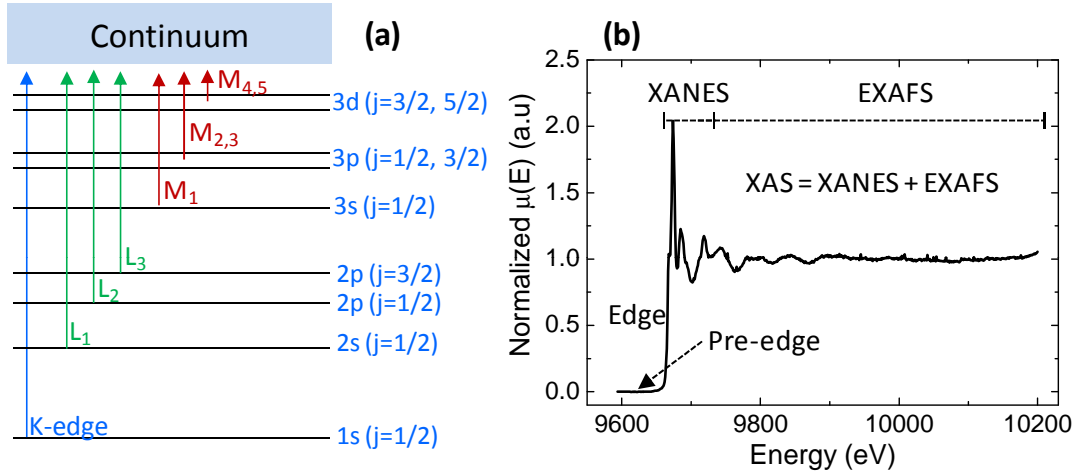


Figure 1.12: (a) Schematic illustration of the transitions that contribute to the absorption edges. j is the total angular momentum of an electron energy level. (b) Example: a Zn K-edge X-ray absorption spectrum of ZnO:Co NWs recorded in X-ray fluorescence configuration.

NW. An XAS spectrum is generally divided into two parts: X-ray absorption near edge structure (XANES) and extended X-ray absorption fine structure (EXAFS). The energy dividing the XANES from the EXAFS is roughly estimated, at the wavelength of the excited electron which is equal to the distance between the absorbing atom and its nearest neighbors. Usually, XANES is a region of XAS spectrum within ~ 50 eV of the absorption edge, including pre-edge and edge regions. While EXAFS covers the region from 50 to 1000 eV above the edge.

Since XAS is a type of absorption spectroscopy from a core initial state with a well defined symmetry, the quantum mechanical selection rules set the symmetry of the final states in the continuum, which usually are mixture of multiple components. The electronic-dipole selection rule for a transition to an unoccupied final state is that an orbital angular momentum quantum number $\Delta l = \pm 1$ [72, 117]. For instance, the most intense features of a K-edge are due to core transitions from $1s \rightarrow p$ -like final states.

i) X-ray absorption near edge structure

As mentioned above, the XANES spectrum covers the energy region from the pre-edge to ~ 50 eV above the absorption edge. The features caused by the electronic transitions to empty bound states and multiple-scattering resonances of the photoelectrons with low kinetic energy.

The pre-edge of XANES is the region with $E < E_0$. The pre-edge peak structures usually result from bound state transitions. The pre-edge structures of a K-edge absorption spectrum arise from $1s$ to unfilled $3d$ transition. Although the $1s$ to $3d$ transition is forbidden by dipole selection rules, it is nevertheless observed due to $3d$ to $4p$ orbital hybridization [118, 119]. Thus, these pre-edge structures are observed for every first row transition metal in the periodic table as long as its $3d$ orbital is not fully occupied. The pre-edge region gives information on local geometry and bonding characteristics of the absorption sites. Its height and position can be also used to empirically determine the oxidation state and coordination chemistry [116].

The absorption edge is the position with $E = E_0$, where a sudden increase of absorption appears, defining the ionization threshold to the continuum. Therefore, the energy of the X-ray absorption edge sensitively depends on the electronic structure and chemical state of the absorber. Such information is useful to identify the oxidation state of the atomic species. Usually, the edge shows a shift to higher energy with the increase of the oxidation state. It can be simply explained by considering that it is increasingly difficult to remove an electron from an atom that bears a higher positive charge. For instance, a difference of one unit in Mn oxidation state is related to a shift ~ 4 eV in the absorption edge feature [120].

In the XANES region above the absorption edge, because of such low kinetic energy, the wavelength calculated from Equation 1.22 is larger than the interatomic distance of photoabsorber and backscatter pair. Thus, the photoelectron backscattering amplitude by neighbor atoms is very large so that multiple scattering features become dominant in the XANES spectrum [121]. This provides information about the first coordination shells around the absorbing atom and bond angles.

ii) Extended X-ray absorption fine structure

The EXAFS refers to the absorption coefficient modulation starting from about 50 eV to 1000 eV above the absorption edge. The simplest EXAFS theory is explained through the single scattering approximation [116, 122]. As mentioned earlier, when an incident X-ray beam with sufficient energy is absorbed by an electron at a core-level of absorbing atom A (Figure 1.13), a photoelectron is ejected away from the atom A. This photoelectron is also represented as a spherical wave with a wave vector (k) as follows:

$$k = \sqrt{\frac{2m(E - E_0)}{\hbar^2}}, \quad (1.25)$$

1. INTRODUCTION

where E is the incident photon energy, E_0 is the absorption edge energy, \hbar is reduced Planck constant and m is the electron mass. If there is a neighboring atom B as shown in Figure 1.13, the outgoing photoelectron wave will be scattered back to the absorber. The interference between the outgoing and backscattered photoelectron waves, therefore, gives rise to the oscillation in the X-ray absorption coefficient. In case of constructive interference, outgoing and scattered photoelectron waves are in phase as shown in Figure 1.13 (a), and maxima are observed. In contrast, the minima correspond to destructive interference as shown in Figure 1.13 (b), out of phase between outgoing and scattered photoelectrons.

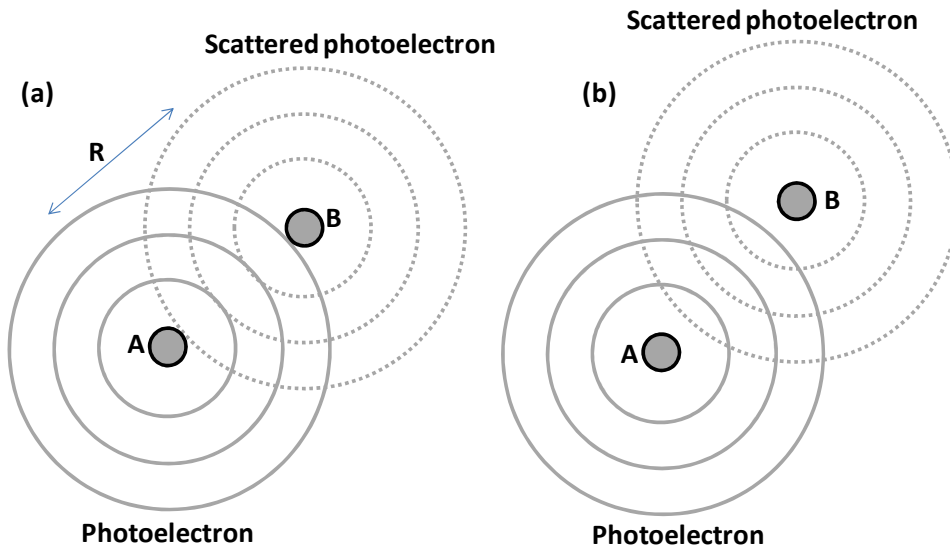


Figure 1.13: Schematic of the single scattering between absorbing atom A and neighboring atom B in the EXAFS energy region. (a) and (b) Constructive and destructive interferences due to the outgoing and back-scattered photoelectrons are in phase and out of phase, respectively.

In EXAFS analysis, it is typical to define $\chi(k)$, as the fractional modulation of the X-ray absorption coefficient:

$$\chi(k) = \frac{\mu(E) - \mu_0(E)}{\mu_0(E)}, \quad (1.26)$$

where $\mu(E)$ is the experimentally determined absorption coefficient and $\mu_0(E)$ is the atomic background absorption of a “bare atom”. $\mu_0(E)$ can not be measured experimentally because of the physical impossibility of isolating the atoms in the sample. Therefore, it is estimated by fitting a smooth spline function through the data [123].

Division by $\mu_0(E)$ normalizes the EXAFS oscillations “per atom” and thus, the EXAFS represents the average structure around the absorbing atoms.

The EXAFS equation

Since the EXAFS spectrum can be considered as summation of a weight addition of a range of waves with different wavelengths (or frequencies), the different frequencies appearing in the oscillations in $\chi(k)$ correspond to different near neighbor coordination shells, which can be described and modeled by following the EXAFS equation [124, 125]. In other words, the EXAFS equation is a theoretical expression that describes $\chi(k)$ in terms of structural parameters and thereby allows structural information to be derived from the experimental $\chi(k)$ [122, 123]:

$$\chi(k) = \sum_j \frac{N_j S_0^2 f_j(k)}{k R_j^2} e^{-2k^2 \sigma_j^2} e^{-2R_j/\lambda(k)} \sin[2k R_j + \delta_j(k)] \cdots \quad (1.27)$$

In Equation 1.27, the parameters that are usually considered for the study of the local structure and coordination chemistry are the number of scattering atoms known as N_j , the absorber–scatterer distance, R and σ^2 , known as the Debye-Waller factor, which is the mean square variation in the interatomic distance R due to the structural disorder. However, there are a variety of other parameters that must either be determined or defined in order to extract the physically/chemically relevant information; for instance, $f(k)$ and $\delta(k)$ which represent, respectively, the magnitude of the back-scattering amplitude, and the phase shift that the photoelectron wave undergoes when passing through the potential of the absorbing and scattering atoms. These amplitude and phase parameters contain the information necessary to identify the scattering atom [122].

The EXAFS amplitude reduces as $1/R^2$, which reflects the decrease in photoelectron amplitude per unit area as one moves further from the absorbing atom. The main consequence of this damping is that the EXAFS information is limited to atoms in the vicinity of the absorber. There are three additional damping terms in Equation 1.27: i) the S_0^2 term that is an amplitude reduction factor due to multiple excitation at the absorbing atom or many body effects such as the shake up/off processes at the absorbing atom. It means that S_0^2 depends on the atom itself and its value is usually estimated by the fitting of a metallic foil or reference sample. Typically, S_0^2 has a value between 0.7 and 1. ii) the exponential $e^{-2k^2 \sigma_j^2}$ term which reflects the fact that if there is more than one absorber–scatterer distance, each distance will contribute to the EXAFS oscillations with a slightly different frequency. The destructive

1. INTRODUCTION

interference between these different frequencies leads to a reduction in the EXAFS amplitude. iii) the $e^{-2R_j/\lambda(k)}$ term is a reduction factor that arises from the mean free path of the photoelectron $[\lambda(k)]$. This limits further the distance range that can be measured by EXAFS. As a consequence of these damping terms in Equation 1.27, EXAFS oscillations are typically observed for atoms within approximately 5 Å of the absorbing atom [122].

iii) XAS data acquisition and analysis

The XAS measurements were performed at the beamline ID22 using the nano-X-ray beam with the setup shown in Figure 1.11. The double Si (111) monochromator was used in the XAS measurements in order to scan the energy with resolution of 1 eV. Thus, in combination with the X-ray nanobeam, the XAS acquisitions were collected with a spot size of around $110 \times 110 \text{ nm}^2$ and a photon flux approximately 10^{10} photons/second. The XANES and EXAFS data were recorded in XRF mode with a step size of 1 eV and integration times determined by the counting statistics. The XANES and EXAFS data reductions were performed using the IFEFFIT package (i.e., ATHENA) [126, 127]. The EXAFS data analysis was then carried out by *ab initio* modeling of the absorption cross section using the FEFF code [128]. Theoretical backscattering amplitudes $f(k)$ and phase shifts $\delta(k)$ from Equation 1.27 for all single and multiple scattering paths were calculated using hexagonal ZnO model clusters (e.g., $a = 3.2498 \text{ Å}$ and $c = 5.2066 \text{ Å}$) [129]. Once these theoretical factors were determined, the ARTEMIS routine [126, 127] was exploited to fit the data in R space within the window $[1.0 - 3.7 \text{ Å}]$, which included the first and second coordination shells. The amplitude $S_0^2 = 0.7307$ was determined from a metallic Zn foil. The coordination number around the Zn absorbing atom of four O nearest neighbor and twelve Zn second nearest neighbor atoms were fixed. As a result, we have fitted the interatomic distances (R_i) and Debye-Waller factors (σ_i^2) of the various atomic shells.

1.3.6 X-ray diffraction

XRD is a versatile, non-destructive technique that allows the study of the crystal structure of materials in the long range order. Some basic fundamentals of XRD are reviewed in order to understand easily how to extract the structural information of a compound from the diffraction pattern.

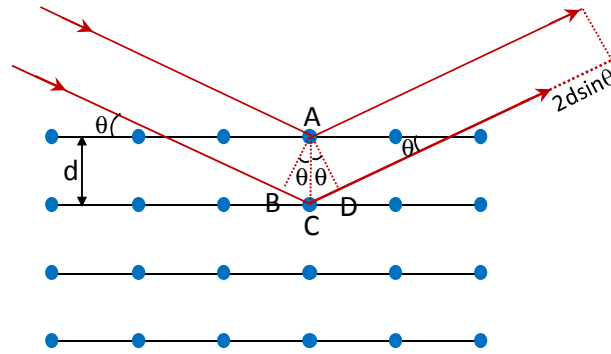


Figure 1.14: A Bragg reflection from a particular family of lattice planes, separated by a distance d . Incident and reflected rays are shown for the two neighboring planes.

i) Principle of X-ray diffraction

The principle of XRD is based on the Bragg's law [130, 131]. W. L. Bragg found that crystalline materials under monochromatic X-ray irradiation produce typical patterns of intense reflected X-ray intensity peaks. This was explained by regarding a crystal that is constituted by parallel planes of ions, with spacing between two closest planes d as shown in Figure 1.14. The conditions for an intense peak of the scattered X-ray are [130]:

- The X-rays should be specularly reflected by the ions in any one plane, namely the angle of incident X-ray (θ) equals the angle of reflected one (θ).
- The reflected X-rays from successive planes should interfere constructively to each other. In order that happens, we should take into account the path difference of the two reflected X-rays on two successive planes between two X-rays. According to Figure 1.14, the path length difference is $(BC + CD)$ that equals $2d \sin \theta$, where θ is the angle of the incident X-rays. To the reflected X-rays interfering constructively, the path length difference must be an integral number n of the X-ray wavelength (λ), this was known as the Bragg's law:

$$n\lambda = 2d \sin(\theta). \quad (1.28)$$

This equation allows to determine d -spacing between the planes. Through the relationship between the d , lattice parameters, and Miller indices, for instance the hexagonal system gives the relationship: $1/d^2 = 4(h^2 + hk + k^2)/3a^2 + l^2/c^2$. Based on the two (hkl) planes, the full structure parameters of the crystal can be determined.

1. INTRODUCTION

ii) Intensities of diffracted beam

Let us consider to the powder X-ray diffraction method, which was used in this work. The integrated intensity of each powder diffraction peak is affected by several factors by the following expression [132]:

$$I_{(hkl)} = |F_{(hkl)}|^2 \times M_{(hkl)} \times LF(\theta) \times TF(\theta), \quad (1.29)$$

where $|F_{(hkl)}|$ is the structure factor, $M_{(hkl)}$ is multiplicity, $LF(\theta)$ is Lorentz factor, and $TF(\theta)$ is temperature factor.

- *Structure factor*: The structure factor reflects the interference between atoms in the unit cell. All of the information regarding where the atoms are located in the unit cell is contained in the structure factor. The structure factor is given by the following summation over all atoms (from 1 to N) in the unit cell [132]:

$$F_{(hkl)} = \sum_1^N f_j e^{2\pi i(hx_j + ky_j + lz_j)}, \quad (1.30)$$

where f_j is a form factor for the j^{th} atom that describes the efficiency of scattering of given atom in a given direction; h, k , and l are Miller indices; x_j, y_j , and z_j are the fractional coordinates of the j^{th} atom.

- *Multiplicity factor*: This is defined as the number of different planes in a form having the same spacing. For instance, a family of planes $\{100\}$ of a cubic crystal contains six different planes (different Miller indices), thus the $M_{(hkl)}$ is six. The multiplicities are lower in lower symmetry systems [132].

- *Lorentz factor*: There are a number of factors that lead to a *theta* dependence of the peak intensities: 1) diffraction can occur for angles slightly different from the value predicted by Bragg's law; 2) the number of crystals oriented in such a way as to satisfy Bragg's law is highest for low angles; 3) the fraction of the diffraction cone that intersects the detector is highest at low angles. When combine these considerations and do some trigonometric manipulation we get the Lorentz factor [132]: $1/(4 \sin^2 \theta \cos \theta)$.

- *Temperature factor*: The vibrations of atoms in a crystal lead to an angle dependent effect on the diffracted peak intensities. The more an atom vibrates the scattering power is decreased, because the scattering power of the atom is smeared out. As an approximation we can assume that all atoms vibrate equally. In that case

the temperature factor $TF(\theta)$ can be expressed by the expression: $e^{-2B(\frac{\sin \theta}{\lambda})^2}$, where the coefficient B is the isotropic temperature factor, being proportional to the mean

squared displacement of the atoms [132].

iii) XRD data acquisition and analysis

For XRD measurements, we used a similar setup like the one for XAS measurements as shown in Figure 1.11 plus a fast readout low noise CCD detector [133] placed behind the sample to record the diffractograms. Using an incident monochromatic beam of 28 keV, Co-implanted ZnO NW samples were measured by rotating the NWs to an angle θ that satisfies the Bragg's condition for certain planes. At this angle, in order to get a map the NWs were scanned through the beam with a step size of $100 \times 100 \text{ nm}^2$. The XRD data was analyzed using the Fit2D program [134, 135], which allows to correct and integrate the 2D data. Thus, we could obtain 2θ XRD spectra and build XRD maps.

1.4 Complementary characterization tools

1.4.1 Scanning electron microscopy

SEM uses a focused energetic electron beam to generate a variety of signals at the surface of a sample. From electron-sample interactions in SEM, the signals obtained such as secondary electrons and backscattered electrons are most valuable for studying morphology of the sample and for illustrating contrasts in composition in multiphase samples, respectively.

In this work, we used a Zeiss Leo 1530 SEM with an acceleration voltage of 20 keV at the ESRF to localize and to study the morphology of the NWs before measuring them at the beamline with the hard X-ray nanoprobe.

1.4.2 Transmission electron microscopy

TEM uses a parallel high energetic electron to illuminate a sample. The secondary signals such as elastically/inelastically scattered electrons, high angle incoherent electron are commonly detected in TEM due to the interaction of the high-energy electron beam with a thin sample. Each signal is used for different purposes. For instance, the elastically scattered electrons are used to form bright field, dark field, and diffraction pattern TEM, as well as high-resolution TEM images. For bright field-TEM, the parallel incident beam is imaged through the sample onto a screen. The contrast is produced by absorption of electrons in the sample (called mass-thickness contrast). In case of dark field-TEM, only electrons diffracted in a certain direction are used to

1. INTRODUCTION

generate an image. The type of contrast for this case is diffraction contrast, which is used to distinguish between different crystal phases or orientations, by choosing a reflection characteristic for a particular crystal phase or crystal orientation. This makes the regions of the sample with the selected phase become bright and regions with all other phases dark in the image. Electron diffraction pattern-TEM was used to identify the crystal phases and the growth direction of the NWs. high-resolution TEM images are formed by interference of the direct and the diffracted beams, and this is called phase-contrast imaging.

In order to complement results obtained by synchrotron nanoprobe based techniques, a TEM investigation was performed by the group of Prof. Carsten Ronning using a JEOL JEM 3010 system with a thermal LaB₆ electron gun at 300 keV.

1.4.3 Optical characterization

The optical properties of Co-implanted ZnO NWs were also studied in collaboration with the group of Prof. Carsten Ronning. It is well-known that a semiconductor can emit light under the excitation with an external source. If the light is generated by the absorption of photons, the emission process is called photoluminescence (PL). If high energy electrons are used to bombard the sample, resulting in light emission, this process called cathodoluminescence (CL). In this work, these two methods were used to investigate Co-implanted ZnO NWs to confirm the successful optical activation of implanted Co ions in ZnO NWs, as well as to corroborate the results obtained from the synchrotron based characterizations.

i) Cathodoluminescence spectroscopy: CL measurements were performed using a JEOL SEM equipped with a GATAN MonoCL³⁺ system. The electron energy was 10 keV for all CL investigations at 10K. Monochromatic CL images were acquired using a high-sensitivity photomultiplier coupled to a grating monochromator at a bandwidth of 5 nm. While CL spectra were detected using a back-illuminated CCD camera [48, 136].

ii) Photoluminescence spectroscopy: Micro-PL measurements were performed below 10K using a self-built epifluorescence microscope with excitation by a continuous-wave 325 nm HeCd laser [137]. While, time-resolved photoluminescence measurements were performed, exciting by frequency-tripled Nd:YAG laser (pulse FWHM 3 ns) and

detection by a grating monochromator with an intensified CCD camera using a gate width of 5 ns [138].

1.5 Key challenges and scientific goals

Doping of semiconductor NWs by ion implantation is a critical step to produce homogeneously doped materials with novel properties and functionalities for new devices [40, 41]. However, the doping during growth is a challenging task, as the self-organized growth mechanisms are sensitive to changes in the growth conditions. Doping of ZnO NWs with Co via wet chemical methods is possible [139], but the control of the dopant concentration is not precise and the crystal quality is lower compared to VLS grown NWs [140]. In general it was observed that doping during VLS growth tends to provide an inhomogeneous dopant distribution [141] and the dopant concentration is typically limited by the low solubility in the solid phase [142]. A successful alternative is the doping by ion implantation, which can overcome all the drawbacks and provides doping with nearly every element in the desired concentration [68]. But, the method generally produces structural defects into the host structure, which can be reduced through a thermal annealing process. Therefore, so far, a long lasting field of research is the understanding of ion implantation induced lattice damage and subsequent structural recovery during the post-implantation thermal treatment, especially at the nanometer scale [143]. The growth and Co doping of ZnO NWs were presented in the Ph.D work of Sebastian Geburt from the University of Jena [48]. The present dissertation focuses on the chemical and structural characterization of the Co-implanted ZnO NWs with different growth conditions using a hard X-ray nanoprobe. We address the following challenges:

1) Homogeneity and concentration of implanted ions along single ZnO:Co nanowires

The utilization of transition metal doped ZnO NWs for optoelectronics or spintronics requires the control of the transition metal concentration and homoneneous distribution across the whole NWs. Although there are many reports on Co doped ZnO NWs [68, 144–146], besides the issues of magnetism stability [146], it remains controversial whether the incorporation of Co dopant is as uniform as in bulk crystals or thin films, or with metal clusters and precipitates of impurity phases [144]. In both radial and axial directions, it is still crucial to address nanosegregation effects, trace element contaminations with magnetic nanoparticles, and mixtures of phases in small

1. INTRODUCTION

domains [147]. However, the role of impurities on NWs and/or on phase separation effects can be only achieved using analytical techniques which are element-specific with high chemical trace sensitivity, and capable of detecting up to nanosized aggregates within deep escape depths.

Therefore, **the first paper** [M. H. Chu, J. Segura-Ruiz, G. Martínez-Criado, P. Cloetens, I. Snigireva, S. Geburt, and C. Ronning. “*Synchrotron fluorescence nanoimaging of a single Co-Implanted ZnO nanowire*”. Phys. Status Solidi RRL **5**, 283 (2011)] embedded in this thesis addresses the first key challenge. We investigate the elemental distribution of single as-grown and Co-implanted ZnO NWs by a hard X-ray nanoprobe. Within our experimental accuracy, nano-XRF data shows no presence of background impurities in the NW but residual Fe and Sn in the substrate. Elemental maps of Zn and Co displays a homogeneous distribution at the length scale of the X-ray beam size, without clustering or segregation effects. Through XRF quantification, Co concentration is roughly estimated about (0.15 ± 0.05) at.%. These findings are also confirmed in other papers presented in the second part of this dissertation.

2) Local structure of thermally annealed single ZnO:Co nanowires

In addition to the study of elemental distribution in the single NWs, determining the dopant local order in individual NWs is crucial to understand their behavior in nanodevices [148, 149]. Also, the investigation of the oxidation state of Co ions is important as valence state of Co ions can be either 3^+ or 2^+ , but only intense Co^{2+} intra- $3d$ emission has been observed [44, 46]. Although the average local atomic structure in ensembles of ZnO:Co NWs had been studied by XANES and EXAFS [118, 150], its examination in single NWs by XAS is still an experimental challenge due to the beam instability during the energy scan and chromaticity of the nanofocusing lens. It remains open whether the incorporation of Co in individual NWs is substitutional as in bulk crystals or thin films, without the formation of metallic clusters or precipitates, and lattice distortion [151, 152]; How the oxidation state of implanted ions behaves along the single NWs? These points enable to evaluate the role of thermal annealing in the recovery of ZnO structure after the Co ion implantation process.

Therefore, **the second paper** [J. Segura-Ruiz, G. Martínez-Criado, M. H. Chu, S. Geburt, C. Ronning. “*Nano-X-ray absorption spectroscopy of single Co-implanted ZnO nanowires*”. Nano Lett. **11**, 5322 (2011)] reports for the first time on the local structure of single Co-implanted ZnO NWs subjected to a thermal treatment through a hard X-ray nanoprobe. XANES around the Co K-edge displays the substitutional incorporation of Co^{2+} ions into the Zn sites of the wurtzite host lattice. EXAFS data

1.5 Key challenges and scientific goals

analysis supports the tetrahedral configuration of Zn in the hexagonal host lattice without pronounced distortion in the interatomic distances of the two nearest neighbor shells. The EXAFS results give no evidence of large structural defects induced in the ZnO host lattice by the Co incorporation and confirm the annealing mediated recovery of the ZnO structure. In addition, the linear polarization of the synchrotron nanobeam made our study not only element specific, but also capable of detecting preferentially oriented defects induced by the ion implantation process. Polarization dependent XANES shows no structural disorder induced neither in the radial nor axial directions of the implanted NWs after the subsequent annealing. The recovery of the damaged structure induced by the ion implantation through the thermal annealing was also confirmed in the following papers.

3) Ion implantation-induced defects in single ZnO:Co nanowires

As mentioned above, the ion implantation process has proven to be an effective and easy way to incorporate Co into the ZnO host lattice. But, the method generally produces unwanted structural defects in the NWs, which could ultimately limit the scalability of semiconductor NWs, as well as affect the performance of advanced optoelectronics and spintronics nanodevices. Although we showed that such defects could be reduced through a thermal annealing process, the study of NWs that have not been subjected to this treatment is also crucial in order to control the collateral effects. So far, using conventional diffraction methods and EXAFS over large ensembles of implanted NWs, it has been revealed a crystal lattice distortion induced by the ion implantation process [153–156]. However, its direct observation from individual NWs has not been addressed in both short and long range orders. Therefore, the following papers concentrate on this third challenge.

The third paper [M. H. Chu, G. Martínez-Criado, J. Segura-Ruiz, S. Geburt, and C. Ronning. “*Local lattice distortions in single Co-implanted ZnO nanowires*”. *Appl. Phys. Lett.* **103**, 141911 (2013)] reports on the local structure of as-implanted and thermally-treated single ZnO:Co NWs. Although the Co ions are incorporated into the wurtzite ZnO lattice, X-ray absorption near edge structure data show high structural disorder in the as-implanted NWs compared with the annealed ones. In particular, extended X-ray absorption fine structure from single wires reveals a lattice distortion around Zn sites of the as-implanted NWs, which involves an expansion of the wurtzite lattice.

The fourth paper [M. H. Chu, G. Martínez-Criado, J. Segura-Ruiz, S. Geburt, and C. Ronning. “*Structural order in single Co-implanted ZnO nanowires*”. *Phys. Status Solidi A* **211**, 483 (2014)] presents a preliminary study on the long range

1. INTRODUCTION

order of single room temperature-implanted (as-implanted) and high temperature-implanted ZnO:Co NWs. XRD results suggest a crystal lattice expansion induced by the ion implantation process in the as-implanted NWs and a recovery of lattice crystal for the high temperature implanted NWs. In addition, micro-PL data corroborate these findings. However, further detailed XRD study was necessary to confirm the results.

The fifth paper [M. H. Chu, G. Martínez-Criado, J. Segura-Ruiz, S. Geburt, and C. Ronning. “*Nano-X-ray diffraction study of single Co-implanted ZnO nanowires*” in press on Phys. Status Solidi A (2014) DOI: 10.1002/pssa.201431194] with the aim to gain further insights into the ion implantation-induced defects distribution along the NWs, presents a full study on the long-range order of individual ZnO:Co NWs by nano-XRD. The findings reveal a distortion of the c lattice constant along the c -axis because of the ion implantation-induced defects, which were reduced, as expected, through a thermal annealing process. In addition, a rough comparison of the findings obtained by XRD and EXAFS techniques in this paper results in a full agreement between the short- and long-range orders.

Complementary results on optical properties of single Zn:Co nanowires

The sixth paper [S. Geburt, R. Roder, U. Kaiser, L. Chen, M. H. Chu, J. Segura-Ruiz, G. Martínez-Criado, W. Heimbrodt, and C. Ronning. “*Intense intra 3d-luminescence and waveguide properties of single Co-doped ZnO nanowires*”. Phys. Status Solidi RRL **7**, 886 (2013)] presents the optical properties of single ZnO:Co NWs studied by micro-PL and -CL to complement the results obtained by hard X-ray nanoprobe. The results show that Co^{2+} ions are indeed optically activated and emit an intense intra-3d luminescence in the visible and near infrared range. Thus, in good agreement with the previous reports, the single implanted NWs showed a homogeneous Co^{2+} emission. The Co-implanted NWs emit waveguided emission from their ends with an enhanced absorption in the range of the Co emission. The spectra of single implanted NWs at different excitation powers follow a linear emission increase with power up to 1000 W/cm^2 .

2

Conclusions and Perspectives

2.1 Conclusions

The present PhD thesis has shown the combined use of nano-XRF, nano-XAS, and nano-XRD tools to study single Co-implanted ZnO NWs. These three techniques make use of the high spatial resolution in pink ($60 \times 60 \text{ nm}^2$) and monochromatic ($110 \times 110 \text{ nm}^2$) beam operation modes provided by the KB mirrors based X-ray nanoprobe. The multi-technique approach which relied on a synchrotron nanoprobe, allowed the direct characterization of the composition, short- and large-range structural order of single semiconductor NWs at the nanometer length scale. The most relevant findings are:

- The nano-XRF data analysis indicated the homogeneous distributions of the Zn and Co at the length scale of the X-ray beam size, without clustering or segregation effects, as well as no presence of unintentional impurity incorporation along the single Zn:Co NWs. Through XRF quantification, the estimated Co concentrations were in the range from 0.2 at.% to 0.9 at.%, which were in good agreement with the values obtained from the simulations using the *iradina* Monte-Carlo Code.

- We reported for the first time nano-XAS measurements on single Co-implanted ZnO NWs. So far, the XAS technique had been mostly limited down to micrometer length scales because of the X-ray beam instability during the energy scan and chromaticity of the X-ray nanofocusing optics. For that reason, most of the local structural analyses on NWs had reported average interatomic distances over a macroscopic volume. In this dissertation, the nanoimaging endstation ID22NI allowed to explore phase separation effects and short range order in single Co-implanted ZnO NWs using XAS technique. The findings indicated the short-range structural disorder induced by an ion implantation process in single Co-implanted ZnO NWs, as well

2. CONCLUSIONS AND PERSPECTIVES

as the good recovery of the damaged structure through a post-implantation thermal annealing. In both cases, the tetrahedral structure remains all along the NWs. In addition, the use of the linear polarization of the synchrotron radiation made the XAS experiment not only element specific, but also capable of detecting preferential oriented nanodefects induced by the implantation process. Within the context of room temperature ferromagnetism in diluted magnetic semiconductors, the results reported here gave strong evidence of the substitutional incorporation of implanted Co transition metal into the ZnO host lattice.

- The thesis highlighted the lattice distortions associated to the ion implantation related defects along the NWs using nano-XRD. Our results provided new insights into the role of the unavoidable damage created by the ion implantation process in individual NWs. Such defects ultimately limit the use of semiconductor NWs.

- The micro-PL and CL results of single Co-implanted ZnO NWs corroborated the synchrotron nanoprobe-based findings, as well as confirmed the good optical activation of the implanted Co ions in ZnO NWs through the post-implantation thermal annealing.

2.2 Perspectives

X-ray excited optical luminescence on single ZnO:Co nanowires

Although preliminary optical properties of single Co-implanted ZnO NWs studied using micro-PL and CL were presented in this thesis, as well as in Ref. [48], a tool with higher spatial resolution such as XEOL is necessary to investigate the relationship between the electronic structure and compositional distribution within single Co-implanted ZnO NWs. In addition, polarization and time-resolved dependent PL of single NWs are very important for potential applications in polarization-sensitive devices [6, 7], which have not been completely studied yet. Thus, taking the advantage of the highly polarized and temporal structure of the synchrotron radiation source in combination with the polarization dependent and time-resolved XEOL detection at the nanometer length scale, the aim will be to obtain high-resolution luminescence maps of the degree of polarization and lifetime of the radiative transitions in single NWs. A proposal submitted last year (MA2212) has got beamtime allocation (15 shifts) in April and July 2014 at the new beamline ID16B.

X-ray beam induced current on single ZnO:Co nanowires

In a complementary way to XEOL, the XBIC in 2D can be used to study the spatial distribution of nonradiative centers, namely the recombination activity of impurities and defects in the ZnO:Co NWs. However, sample preparation for the XBIC measurements of single NWs is still critical. The electrical contacts in the NWs are still very challenging because they can be broken during the setup and measurement. It needs, therefore, a further improvement in the sample preparation in order to enable this measurement.

Conclusions en Français

Ce travail de thèse a montré l'utilisation combinée de nano-fluorescence des rayons X, nano-spectroscopie des rayons X, et des outils de nano-diffraction des rayons X pour étudier les nanofils de ZnO dopés au cobalt par implantation ionique. Ces trois techniques utilisent une haute résolution spatiale grâce à la focalisation par des miroirs KB multi-couches en faisceau "rose" ($60 \times 60 \text{ nm}^2$) et en faisceau monochromatique ($110 \times 110 \text{ nm}^2$). L'approche multi-techniques, s'appuyant sur l'utilisation d'une nanosonde de rayonnement synchrotron, a permis la caractérisation directe de la composition et de l'ordre structural à courte et grande distance des nanofils semi-conducteurs à l'échelle du nanomètre. Les résultats les plus pertinents sont:

- L'analyse des données de nano-XRF révèle une distribution homogène du zinc et du cobalt implanté dans la limite de la résolution du faisceau de rayons X, sans cluster ni effet de ségrégation, et sans aucune présence d'impuretés le long du nanofils ZnO:Co. Grâce à la quantification XRF, les concentrations de Co estimées sont de l'ordre de 0,2 at.% à 0,9 at.%, ce qui est en accord avec les valeurs obtenues à partir des simulations réalisées en utilisant le code Monte-Carlo *iradina*.

- Nous avons rapporté pour la première fois des mesures de nano-XAS sur nanofils de ZnO dopés au cobalt par implantation ionique. Jusqu'à présent, la technique XAS a été principalement limitée à des mesures micrométriques à cause de l'instabilité du faisceau de rayons X lors du balayage en l'énergie et de la chromaticité de l'optique de nanofocalisation des rayons X. Pour cette raison, la plupart des analyses structurales locales sur nanofils avaient montré des moyennes pour les distances interatomiques sur un volume macroscopique. Dans cette thèse, la station de nano-imagerie ID22NI a permis d'explorer les effets de séparation de phases et de l'ordre structural à courte distance dans les nanofils de ZnO dopés au cobalt par implantation ionique en utilisant la technique XAS. Les résultats indiquent un désordre structural à courte distance induit par le processus d'implantation ionique du cobalt dans les nanofils de ZnO, ainsi qu'une bonne récupération de la structure endommagée grâce à un recuit thermique après l'implantation. Dans les deux cas, la structure tétraédrique perdure tout au long du nanofil. En outre, l'utilisation de la polarisation linéaire du rayonnement synchrotron permet aux mesures XAS d'être non seulement discriminative au niveau des éléments chimiques détectés, mais également d'être capable de détecter les défauts nanométriques ayant des orientations préférentielles du fait du processus d'implantation. Dans le cadre des propriétés ferromagnétiques des semi-conducteurs

magnétiques dilués à température ambiante, les résultats présentés ici ont donné des preuves solides de l'incorporation par substitution du cobalt, métal de transition implanté dans le réseau cristallin du ZnO.

- La thèse a mis en évidence les distorsions du réseau cristallin associées aux défauts liés à l'implantation ionique dans les nanofils grâce à l'utilisation de la nano-diffraction par rayons X. Nos résultats ont fourni de nouvelles connaissances sur le rôle des dommages inévitables créés par le processus d'implantation ionique dans les nanofils. En définitive, de tels défauts limitent l'utilisation des nanofils semi-conducteurs.

- Les résultats de micro-PL et de CL de nanofils de ZnO dopés au cobalt par implantation ionique ont corroboré les conclusions obtenues grâce à la nanosonde de rayonnement, et ont confirmé la bonne activation optique des ions cobalt implantés dans les nanofils de ZnO par le recuit thermique post-implantation.

Perspectives en Français

Luminescence optique des rayons X excitée sur des nanofils ZnO:Co

Malgré les propriétés optiques préliminaires obtenues à l'aide de mesures par micro-PL et CL, et présentées dans cette thèse et en référence [48], sur des nanofils de ZnO dopés au cobalt par implantation ionique, un outil avec une résolution spatiale élevée comme le XEOL est nécessaire pour étudier la relation entre la structure électronique et la distribution de composition dans un nanofil de ZnO dopé au cobalt. En outre, les mesures de photo-luminescence résolues dans le temps et en fonction de la polarisation sur des nanofils n'ont pas encore été complètement étudiées alors que ces paramètres sont très importants pour des applications potentielles dans des appareils sensibles à la polarisation [6, 7]. Ainsi, en tirant profit de la structure hautement polarisée et temporelle de la source de rayonnement synchrotron pour de la détection XEOL dépendante de la polarisation et résolue en temps, à l'échelle du nanomètre, l'objectif sera d'obtenir des cartographies de luminescence à haute résolution du degré de polarisation et de la durée de vie des transitions radiatives dans les nanofils. Une demande de temps de faisceau présentée l'année dernière (MA2212) a abouti sur l'obtention de 15 sessions de 8h en Avril et Juillet 2014 sur la nouvelle ligne ID16B de l'ESRF.

2. CONCLUSIONS AND PERSPECTIVES

Courant induit par le faisceau de rayons X sur les nanofils ZnO:Co

En complément des mesures XEOL, les mesures en XBIC en 2D peuvent être utilisées pour étudier la distribution spatiale des centres non radiatifs, tel que par exemple l'activité de recombinaison des impuretés et des défauts dans les nanofils ZnO:Co. Cependant, la préparation des échantillons pour les mesures XBIC sur les nanofils est toujours critique. Les contacts électriques dans les nanofils sont encore très difficiles, car ils peuvent être brisés lors de l'alignement ou de la mesure. Il faut, par conséquent, améliorer la préparation de l'échantillon afin de permettre cette mesure.

References

- [1] A. I. Hochbaum and P. Yang, “Semiconductor nanowires for energy conversion,” *Chem. Rev.*, vol. 110, no. 1, p. 527, 2010.
- [2] M. Yazawa, M. Koguchi, A. Muto, M. Ozawa, and K. Hiruma, “Effect of one monolayer of surface gold atoms on the epitaxial growth of InAs nanowhiskers,” *Appl. Phys. Lett.*, vol. 61, no. 17, p. 2051, 1992.
- [3] M. Yazawa, M. Koguchi, A. Muto, and K. Hiruma, “Semiconductor nanowhiskers,” *Adv. Mater.*, vol. 5, no. 7-8, p. 577, 1993.
- [4] N. Elfström, R. Juhasz, I. Sychugov, T. Engfeldt, A. E. Karlström, and J. Linros, “Surface charge sensitivity of silicon nanowires: size dependence,” *Nano Lett.*, vol. 7, no. 9, p. 2608, 2007.
- [5] J. Wang, M. S. Gudiksen, X. Duan, Y. Cui, and C. M. Lieber, “Highly polarized photoluminescence and photodetection from single indium phosphide nanowires,” *Science*, vol. 293, no. 5534, p. 1455, 2001.
- [6] M. Montazeri, A. Wade, M. Fickenscher, H. E. Jackson, L. M. Smith, J. M. Yarrison-Rice, Q. Gao, H. H. Tan, and C. Jagadish, “Photomodulated rayleigh scattering of single semiconductor nanowires: Probing electronic band structure,” *Nano Lett.*, vol. 11, no. 10, p. 4329, 2011.
- [7] A. I. Singh, X. Li, V. Protasenko, G. Galantai, M. Kuno, H. G. Xing, and D. Jena, “Polarization-sensitive nanowire photodetectors based on solution-synthesized CdSe quantum-wire solids,” *Nano Lett.*, vol. 7, no. 10, p. 2999, 2007.
- [8] K. Tomioka, J. Motohisa, S. Hara, K. Hiruma, and T. Fukui, “GaAs/AlGaAs core multishell nanowire-based light-emitting diodes on Si,” *Nano Lett.*, vol. 10, no. 5, p. 1639, 2010.

REFERENCES

- [9] S. Xu, C. Xu, Y. Liu, Y. Hu, R. Yang, Q. Yang, J. H. Ryou, H. J. Kim, Z. Lochner, S. Choi, R. Dupuis, and Z. L. Wang, "Ordered nanowire array blue/near-UV light emitting diodes," *Adv. Mater.*, vol. 22, no. 42, p. 4749, 2010.
- [10] X. Jiang, Q. Xiong, S. Nam, F. Qian, Y. Li, and C. M. Lieber, "InAs/InP radial nanowire heterostructures as high electron mobility devices," *Nano Lett.*, vol. 7, no. 10, p. 3214, 2007.
- [11] H. Yan, H. S. Choe, S. Nam, Y. Hu, S. Das, J. F. Klemic, J. C. Ellenbogen, and C. M. Lieber, "Programmable nanowire circuits for nanoprocessors," *Nature*, vol. 470, no. 7333, p. 240, 2011.
- [12] B. Tian, T. Cohen-Karni, Q. Qing, X. Duan, P. Xie, and C. M. Lieber, "Three-dimensional, flexible nanoscale field-effect transistors as localized bioprobes," *Science*, vol. 329, no. 5993, p. 830, 2010.
- [13] M. D. Kelzenberg, D. B. Turner-Evans, B. M. Kayes, M. A. Filler, M. C. Putnam, N. S. Lewis, and H. A. Atwater, "Photovoltaic measurements in single-nanowire Silicon solar cells," *Nano Lett.*, vol. 8, no. 2, p. 710, 2008.
- [14] E. S. Liu, J. Nah, K. M. Varahramyan, and E. Tutuc, "Lateral spin injection in Germanium nanowires," *Nano Lett.*, vol. 10, no. 9, p. 3297, 2010.
- [15] D. D. Awschalom and M. E. Flatte, "Challenges for semiconductor spintronics," *Nat. Phys.*, vol. 3, no. 3, p. 153, 2007.
- [16] C. Gould, K. Pappert, G. Schmidt, and L. Molenkamp, "Magnetic anisotropies and (Ga,Mn)As-based spintronic devices," *Adv. Mater.*, vol. 19, no. 3, p. 323, 2007.
- [17] R. Yan, D. Gargas, P. Yang, and L. Molenkamp, "Nanowires photonics," *Nat. Photonics*, vol. 3, no. 10, p. 569, 2009.
- [18] F. Qian, Y. Li, S. Gradecak, H.-W. Park, Y. Dong, Z. L. Wang, and C. M. Lieber, "Multi-quantum-well nanowire heterostructures for wavelength-controlled lasers," *Nat. Mater.*, vol. 7, no. 9, p. 701, 2008.
- [19] J. Zhou, Y. Ding, S. Deng, L. Gong, N. Xu, and Z. Wang, "Three-dimensional tungsten oxide nanowire networks," *Adv. Mater.*, vol. 17, no. 17, p. 2107, 2005.

-
- [20] X. D. Wang, C. J. Summers, and Z. L. Wang, “Large-scale hexagonal-patterned growth of aligned ZnO nanorods for nano-optoelectronics and nanosensor arrays,” *Nano Lett.*, vol. 4, no. 3, p. 423, 2004.
- [21] P. Yang, R. Yan, and M. Fardy, “Semiconductor nanowire: What’s next?,” *Nano Lett.*, vol. 10, no. 5, p. 1529, 2010.
- [22] V. A. Coleman and C. Jagadish, “Basic properties and applications of ZnO,” in *Zinc oxide bulk, thin films and nanostructures* (c. Jagadish and S. J. Pearton, eds.), Amsterdam, Oxford: Elsevier, 2006.
- [23] C. Klingshirn, J. Fallert, H. Zhou, J. Sartor, C. Thiele, F. Maier-Flaig, D. Schneider, and H. Kalt, “65 years of ZnO research – old and very recent results,” *phys. status solidi (b)*, vol. 247, no. 6, p. 1424, 2010.
- [24] M. A. Zimmler, D. Stichtenoth, C. Ronning, W. Yi, V. Narayanamurti, T. Voss, and F. Capasso, “Scalable fabrication of nanowire photonic and electronic circuits using spin-on glass,” *Nano Lett.*, vol. 8, no. 6, p. 1695, 2008.
- [25] T. Voss, G. T. Svacha, E. Mazur, S. Müller, C. Ronning, D. Konjhodzic, and F. Marlow, “High-order waveguide modes in ZnO nanowires,” *Nano Lett.*, vol. 7, no. 12, p. 3675, 2007.
- [26] J. Bao, M. A. Zimmler, F. Capasso, X. Wang, and Z. F. Ren, “Broadband zno single-nanowire light-emitting diode,” *Nano Lett.*, vol. 6, no. 8, p. 1719, 2006.
- [27] T. Voss, G. T. Svacha, E. Mazur, S. Müller, and C. Ronning, “The influence of local heating by nonlinear pulsed laser excitation on the transmission characteristics of a ZnO nanowire waveguide,” *Nanotechnology*, vol. 20, no. 9, p. 095702, 2009.
- [28] M. A. Zimmler, J. Bao, F. Capasso, S. Müller, and C. Ronning, “Laser action in nanowires: Observation of the transition from amplified spontaneous emission to laser oscillation,” *Appl. Phys. Lett.*, vol. 93, no. 5, p. 051101, 2008.
- [29] M. A. Zimmler, F. Capasso, S. Müller, and C. Ronning, “Optically pumped nanowire lasers: invited review,” *Semicond. Sci. Technol.*, vol. 25, no. 2, p. 024001, 2010.
- [30] Wikipedia, “Wurtzite crystal structure — wikipedia, the free encyclopedia,” 2013.

REFERENCES

- [31] S. Bloom and I. Ortenburger, “Pseudopotential band structure of ZnO,” *phys. status solidi (b)*, vol. 58, no. 2, p. 561, 1973.
- [32] D. Vogel, P. Krüger, and J. Pollmann, “*Ab initio* electronic-structure calculations for II-VI semiconductors using self-interaction-corrected pseudopotentials,” *Phys. Rev. B*, vol. 52, no. 20, p. R14316, 1995.
- [33] I. Ivanov and J. Pollmann, “Electronic structure of ideal and relaxed surfaces of zno: A prototype ionic wurtzite semiconductor and its surface properties,” *Phys. Rev. B*, vol. 24, no. 12, p. 7275, 1981.
- [34] U. Rössler, “Energy bands of hexagonal II-VI semiconductors,” *Phys. Rev.*, vol. 184, no. 3, p. 733, 1969.
- [35] M. Usuda, N. Hamada, T. Kotani, and M. van Schilfgaarde, “All-electron GW calculation based on the LAPW method: application to wurtzite ZnO,” *Phys. Rev. B*, vol. 66, no. 12, p. 125101, 2002.
- [36] B. K. Meyer, H. Alves, D. M. Hofmann, W. Kriegseis, D. Forster, F. Bertram, J. Christen, A. Hoffmann, M. Straßburg, M. Dworzak, U. Habocek, and A. V. Rodina, “Bound exciton and donor–acceptor pair recombinations in ZnO,” *phys. status solidi (b)*, vol. 241, no. 2, p. 231, 2004.
- [37] H. Morkoç and U. Özgür, “General properties of zno,” in *Zinc Oxide: Fundamentals, Materials and Device Technology*, Weinheim, Germany: Wiley-VCH Verlag GmbH & Co. KGaA, 2009.
- [38] U. Özgür, Y. I. Alivov, C. Liu, A. Teke, M. A. Reshchikov, S. Doğan, V. Avrutin, S.-J. Cho, and H. Morkoç, “A comprehensive review of ZnO materials and devices,” *J. Appl. Phys.*, vol. 98, no. 4, p. 041301, 2005.
- [39] U. Özgür and H. Morkoç, “Optical properties of ZnO and related alloys,” in *Zinc oxide bulk, thin films and nanostructures* (c. Jagadish and S. J. Pearton, eds.), Amsterdam, Oxford: Elsevier, 2006.
- [40] T. J. Kempa, B. Tian, D. R. Kim, J. Hu, X. Zheng, and C. M. Lieber, “Single and tandem axial p-i-n nanowire photovoltaic devices,” *Nano Lett.*, vol. 8, no. 10, p. 3456, 2008.

-
- [41] E. D. Minot, F. Kelkensberg, M. van Kouwen, J. A. van Dam, L. P. Kouwenhoven, V. Zwiller, M. T. Borgström, O. Wunnicke, M. A. Verheijen, and E. P. A. M. Bakkers, “Single quantum dot nanowire LEDs,” *Nano Lett.*, vol. 7, no. 2, p. 367, 2007.
- [42] J. B. Cui and U. J. Gibson, “Electrodeposition and room temperature ferromagnetic anisotropy of Co and Ni-doped ZnO nanowire arrays,” *Appl. Phys. Lett.*, vol. 87, no. 13, p. 133108, 2005.
- [43] T. Dietl, “A ten-year perspective on dilute magnetic semiconductor oxides,” *Nature Mater.*, vol. 9, no. 12, p. 965, 2010.
- [44] S. Müller, M. Zhou, Q. Li, and C. Ronning, “Intra-shell luminescence of transition-metal-implanted zinc oxide nanowires,” *Nanotechnology*, vol. 20, no. 13, p. 135704, 2009.
- [45] P. Koidl, “Optical absorption of Co^{2+} in ZnO,” *Phys. Rev. B*, vol. 15, no. 5, p. 2493, 1977.
- [46] H. A. Weakliem, “Optical spectra of Ni^{2+} , Co^{2+} , and Cu^{2+} in tetrahedral sites in crystals,” *J. Chem. Phys.*, vol. 36, no. 8, p. 2117, 1962.
- [47] E. Malguth, A. Hoffmann, and M. R. Phillips, “Fe in III–V and II–VI semiconductors,” *phys. status solidi (b)*, vol. 245, no. 3, p. 455, 2008.
- [48] S. Geburt, *Lasing and ion beam doping of semiconductor nanowires*. PhD thesis, University of Jena, 2013.
- [49] R. O. Kuzian, A. M. Daré, P. Sati, and R. Hayn, “Crystal-field theory of Co^{2+} in doped ZnO,” *Phys. Rev. B*, vol. 74, no. 15, p. 155201, 2006.
- [50] J. Segura-Ruiz, *Electronic and Vibrational States of InN and GaInN Nanocolumns*. PhD thesis, University of Valencia, 2009.
- [51] J. Wu, W. Walukiewicz, K. M. Yu, J. W. Ager, E. E. Haller, H. Lu, and W. J. Schaff, “Small band gap bowing in $\text{In}_{1-x}\text{Ga}_x\text{N}$ alloys,” *Appl. Phys. Lett.*, vol. 80, no. 25, p. 4741, 2002.
- [52] J. Wu, W. Walukiewicz, K. M. Yu, W. Shan, J. W. Ager, E. E. Haller, H. Lu, W. J. Schaff, W. K. Metzger, and S. Kurtz, “Superior radiation resistance of $\text{In}_{1-x}\text{Ga}_x\text{N}$ alloys: Full-solar-spectrum photovoltaic material system,” *J. Appl. Phys.*, vol. 94, no. 10, p. 6477, 2003.

REFERENCES

- [53] X. Chen, K. D. Matthews, D. Hao, W. J. Schaff, and L. F. Eastman, “Growth, fabrication, and characterization of InGaN solar cells,” *phys. status solidi (a)*, vol. 205, no. 5, p. 1103, 2008.
- [54] J. Phillips, M. Coltrin, M. Crawford, A. Fischer, M. Krames, R. Mueller-Mach, G. Mueller, Y. Ohno, L. Rohwer, J. Simmons, and J. Tsao, “Research challenges to ultra-efficient inorganic solid-state lighting,” *Laser Photon. Rev.*, vol. 1, no. 4, p. 307, 2007.
- [55] A. Khan, “Semiconductor photonics: Laser diodes go green,” *Nat. Photon.*, vol. 3, no. 8, p. 432, 2009.
- [56] S. L. Howell, S. Padalkar, K. Yoon, Q. Li, D. D. Koleske, J. J. Wierer, G. T. Wang, and L. J. Lauhon, “Spatial mapping of efficiency of GaN/InGaN nanowire array solar cells using scanning photocurrent microscopy,” *Nano Lett.*, vol. 13, no. 11, p. 5123, 2013.
- [57] F. Qian, S. Gradecak, Y. Li, C.-Y. Wen, and C. M. Lieber, “Core/multishell nanowire heterostructures as multicolor, high-efficiency light-emitting diodes,” *Nano Lett.*, vol. 5, no. 11, pp. 2287–2291, 2005.
- [58] N. S. Lewis, “Toward cost-effective solar energy use,” *Science*, vol. 315, no. 5813, pp. 798–801, 2007.
- [59] B. Tian, X. Zheng, T. J. Kempa, Y. Fang, N. Yu, G. Yu, J. Huang, and C. M. Lieber, “Coaxial silicon nanowires as solar cells and nanoelectronic power sources,” *Nature*, vol. 449, no. 7164, p. 885, 2007.
- [60] G. Tourbot, C. Bougerol, A. Grenier, M. D. Hertog, D. Sam-Giao, D. Cooper, P. Gilet, B. Gayral, and B. Daudin, “Structural and optical properties of InGaN/GaN nanowire heterostructures grown by PA-MBE,” *Nanotechnology*, vol. 22, no. 7, p. 075601, 2011.
- [61] F. Limbach, T. Gotschke, T. Stoica, R. Calarco, E. Sutter, J. Ciston, R. Cusco, L. Artus, S. Kremling, S. Höfling, L. Worschech, and D. Grützmacher, “Structural and optical properties of InGaN–GaN nanowire heterostructures grown by molecular beam epitaxy,” *J. Appl. Phys.*, vol. 109, no. 1, p. 014309, 2011.
- [62] T. Kuykendall, P. Ulrich, S. Aloni, and P. Yang, “Complete composition tunability of InGaN nanowires using a combinatorial approach,” *Nat Mater*, vol. 6, no. 12, p. 951, 2007.

REFERENCES

- [63] H.-M. Kim, Y.-H. Cho, H. Lee, S. I. Kim, S. R. Ryu, D. Y. Kim, T. W. Kang, and K. S. Chung, “High-brightness light emitting diodes using dislocation-free indium gallium nitride/gallium nitride multi-quantum-well nanorod arrays,” *Nano Lett.*, vol. 4, no. 6, p. 1059, 2004.
- [64] J. Segura-Ruiz, G. Martínez-Criado, J. A. Sans, R. Tucoulou, P. Cloetens, I. Snigireva, C. Denker, J. Malindretos, A. Rizzi, M. Gomez-Gomez, N. Garro, and A. Cantarero, “Direct observation of elemental segregation in InGaN nanowires by X-ray nanoprobe,” *phys. status solidi-RRL*, vol. 5, no. 3, pp. 95–97, 2011.
- [65] H. J. Choi, “Vapor–liquid–solid growth of semiconductor nanowire,” in *Semiconductor Nanostructures for Optoelectronic Devices* (G.-C. Yi, ed.), Springer, 2012.
- [66] R. S. Wagner and W. C. Ellis, “Vapor liquid solid mechanism of single crystal growth,” *Appl. Phys. Lett.*, vol. 4, no. 5, p. 89, 1964.
- [67] C. Borschel and C. Ronning, “Ion beam irradiation of nanostructures – a 3d monte carlo simulation code,” *Nucl. Instrum. Methods Phys. Res. B*, vol. 269, no. 19, p. 2133, 2011.
- [68] C. Ronning, C. Borschel, S. Geburt, and R. Niepelt, “Ion beam doping of semiconductor nanowires,” *Mater. Sci. Eng., R*, vol. 70, no. 3–6, p. 30, 2010.
- [69] J. Segura-Ruiz, G. Martínez-Criado, M. H. Chu, C. Denker, J. Malindretos, and A. Rizzi, “Synchrotron nanoimaging of single In-rich InGaN nanowires,” *J. Appl. Phys.*, vol. 113, no. 13, p. 136511, 2013.
- [70] J. Segura-Ruiz, N. Garro, A. Cantarero, C. Denker, J. Malindretos, and A. Rizzi, “Optical studies of MBE-grown InN nanocolumns: Evidence of surface electron accumulation,” *Phys. Rev. B*, vol. 79, no. 11, p. 115305, 2009.
- [71] F. R. Elder, A. M. Gurewitsch, R. V. Langmuir, and H. C. Pollock, “Radiation from electrons in a synchrotron,” *Phys. Rev.*, vol. 71, no. 11, p. 829, 1947.
- [72] Wikipedia, “Synchrotron light source — wikipedia, the free encyclopedia,” 2013.
- [73] ESRF, “A light for science—at www.esrf.eu,”
- [74] H. Motz, “Applications of the radiation from fast electron beams,” *J. Appl. Phys.*, vol. 22, no. 5, p. 527, 1951.

REFERENCES

- [75] E. Kosior, *Combined phase and X-ray fluorescence imaging at the sub-cellular level*. PhD thesis, University of Grenoble, 2013.
- [76] ESRFwebsite, “Brilliance,” 2013.
- [77] D. H. Bilderback, P. Elleaume, and E. Weckert, “Review of third and next generation synchrotron light sources,” *J. Phys. B: At. Mol. Opt. Phys.*, vol. 38, no. 9, p. S773, 2005.
- [78] G. Schütz, W. Wagner, W. Wilhelm, P. Kienle, R. Zeller, R. Frahm, and G. Materlik, “Absorption of circularly polarized X rays in iron,” *Phys. Rev. Lett.*, vol. 58, no. 7, p. 737, 1987.
- [79] J. Segura-Ruiz, G. Martínez-Criado, M. H. Chu, S. Geburt, and C. Ronning, “Nano-x-ray absorption spectroscopy of single Co-implanted ZnO nanowires,” *Nano Lett.*, vol. 11, no. 12, p. 5322, 2011.
- [80] G. Martínez-Criado, E. Borfecchia, L. Mino, and C. Lamberti, “Micro- and nano-X-ray beams,” in *Characterization of Semiconductor Heterostructures and Nanostructures (Second Edition)* (G. Agostini and C. Lamberti, eds.), Elsevier, 2013.
- [81] G. E. Ice, J. D. Budai, and J. W. L. Pang, “The race to x-ray microbeam and nanobeam science,” *Science*, vol. 334, no. 6060, p. 1234, 2011.
- [82] C. Morawe and M. Osterhoff, “Hard x-ray focusing with curved reflective multilayers,” *X-Ray Optics and Instrumentation*, vol. 2010, p. 479631, 2010.
- [83] K. Yamauchi, H. Mimura, T. Kimura, H. Yumoto, S. Handa, S. Matsuyama, K. Arima, Y. Sano, K. Yamamura, K. Inagaki, H. Nakamori, J. Kim, K. Tamasaku, Y. Nishino, M. Yabashi, and T. Ishikawa, “Single-nanometer focusing of hard x-rays by Kirkpatrick–Baez mirrors,” *J. Phys: Condens. Matter*, vol. 23, no. 39, p. 394206, 2011.
- [84] A. Snigirev, V. Kohn, I. Snigireva, and B. Lengeler, “A compound refractive lens for focusing high-energy X-rays,” *Nature*, vol. 384, no. 6604, p. 49, 1996.
- [85] A. Snigirev and I. Snigireva, “High energy X-ray micro-optics,” *C. R. Phys.*, vol. 9, no. 5–6, p. 507, 2008.

REFERENCES

- [86] W. Chao, B. D. Harteneck, J. A. Liddle, E. H. Anderson, and D. T. Attwood, “Soft X-ray microscopy at a spatial resolution better than 15 nm,” *Nature*, vol. 435, no. 7046, p. 1210, 2005.
- [87] W. Chao, P. Fischer, T. Tyliczszak, S. Rekawa, E. Anderson, and P. Naulleau, “Real space soft X-ray imaging at 10 nm spatial resolution,” *Opt. Express*, vol. 20, no. 9, p. 9777, 2012.
- [88] D. H. Bilderback, S. A. Hoffman, and D. J. Thiel, “Nanometer spatial resolution achieved in hard x-ray imaging and laue diffraction experiments,” *Science*, vol. 263, no. 5144, p. 201, 1994.
- [89] R. Huang and D. H. Bilderback, “Single-bounce monocrystals for focusing synchrotron radiation: modeling, measurements and theoretical limits,” *J. Synchrot. Radiat.*, vol. 13, no. 1, p. 74, 2006.
- [90] H. C. Kang, J. Maser, G. B. Stephenson, C. Liu, R. Conley, A. T. Macrander, and S. Vogt, “Nanometer linear focusing of hard X rays by a multilayer Laue lens,” *Phys. Rev. Lett.*, vol. 96, no. 12, p. 127401, 2006.
- [91] H. C. Kang, H. Yan, R. P. Winarski, M. V. Holt, J. Maser, C. Liu, R. Conley, S. Vogt, A. T. Macrander, and G. B. Stephenson, “Focusing of hard x-rays to 16 nanometers with a multilayer Laue lens,” *Appl. Phys. Lett.*, vol. 92, no. 22, p. 221114, 2008.
- [92] C. G. Schroer and B. Lengeler, “Focusing hard X rays to nanometer dimensions by adiabatically focusing lenses,” *Phys. Rev. Lett.*, vol. 94, no. 5, p. 054802, 2005.
- [93] A. F. Isakovic, A. Stein, J. B. Warren, S. Narayanan, M. Sprung, A. R. Sandy, and K. Evans-Lutterodt, “Diamond kinoform hard X-ray refractive lenses: design, nanofabrication and testing,” *J. Synchrot. Radiat.*, vol. 16, no. 1, p. 8, 2009.
- [94] J. Als-Nielsen and D. McMorrow, “Elements of modern x-ray physics (second edition),” JohnWiley & Sons, 2001.
- [95] R. Tucoulou, G. Martinez-Criado, P. Bleuet, I. Kieffer, P. Cloetens, S. Labouré, T. Martin, C. Guilloud, and J. Susini, “High-resolution angular beam stability monitoring at a nanofocusing beamline,” *J. Synchrotron Radiat.*, vol. 15, no. 4, p. 392, 2008.

REFERENCES

- [96] M. G. Honnicke, J. W. Keister, R. Conley, K. Kaznatcheev, P. Z. Takacs, D. S. Coburn, L. Reffi, and Y. Q. Cai, "Synchrotron X-ray tests of an L-shaped laterally graded multilayer mirror for the analyzer system of the ultra-high-resolution IXS spectrometer at NSLS-II," *J. Synchrotron Radiat.*, vol. 18, no. 6, p. 862, 2011.
- [97] P. Kirkpatrick and A. V. Baez, "Formation of optical images by x-rays," *J. Opt. Soc. Am.*, vol. 38, no. 9, p. 766, 1948.
- [98] C. Morawe, P. Pecci, J. C. Peffen, and E. Ziegler, "Design and performance of graded multilayers as focusing elements for X-ray optics," *Rev. of Sci. Instrum.*, vol. 70, no. 8, p. 3227, 1999.
- [99] H. Mimura, S. Handa, T. Kimura, H. Yumoto, D. Yamakawa, H. Yokoyama, S. Matsuyama, K. Inagaki, K. Yamamura, Y. Sano, K. Tamasaku, Y. Nishino, M. Yabashi, T. Ishikawa, and K. Yamauchi, "Breaking the 10[thinsp]nm barrier in hard-X-ray focusing," *Nat. Phys.*, vol. 6, no. 2, p. 122, 2010.
- [100] "Handbook of x-ray spectrometry, practical spectroscopy series," vol. 29, Marcel Dekker, New York, 2002.
- [101] P. Brouwer, "Theory of XRF," PANalytical B.V, Almelo, Netherlands, 2010.
- [102] Wikipedia, "Atomic orbital," 2014.
- [103] Wikipedia, "Quantum number," 2014.
- [104] Wikipedia, "Auger electron spectroscopy," 2007.
- [105] P. Persson, S. Lunell, A. Szöke, B. Ziaja, and J. Hajdu, "Shake-up and shake-off excitations with associated electron losses in X-ray studies of proteins," *Protein Sci.*, vol. 10, p. 2480, 2001.
- [106] M. O. Krause and J. H. Oliver, "Natural widths of atomic K and L levels, $K\alpha$ x-ray lines and several K L L Auger lines," *J. Phys. Chem.l Ref. Data*, vol. 8, p. 329, 1979.
- [107] B. Arezki, "X-ray fluorescence: Energy-dispersive analysi (EDXRF)," in <http://www.physik.uni-siegen.de>, Advanced Physics Laboratory.
- [108] Wikipedia, "Selection rule," 2014.

REFERENCES

- [109] R. Sitko and B. Zawiszai, “Quantification in X-ray fluorescence spectrometry,” in *X-ray spectroscopy* (S. K. Sharma, ed.), InTech, 2012.
- [110] G. Falkenberg and K. Rickers, “Pink-beam and monochromatic micro-X-ray fluorescence analysis at the beamline L,” *Hasylab Annual Report*, p. 88, 2002.
- [111] A. Somogyi, R. Tucoulou, G. Martínez-Criado, A. Homs, J. Cauzid, P. Bleuet, S. Bohic, and A. Simionovici, “ID22: a multitechnique hard X-ray microprobe beamline at the European Synchrotron Radiation Facility,” *J. Synchrotron Radiat.*, vol. 12, p. 208, 2005.
- [112] G. Martínez-Criado, R. Tucoulou, P. Cloetens, P. Bleuet, S. Bohic, J. Cauzid, I. Kieffer, E. Kosior, S. Labouré, S. Petitgirard, A. Rack, J. A. Sans, J. Segura-Ruiz, H. Suhonen, J. Susini, and J. Villanova, “Status of the hard X-ray microprobe beamline ID22 of the European Synchrotron Radiation Facility,” *J. Synchrotron Radiat.*, vol. 19, no. 1, p. 10, 2012.
- [113] EDAX, “Defining silicon drift detector performance,” Insight Newsletter-EDAX—[http : //www.edax.com/mobile/news_events/newsletter.aspx](http://www.edax.com/mobile/news_events/newsletter.aspx), 2012.
- [114] V. Solé, E. Papillon, M. Cotte, P. Walter, and J. Susini, “A multiplatform code for the analysis of energy-dispersive X-ray fluorescence spectra,” *Spectrochim. Acta, Part B*, vol. 62, no. 1, p. 63, 2007.
- [115] D. C. Koningsberger and R. Prins, “X-ray absorption: Principles, applications, techniques of EXAFS, SEXAFS and XANES,” JohnWiley & Sons, 1988.
- [116] M. Newville, “Fundamentals of XAFS-xasf.org,” 2004.
- [117] G. Bunker, “Introduction to XAFS a practical guide to X-ray absorption fine structure spectroscopy,” Cambridge University Press, 2010.
- [118] T. Busgen, M. Hilgendorff, S. Irsen, F. Wilhelm, A. Rogalev, D. Goll, and M. Giersig, “Colloidal cobalt-doped ZnO nanorods: Synthesis, structural, and magnetic properties,” *J. Phys. Chem. C*, vol. 112, no. 7, p. 2412, 2008.
- [119] Chemwiki, “Xanes:theory,” 2013.
- [120] T. Ressler, S. L. Brock, J. Wong, and S. L. Suib, “Structural studies on colloidal tetraalkylammonium manganese oxides,” *J. Synchrotron. Radiat.*, vol. 6, no. 3, p. 728, 1999.

REFERENCES

- [121] A. Bianconi, “Xanes spectroscopy for local structures in complex systems,” in *EXAFS and Near Edge Structure*, vol. 12, pp. 118–129, Springer Berlin Heidelberg, 1983.
- [122] J. E. Penner-Hahn, “X-ray absorption spectroscopy,” in *eLS*, John Wiley & Sons, Ltd, 2001.
- [123] M. J. Fay, A. Proctor, D. P. Hoffmann, and D. M. Hercules, “Unraveling EXAFS spectroscopy,” *Analytical Chemistry*, vol. 60, no. 21, p. 1225A, 1988.
- [124] E. A. Stern, D. E. Sayers, and F. W. Lytle, “Extended x-ray-absorption fine-structure technique.III. determination of physical parameters,” *Phys. Rev. B*, vol. 11, no. 12, p. 4836, 1975.
- [125] P. A. Lee and J. B. Pendry, “Theory of the extended x-ray absorption fine structure,” *Phys. Rev. B*, vol. 11, no. 8, pp. 2795–2811, 1975.
- [126] M. Newville, “*IFEFFIT*: interactive XAFS analysis and *FEFF* fitting,” *J. Synchrotron Radiat.*, vol. 8, no. 2, p. 322, 2001.
- [127] B. Ravel and M. Newville, “*ATHENA*, *ARTEMIS*, *HEPHAESTUS*: data analysis for X-ray absorption spectroscopy using *IFEFFIT*,” *J. Synchrotron Radiat.*, vol. 12, no. 4, pp. 537–, 2005.
- [128] A. L. Ankudinov, B. Ravel, J. J. Rehr, and S. D. Conradson, “Real-space multiple-scattering calculation and interpretation of x-ray-absorption near-edge structure,” *Phys. Rev. B*, vol. 58, no. 12, p. 7565, 1998.
- [129] A. Zeuner, H. Alves, D. M. Hofmann, B. K. Meyer, M. Heuken, J. Bläsing, and A. Krost, “Structural and optical properties of epitaxial and bulk ZnO,” *Appl. Phys. Lett.*, vol. 80, no. 12, p. 2078, 2002.
- [130] N. W. Ashcroft and N. D. Mermin, *The reciprocal lattice*. Cengage Learning, Inc, 1976.
- [131] B. B. He, *Two-dimensional X-Ray Diffraction*. Wiley, 2009.
- [132] B. D. Cullity, *Elements of X-ray diffraction*. Addison-Wesley, 1978.

REFERENCES

- [133] J.-C. Labiche, O. Mathon, S. Pascarelli, M. A. Newton, G. G. Ferre, C. Curfs, G. Vaughan, A. Homs, and D. F. Carreiras, “Invited article: The fast readout low noise camera as a versatile x-ray detector for time resolved dispersive extended x-ray absorption fine structure and diffraction studies of dynamic problems in materials science, chemistry, and catalysis,” *Rev. Sci. Instrum.*, vol. 78, no. 9, p. 091301, 2007.
- [134] A. P. Hammersley, S. O. Svensson, A. Thompson, H. Graafsma, A. Kvick, and J. P. Moy, “Calibration and correction of distortions in two dimensional detector systemsa),” *Rev. Sci. Instrum.*, vol. 66, no. 3, p. 2729, 1995.
- [135] A. P. Hammersley, S. O. Svensson, M. Hanfland, A. N. Fitch, and D. Hausermann, “Two-dimensional detector software: From real detector to idealised image or two-theta scan,” *High Pressure Research*, vol. 14, no. 4-6, p. 235, 1996.
- [136] S. Geburt, R. Röder, U. Kaiser, L. Chen, M.-H. Chu, J. Segura-Ruiz, G. Martínez-Criado, W. Heimbrodtt, and C. Ronning, “Intense intra-3d luminescence and waveguide properties of single Co-doped ZnO nanowires,” *phys. status solidi– RRL*, vol. 7, no. 10, p. 886, 2013.
- [137] S. Geburt, A. Thielmann, R. Röder, C. Borschel, A. McDonnell, M. Kozlik, J. Kühnel, K. A. Sunter, F. Capasso, and C. Ronning, “Low threshold room-temperature lasing of CdS nanowires,” *Nanotechnology*, vol. 23, no. 36, p. 365204, 2012.
- [138] L. Chen, T. Niebling, W. Heimbrodtt, D. Stichtenoth, C. Ronning, and P. J. Klar, “Dimensional dependence of the dynamics of the Mn $3d^5$ luminescence in (Zn, Mn)S nanowires and nanobelts,” *Phys. Rev. B*, vol. 76, no. 11, p. 115325, 2007.
- [139] B. D. Yuhas, D. O. Zitoun, P. J. Pauzauskie, R. He, and P. Yang, “Transition-metal doped zinc oxide nanowires,” *Angew. Chem.*, vol. 45, no. 3, p. 420, 2006.
- [140] D. S. D. S. C. Borchers, S. Müller and C. Ronning, “Catalyst–nanostructure interaction in the growth of 1-D ZnO nanostructures,” *J. Phys. Chem. B*, vol. 110, no. 4, p. 1656, 2006.
- [141] D. E. Perea, E. R. Hemesath, E. J. Schwalbach, J. L. Lensch-Falk, P. W. Voorhees, and L. J. Lauhon, “Direct measurement of dopant distribution in

REFERENCES

- an individual vapour-liquid-solid nanowire,” *Nature Nanotechnol.*, vol. 4, no. 5, pp. 315–319, 2009.
- [142] R. Lide, *CRC Handbook of Chemistry and Physics*. CRC Press, Boca Raton, Florida, USA, 1996, 1996.
- [143] A. Y. Azarov, B. G. Svensson, and A. Y. Kuznetsov, “Impurity-limited lattice disorder recovery in ion-implanted ZnO,” *Appl. Phys. Lett.*, vol. 101, no. 22, p. 222109, 2012.
- [144] A. Nadarajah and R. Könenkamp, “Dilute magnetic semiconductors from electrodeposited ZnO nanowires,” *phys. status solidi (b)*, vol. 248, no. 2, p. 334, 2011.
- [145] C. Y. Lin, W. H. Wang, C.-S. Lee, K. W. Sun, and Y. W. Suen, “Magnetophotoluminescence properties of Co-doped ZnO nanorods,” *Appl. Phys. Lett.*, vol. 94, no. 15, p. 151909, 2009.
- [146] E.-A. Choi, W.-J. Lee, and K. J. Chang, “Enhanced electron-mediated ferromagnetism in Co-doped ZnO nanowires,” *J. Appl. Phys.*, vol. 108, no. 2, p. 023904, 2010.
- [147] S. Deka and P. Joy, “Synthesis and magnetic properties of Mn doped ZnO nanowires,” *Solid State Commun.*, vol. 142, no. 4, p. 190, 2007.
- [148] A. Mourachkine, O. V. Yazyev, C. Ducati, and J.-P. Ansermet, “Template nanowires for spintronics applications: Nanomagnet microwave resonators functioning in zero applied magnetic field,” *Nano Lett.*, vol. 8, no. 11, p. 3683, 2008.
- [149] J. C. Sankey, P. M. Braganca, A. G. F. Garcia, I. N. Krivorotov, R. A. Buhrman, and D. C. Ralph, “Spin-transfer-driven ferromagnetic resonance of individual nanomagnets,” *Phys. Rev. Lett.*, vol. 96, no. 22, p. 227601, 2006.
- [150] B. D. Yuhas, S. Fakra, M. A. Marcus, and P. Yang, “Probing the local coordination environment for transition metal dopants in zinc oxide nanowires,” *Nano Lett.*, vol. 7, no. 4, pp. 905–909, 2007.
- [151] J. Cui and U. Gibson, “Thermal modification of magnetism in cobalt-doped ZnO nanowires grown at low temperature,” *Phys. Rev. B*, vol. 74, no. 4, p. 045416, 2006.

REFERENCES

- [152] L. Liao, J. C. Li, D. F. Wang, C. Liu, M. Z. Peng, and J. M. Zhou, "Size dependence of Curie temperature in Co⁺ ion implanted ZnO nanowires," *Nanotechnology*, vol. 17, no. 3, p. 830, 2006.
- [153] Y. Shen, J.-I. Hong, Z. Peng, H. Fang, S. Zhang, S. Dong, R. L. Snyder, and Z. L. Wang, "Tuning the shape and strain in micro/nanowires by a sideways physical deposition process," *J. Phys. Chem. C*, vol. 114, no. 49, p. 21277, 2010.
- [154] S.-H. Park, S.-H. Kim, and S.-W. Han, "Structural properties of nitrogen-ion implanted zno nanorods," *J. Korean Phys. Soc.*, vol. 50, p. 1557, 2007.
- [155] Y.-B. Lee, C.-H. Kwak, S.-Y. Seo, S.-H. Kim, C.-I. Park, K. B.-H., S.-H. Park, Y.-D. Choi, and S.-W. Han, "Structural and optical properties of hydrogen-ion-implanted znonanorods," *J. Korean Phys. Soc.*, vol. 56, p. 2050, 2010.
- [156] C.-H. Kwak, Y.-B. Lee, S.-Y. Seo, S.-H. Kim, C.-I. Park, B.-H. Kim, D.-W. Jeong, J.-J. Kim, Z. Jin, and S.-W. Han, "Structural and electrical properties of nitrogen-ion implanted zno nanorods," *Curr. Appl. Phys.*, vol. 11, no. 3, Supplement, p. S328, 2011.

REFERENCES

Part II

Dissertation related papers

3

Synchrotron fluorescence nanoimaging of a single Co-implanted ZnO nanowire

M. H. Chu, G. Martínez-Criado, J. Segura-Ruiz, P. Cloetens, I. Snigireva, S. Geburt,
and C. Ronning



Synchrotron fluorescence nanoimaging of a single Co-implanted ZnO nanowire

M. H. Chu¹, J. Segura-Ruiz^{*1}, G. Martinez-Criado¹, P. Cloetens¹, I. Snigireva¹, S. Geburt², and C. Ronning²

¹ European Synchrotron Radiation Facility, Experiments Division, 38043 Grenoble, France

² Institute of Solid State Physics, University of Jena, 07743 Jena, Germany

Received 8 June 2011, revised 24 June 2011, accepted 30 June 2011

Published online 5 July 2011

Keywords ZnO, diluted magnetic semiconductors, nanowires, X-ray fluorescence

* Corresponding author: e-mail seguraru@esrf.fr

In this study, we report the application of synchrotron radiation nanoprobe technique to the elemental analysis of single as-grown and Co-implanted ZnO nanowires. The nano-X-ray fluorescence technique enabled us not only to examine the spatial variation of Zn and Co elements, but also to disregard the presence of residual impurities in the nanowires, as well as the detection of Fe and Sn residual impurities in the sub-

strates. Our observations provide strong evidence for the overall elemental uniformity of Zn and Co along the wires, without clustering or segregation effects. Within the nanoprobe spatial resolution, our findings indicate a Co localization within thicker irregularities observed with scanning electron microscopy.

© 2011 WILEY-VCH Verlag GmbH & Co. KGaA, Weinheim

1 Introduction The combination of diluted magnetic semiconductors and unidimensional systems has emerged as a promising approach for spintronics nanodevices [1]. In particular, Co doped ZnO nanowires (NWs) offer unique advantages owing to their large geometrical aspect ratio and predicted room-temperature (RT) ferromagnetism [2]. Although there are several reports on Co doped ZnO nanowires [3, 4], besides the issues of magnetism stability [5], it remains controversial whether the incorporation of transition metals (TMs) is as uniform as in bulk crystals or thin films, or with metal clusters and precipitates of impurity phases [4, 6]. In both radial and axial directions, it is still crucial to address electromigration and/or nanosegregation effects, trace element contaminations with magnetic nanoparticles, and mixtures of phases in small domains [7]. However, the role of impurities on NWs and/or on phase separation effects can be only achieved using analytical techniques which are element-specific with high chemical trace sensitivity, and capable of detecting up to nanosized aggregates within deep escape depths. Therefore, the aim of this study is to investigate single Co doped ZnO NWs by hard synchrotron radiation nanoprobe. Although a soft

X-ray nanoprobe is necessary to study the lower-Z elements, a hard X-ray instrument like the nanoimaging station ID22NI of the European Synchrotron Radiation Facility (ESRF) has exceptional attributes for TMs analysis in a higher energy range.

2 Experimental details ZnO NWs were grown on the Si(100) substrates covered with 5 nm thick Au film through the vapour–liquid–solid process at 1350 °C [8, 9]. As-grown ZnO NWs were implanted with Co ions at RT with a total ion fluence of $1.5 \times 10^{16} \text{ cm}^{-2}$ and several ion energies from 60 to 300 keV. This process results in a nominal concentration of 1 at% homogeneously within the NW thickness [3]. After implantation, the samples were annealed at 750 °C for four hours in air to remove the radiation induced lattice damage. The as-grown and Co-implanted ZnO NWs were transferred to clean p-Si (100) substrates via imprint [3]. To examine the elemental uniformity, scanning nano-X-ray fluorescence (XRF) measurements were carried out at the hard X-ray nanoprobe of the beamline ID22 of the ESRF [10]. The station ID22NI is equipped with a pair of Kirkpatrick–Baez multilayer coat-

ed Si mirrors providing a spot of $50 \times 50 \text{ nm}^2$ with a photon flux of about 10^{11} ph/s at 17 keV ($\Delta E/E \approx 10^{-2}$). The XRF signal was detected with an energy dispersive silicon drift detector at 15° related to the sample surface. The XRF spectra were analyzed by the non-linear least-squares fitting code PyMca [11].

3 Results Representative scanning electron micrographs (SEM) of as-grown and Co-implanted NWs are shown in Fig. 1(a) and (b). The wire lengths and average diameters are $15.5 \mu\text{m}$ and 300 nm for the as-grown NW, and $8.5 \mu\text{m}$ and 125 nm for the Co-implanted NW, respectively. Both NWs taper toward the top and show irregularities at the lateral walls due to a secondary vapour–solid process taking place during the growth [12]. Figure 1(c) displays the average XRF spectra collected over the scanned area shown in Fig. 2 for both NWs. The XRF signals, plotted on logarithmic scale, were normalized to the intensity of the Zn K_α peak for clarity. The data exhibit the K_α and K_β fluorescence lines of Zn and Ar generated from the NW and the air, respectively. The escape peaks produced by the Si drift detector at 1.74 keV (Si K_α energy) below the Zn parent lines are also indicated in the graph. In the same energy range, the contribution from the Co K_α line is revealed for the Co-implanted ZnO NW. The measurements show the presence of residual Fe in both samples, and Sn in the Co doped ZnO. The issue if these elements are incorporated into the NW or not, will be addressed later on.

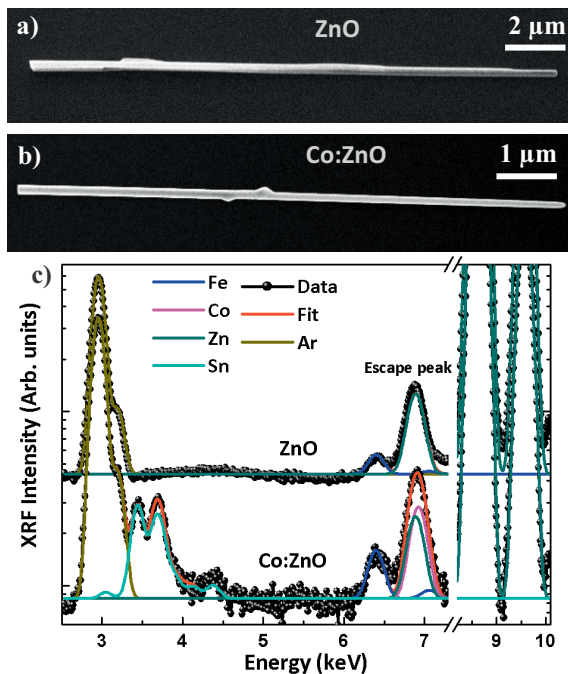


Figure 1 (online colour at: www.pss-rapid.com) SEM images of a single as-grown ZnO NW (a), and a Co implanted ZnO NW (b). Normalized XRF spectra corresponding to both NWs (c). The XRF intensity of the as-grown ZnO NW has been multiplied by five for clarity.

To examine the compositional homogeneity, we have scanned both single NWs taking advantage of the high X-ray flux of ID22NI, typically of the order of 10^{11} ph/s at the focused nanobeam area of $50 \times 50 \text{ nm}^2$. In Fig. 2, red–green–blue plots display the Zn, Co, Fe and Sn XRF intensity distributions for both, as-grown (a) and Co-implanted (b) NWs. The maps were taken with a 25 nm step size and integration time of 500 ms/point. The respective colour scale indicates the intensity range (light represents high counts, dark low counts). As expected, the Zn map exhibits the corresponding bright image for the NW, illustrating the general morphology observed by SEM. On the contrary, the Fe map shows a uniform distribution all-over, indicating that this element is not incorporated into the ZnO NW.

The resulting spatial variations shown in Fig. 2(b) reflect a homogeneous Co-implantation in ZnO, without signatures of impurity-induced defects and/or agglomeration effects in the NW. Within our detection limits, the variations of the fluorescence intensity observed in the Co map are basically due to signal-to-noise statistics rather than changes in the Co content. A preliminary quantification estimates a mean value of $0.15 \pm 0.05 \text{ at}\%$ Co. We have characterized several single Co implanted NWs and found the same elemental homogeneous distribution in all of them. Compared with a previous report on (Ga, Mn)N NWs, which reveals nonuniform elemental patterns [13], our observations show a more homogeneous elemental incorporation at the length scale of the X-ray beam size. Again, the spatial projections of Fe and Sn illustrate a homogeneous distribution all-over, without any preferential

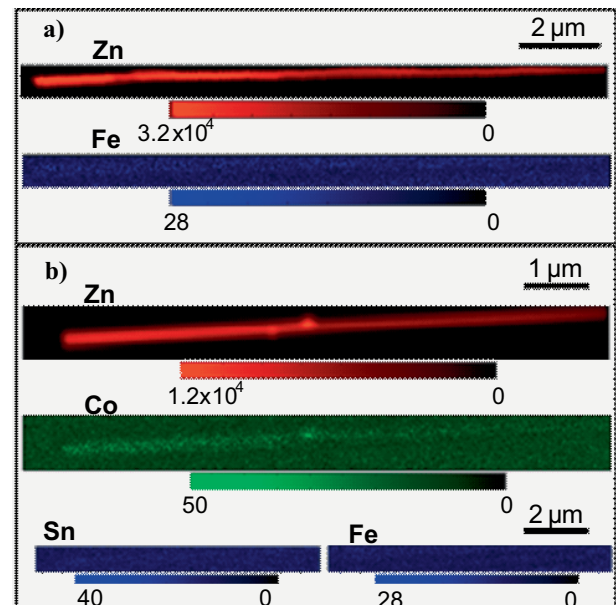


Figure 2 (online colour at: www.pss-rapid.com) Colour maps of the single as-grown ZnO NW (a), and Co implanted ZnO NW (b). Red, green and blue correspond to the Zn, Co, and the Fe and Sn signals, respectively. The intensity ranges are indicated by their colour scale (dark represents low counts, bright high counts).

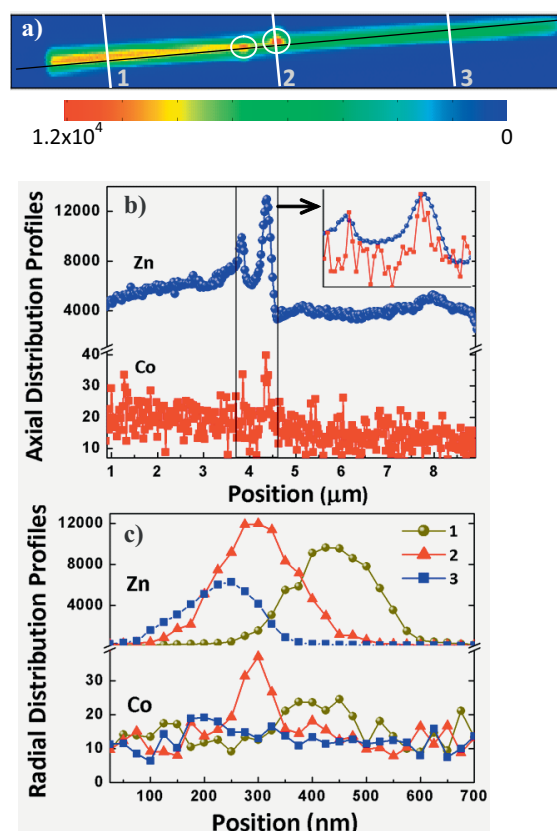


Figure 3 (online colour at: www.pss-rapid.com) Colour map of the integrated XRF count rate of the Co-implanted NW (a). The colour scale indicates the XRF intensity in photon counts. Axial (b) and radial (c) elemental profiles taken as indicated by the lines in (a). The inset in (b) shows the profiles normalized to the intensity of highest Zn peak in the delimited region.

variation along the NW. Within the detection limit of the X-ray nanoprobe, our findings suggest a colocalization of Zn and Co atoms with the presence of background impurities of Fe and Sn in the substrates. The different intensities of Fe and Sn fluorescence lines in the as-grown and implanted samples are not an effect of the implantation process but different residual impurities in two Si substrates used to deposit the NWs.

To gain further insight into the composition of the individual Co doped ZnO NW, Fig. 3 shows the Zn and Co profiles along both radial and axial directions of the NW. The spatial dependences of Zn and Co lines exhibit no relevant contrast along the axial axis in Fig. 3(b), except in the circled regions shown in Fig. 3(a), locally amplified in the inset, where the stronger fluorescence intensity characterized both growth inhomogeneities observed in Fig. 1(b).

Although no clear statement can be made concerning the variation of the composition in the thicker features, from the inset and within the experimental error, the Co signal seems to arise from an inner volume compared to Zn one. The radial uniformity of the Co-implanted ZnO NW was also measured to examine the Co-implantation homo-

geneity. A series of line scans were performed across the wire as indicated by lines 1, 2 and 3 in Fig. 3(a). According to the variation of the wire shape along the axial direction, for the Zn profiles Fig. 3(c) represents the wire diameter. The tapering effect in the NW is evidenced as a reduction in the fluorescence intensity of profile 3 with respect to profile 1. As expected, Zn strength has a larger signal-to-noise ratio than Co. Nevertheless, for the line scan number 2, taken in one of the growth inhomogeneities, a core/shell-like radial distribution is revealed from the Co/Zn profiles, with Co mostly detected in the inner volume of the wire.

In conclusion, we have investigated the elemental distribution of single as-grown and Co-implanted ZnO NWs by hard X-ray nanoprobe. Nano-XRF data have shown no presence of background impurities in the NW but residual Fe and Sn in the substrate. Elemental maps of Zn and Co displayed a homogeneous distribution at the length scale of the X-ray beam size, without clustering or segregation effects. The corresponding profiles along both radial and axial directions of the NW were also examined. Within the experimental accuracy of the X-ray nanoprobe, our findings indicated that Co is homogeneously distributed along the NW, except in thicker irregularities of the wire observed by SEM.

Acknowledgements The authors thank R. Tucoulou and S. Labouré from the ESRF, for the useful help with the set-up of the beamline ID22. This work was partially supported by the NANOWIRING Marie Curie ITN (EU project No. PITN-GA-2010-265073).

References

- [1] T. Dietl, *Nature Mater.* **9**, 965 (2010).
- [2] Y. W. Heo, D. P. Norton, L. C. Tien, Y. Kwon, B. S. Kang, F. Ren, S. J. Pearton, and J. R. LaRoche, *Mater. Sci. Eng. R* **47**, 1 (2004).
- [3] C. Ronning, C. Borschel, S. Geburt, and R. Niepelt, *Mater. Sci. Eng. R* **70**, 30 (2010).
- [4] A. Nadarajah and R. Konenkamp, *Phys. Status Solidi B* **248**, 334 (2011).
- [5] E. A. Choi, W. J. Lee, and K. J. Chang, *J. Appl. Phys.* **108**, 023904 (2010).
- [6] L. Q. Liu, B. Xiang, X. Z. Zhang, Y. Zhang, and D. P. Yu, *Appl. Phys. Lett.* **88**, 063104 (2006).
- [7] S. Deka and P. A. Joy, *Solid State Commun.* **142**, 190 (2007).
- [8] M. H. Huang, Y. Wu, H. Feick, N. Tran, E. Weber, and P. Yang, *Adv. Mater.* **13**, 113 (2001).
- [9] C. Borchers, S. Müller, D. Stichtenoth, D. Schwen, and C. Ronning, *J. Phys. Chem. B* **110**, 1656 (2006).
- [10] R. Tucoulou, G. Martinez-Criado, P. Bleuett, I. Kieffer, P. Cloetens, S. Labouré, T. Martin, C. Guilloud, and J. Susini, *J. Synchrotron Radiat.* **105**, 392 (2008).
- [11] V. A. Sole, E. Papillon, M. Cotte, Ph. Walter, and J. Susini, *Spectrochim. Acta B* **62**, 63 (2007).
- [12] Z. L. Wang, *J. Phys.: Condens. Matter* **16**, R829 (2004).
- [13] A. Urban, J. Malindretos, M. Seibt, and A. Rizzi, *Nano Lett.* **11**, 398 (2011).

4

Nano-X-ray absorption spectroscopy of single Co-implanted ZnO nanowires

J. Segura-Ruiz, G. Martínez-Criado, M. H. Chu, S. Geburt, and C. Ronning

Nano-X-ray Absorption Spectroscopy of Single Co-Implanted ZnO Nanowires

J. Segura-Ruiz,^{*,†} G. Martínez-Criado,[†] M. H. Chu,[†] S. Geburt,[‡] and C. Ronning[‡]

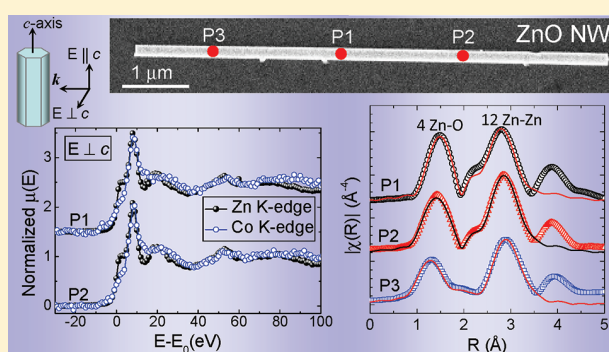
[†]European Synchrotron Radiation Facility, Experiments Division, 38043 Grenoble, France

[‡]Institute of Solid State Physics, University of Jena, D-07743 Jena, Germany

S Supporting Information

ABSTRACT: We report on the local structure of single Co-implanted ZnO nanowires studied using a hard X-ray nanoprobe. X-ray fluorescence maps show uniform Zn and Co distributions along the wire within the length scale of the beam size. The X-ray fluorescence data allow the estimation of the Co content within the nanowire. Polarization dependent X-ray absorption near edge structure shows no structural disorder induced neither in the radial nor axial directions of the implanted nanowires after subsequent annealing. Co²⁺ ions occupy Zn sites into the wurtzite ZnO lattice. Extended X-ray absorption fine structure data reveal high structural order in the host lattice without distortion in their interatomic distances, confirming the recovery of the radiation damaged ZnO structure through thermal annealing.

KEYWORDS: EXAFS, XANES, nanowires, ZnO, dilute magnetic semiconductors



Determining the local order of individual nanostructures is crucial to understand their behavior in the spintronics nanodevices.^{1–3} In particular, Co-doped ZnO nanowires (NWs) offer unique advantages owing to their large geometrical aspect ratio and predicted room-temperature ferromagnetism.^{4,5} In addition to spintronic applications, transitions involving degenerated Co 3d-shell states within the ZnO could be used in optoelectronic devices.⁶ However, controlled doping of semiconductor NWs with transition metals (TM) during growth remains a challenge. For instance, the doping of NWs by metal–organic chemical vapor deposition,⁷ molecular beam epitaxy,⁸ or hot-walled pulsed laser deposition,⁹ gives origin to a high density of structural defects (e.g., edge dislocations and stacking faults), inhomogeneous dopant distribution and secondary phases. Ion implantation is an alternative that allows a better control of both concentration and distribution of TM ions.¹⁰ Determining the doping homogeneity and local order of individual implanted nanostructures is crucial to understand their behavior in spintronics nanodevices. Although there are many reports about ensembles of NWs, it remains controversial whether the incorporation of Co in individual NWs is substitutional as in bulk crystals or thin films, without the formation of metallic clusters or precipitates.^{11,12} The average local atomic structure and secondary phases in ensembles of NWs have already been studied by X-ray absorption near edge structure (XANES) and extended X-ray absorption fine structure (EXAFS).^{13,14} However, the examination of single NWs remains an experimental challenge. Alternatively, the long-range order in single nanostructures has been analyzed by X-ray nanodiffraction,¹⁵

three-dimensional strain images of single NWs have been obtained by coherent X-ray diffraction imaging,¹⁶ and the 3D structure of nanoscale crystals by X-ray Fourier transform holography.¹⁷ Moreover, we have recently reported the application of synchrotron fluorescence nanoimaging to single NWs,^{18,19} but the X-ray absorption acquisitions have been mostly limited by the beam instability during the energy scan and chromaticity of the nanofocusing lens. In this work, a Kirkpatrick–Baez mirror based nanoprobe with scanning X-ray fluorescence (XRF) capability was used to explore phase separation effects and short-range order in single Co implanted ZnO NWs. In addition, the linear polarization of the synchrotron nanobeam made our study not only element specific but also capable of detecting preferentially oriented defects induced by the ion implantation process.²⁰

In this Letter, we describe the investigation of ZnO NWs grown on p-Si (100) substrates using vapor–liquid–solid process. The main NW axis is parallel to the *c*-axis of the wurtzite structure. The Co ions were implanted using a dose of $1.57 \times 10^{16} \text{ cm}^{-2}$ with ion energies ranging from 60 to 300 keV to obtain a homogeneous concentration profile. After the Co implantation, the NWs were annealed at 750 °C in air during four hours to recover from the radiation induced lattice damage. More details about growth and implantation processes can be found elsewhere.^{6,21} For the X-ray based analysis, the

Received: August 12, 2011

Revised: October 2, 2011

Published: October 18, 2011

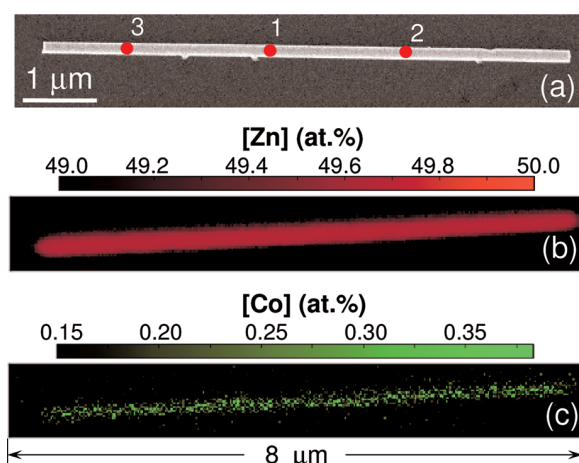


Figure 1. (a) SEM image of the single Co implanted NW. Elemental maps collected at 12 keV for Zn (b) and Co (c) with the respective atomic fraction estimated from the XRF quantification.

NWs were transferred to a clean p-Si (100) substrate via imprint. The X-ray absorption measurements were carried out at the hard X-ray nanoprobe beamline ID22 of the European Synchrotron Radiation Facility.²² The monochromatic X-ray beam was focused to $100 \times 100 \text{ nm}^2$ spot size with $\sim 10^{11}$ ph/s using a pair of Kirkpatrick–Baez Si mirrors. The intensity of the incident beam was monitored with a gas filled ionization chamber. The XRF signal was collected at 15° with respect to the substrate surface with a Si drift detector. The XRF maps were taken at 12 keV with a pixel size of $25 \times 25 \text{ nm}^2$ and an accumulation time of 500 ms per pixel. The information depths of Co and Zn fluorescence photons were about 8.0 and 4.3 μm at 12 keV, respectively.²³ Using the PyMca program,²⁴ the XRF spectra were fitted to quantify the elemental composition. XANES and EXAFS data were recorded in XRF mode with a step size of 1 eV and integration times determined by the counting statistics. The data analysis was performed using the IFEFFIT package.²⁵

Figure 1a shows the scanning electron microscopy (SEM) image of a single NW with diameter and length of 180 nm and 7 μm , respectively. The positions indicated by 1, 2, and 3 correspond to the areas where XANES and EXAFS spectra were recorded. Figure 1b,c shows the elemental maps of Zn and Co with the respective concentrations estimated from the XRF quantification.²⁶ The average concentrations of Co and Zn are (0.3 ± 0.1) and (49.7 ± 0.1) atom %, respectively. These values are in good agreement with those obtained from simulations using the IRADINA Monte Carlo code,²⁷ which takes the nanowire geometry fully into account. Within our detection limits, the observed content variations are due to signal-to-noise statistics rather than changes in the Co and Zn fractions. The maps indicate homogeneous distributions of Co and Zn along the NW without any signature of clusters or nanoaggregates.

Taking advantage of the high spatial resolution and the linear polarization of the X-ray beam, Zn K edge XANES spectra recorded along the NW are shown in Figure 2a. The *c*-axis of the NW is oriented perpendicular to the electric field vector of the synchrotron radiation. Due to the scalar product between the photon polarization vector (*e*) and the position vector of the photon (*r*) in the matrix element of the absorption cross section: $M = \langle \phi_{1s} | \mathbf{e} \cdot \mathbf{r} | \phi_j \rangle$, XANES spectra in wurtzite ZnO depend on

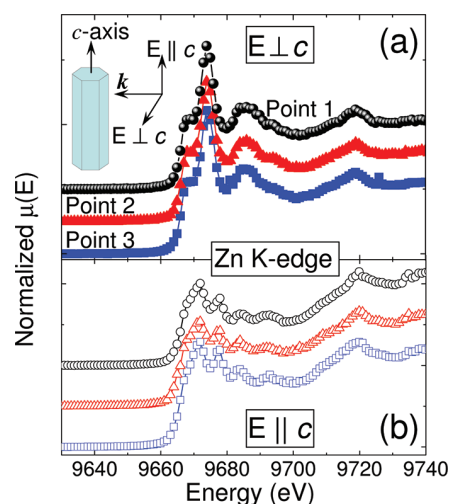


Figure 2. Zn K edge XANES spectra recorded along the NW with the *c*-axis oriented perpendicular (a), and parallel (b) to the electric field vector of the X-ray nanobeam. For clarity, the spectra were shifted vertically.

the crystallographic orientation.²⁸ Thus, if the electric field of the absorbed photons is perpendicular to the *c*-axis ($E \perp c$), transitions from $1s$ to p_{xy} states are allowed. Therefore, under our experimental configuration, the XANES data probe the symmetry of the *ab*-plane, namely p_{xy} conduction band states. The spectral features in Figure 2a reflect the typical wurtzite structure of the ZnO lattice.²⁹ No signatures of Zn metallic precipitates after the ion implantation process are observed in the spectra. According to the line shapes and peaks energies, there is no structural disorder in the radial direction along the implanted NW. For the axial direction, Figure 2b displays the XANES data from the NW with its *c*-axis oriented parallel to the electric field vector of the X-ray beam. Thus, the XANES data probe the symmetry of the *c*-plane, namely p_z conduction band states. Again, the spectra exhibit the peaks associated to the hexagonal structure, without any evidence of lattice damage along the NW. Our findings reveal the high structural order of the host lattice along both radial and axial directions.

Figure 3a shows the XANES spectra around the Zn K edge (solid circles) and Co K edge (open circles) at points 1 and 2. To enable the comparison between Zn and Co XANES spectra, the energy has been rescaled to the respective absorption K edges calculated from the first derivative of the XANES signal. Despite the low Co content, the quality of the XANES data around the Co K edge reproduces well the oscillations of the Zn K edge spectra at both points, with minor differences above 70 eV. Co ions seem to be incorporated into the wurtzite host lattice on the Zn sites. To gain further insight into the Co chemical configuration, Figure 3b shows the average XANES spectrum of the NW around the Co K edge (solid circles). For comparison, we have included the Co K edge XANES of a high quality wurtzite $\text{Zn}_{0.9}\text{Co}_{0.1}\text{O}$ epitaxial film taken from ref 29 (open circles), a mixed valence Co_3O_4 sample (open triangles), and a metallic Co foil (open squares). The good match between the NW and ZnCoO data suggests oxidation state 2+ for Co ions. Metallic Co and/or mixed valence Co_3O_4 contributions are not clearly visible. The weak pre-edge peak around 7710 eV arises from the hybridization of the Co 3d and 4p orbitals states induced by the tetrahedral crystal field within the

noncentrosymmetric ZnO structure.^{14,30} While a strong pre-edge peak is associated with the existence of pure CoO particles as a secondary phase,¹⁴ our result supports that Co has been substitutionally incorporated into the wurtzite ZnO lattice.

In order to confirm the local structure, EXAFS data around the Zn K edge were acquired at different positions along the NW. Figure 4a plots the k^3 -weight EXAFS oscillations accompanied by their best fits in the interval $[0-8.1 \text{ \AA}^{-1}]$ using a Hanning window. The data analysis was carried out by ab initio modeling of the absorption cross section using the FEFF code.³¹ Theoretical backscattering amplitudes and phase shifts for all single and multiple scattering paths were calculated using hexagonal ZnO model clusters ($a = 3.289 \text{ \AA}$ and $c = 5.315 \text{ \AA}$).³² The ARTEMIS routine²⁵ was exploited to fit the data in R space within the window $[1.0-3.7 \text{ \AA}]$, which included the first and second coordination shells. On the basis of previous X-ray diffraction data,³³ a fixed coordination of 4 O nearest neighbor atoms and 12 Zn second-nearest-neighbor atoms was applied. We have fitted the interatomic distances (R_i) and Debye–Waller (DW) factors (σ_i^2) of the various atomic shells, fixing the amplitude $s_0^2 = 0.7307$ as determined from the metallic Zn foil. The values of the structural parameters extracted from the curve fits are reported in Table 1.

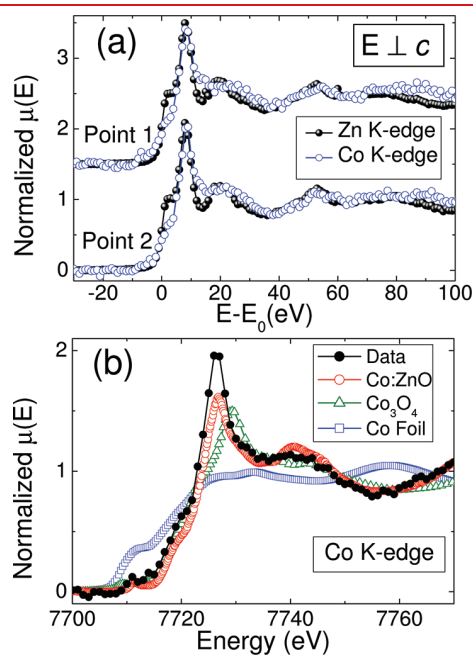


Figure 3. (a) XANES spectra around the Zn K edge (solid circles) and Co K edge (open circles) taken at points 1 and 2. The energy has been rescaled to the respective absorption K edges. (b) Average XANES spectrum of the NW around the Co K edge (solid circles), a high quality wurtzite $\text{Zn}_{0.9}\text{Co}_{0.1}\text{O}$ epitaxial film taken from ref 29 (open circles), a mixed valence Co_3O_4 sample (open triangles), and a metallic Co foil (open squares).

Table 1. Summary of the Interatomic Distances (R_i), Debye–Waller (DW) Factors (σ_i^2) of the Various Atomic Shells, and the R -Factors Obtained from the Fittings of the FT EXAFS Fixing $s_0^2 = 0.7307$ As Determined from the Metallic Zn Foil

point	$R_{\text{Zn-O}}$ (Å)	$\sigma_{\text{Zn-O}}^2 \times 10^{-3} (\text{Å}^2)$	$R_{\text{Zn-Zn}}$ (Å)	$\sigma_{\text{Zn-Zn}}^2 \times 10^{-3} (\text{Å}^2)$	R
1	1.97 ± 0.02	2.3 ± 1.6	3.25 ± 0.02	5.0 ± 1.4	0.016
2	1.98 ± 0.02	3.7 ± 1.6	3.25 ± 0.01	4.5 ± 1.3	0.011
3	1.98 ± 0.02	9.3 ± 2.0	3.25 ± 0.01	7.4 ± 1.5	0.011

Figure 4b shows the corresponding magnitude of the Fourier transforms (FTs) of the EXAFS functions. The spectra show two dominant peaks related to the first O- and second Zn-shells, which are expected in the wurtzite model. All points show the same contributions with a slight decrease in the first shell amplitude as a function of the position. In general, within the experimental accuracy, there is no change in the first and second neighbor distances along the NW. Note that the Zn–O and Zn–Zn spacings are equal to those of pure ZnO (1.98 and 3.25 \AA ³⁴), without any evidence of amorphization. The undistorted cation–anion first neighbor distance also reflects the low Co content estimated by XRF in the implanted ZnO NW (Figure 1). For points 2 and 3, the apparent reduced amplitude of the nearest O-neighbor peak is accounted for by the higher static disorder; namely, increase of their corresponding DW factors. The data analysis suggests that there is no local atomic distortion around the Zn sites, although there is an increase in the width of the interatomic distance distribution, as measured by the EXAFS DW factor. The overall EXAFS results do not indicate any significant contribution from common defects generated by the implantation process, e.g., secondary phases, vacancy accumulations and interstitials. This confirms

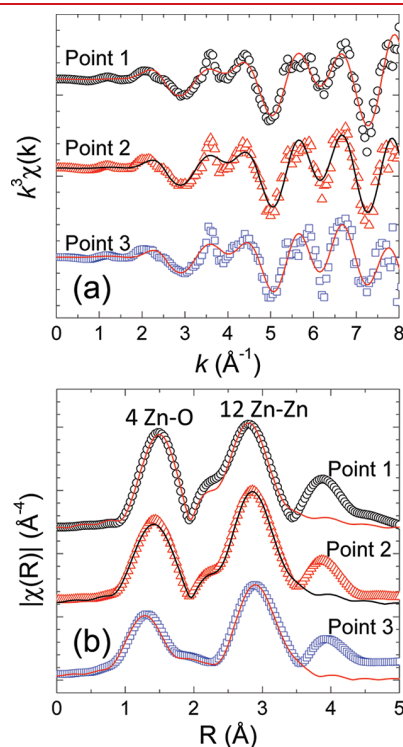


Figure 4. (a) k^3 -weight EXAFS oscillations (open symbols) accompanied by their best fits (solid lines) in the interval $k = 0-8.1 \text{ \AA}^{-1}$. (b) Magnitude of the FTs of the EXAFS functions (open symbols) and their best fits (solid lines). For clarity, the spectra were shifted vertically.

the good recovery of the radiation damaged ZnO lattice through the thermal annealing.

The overall EXAFS results obtained in these NWs are in agreement with what we have observed in 4 atom % Co implanted ZnO NW by transmission electron microscope (TEM).⁶ There, secondary phases in the NWs after annealing were not observed, although the structural damage created by the ion implantation process was not completely removed by annealing. However, to further corroborate our findings, new TEM images were acquired in several 1 atom % Co implanted NWs. In Supplementary Figures S1 and S2 in Supporting Information we show midmagnification and high-resolution TEM images of single NWs, along with their electron diffraction patterns and the fast Fourier transform (FFT) of selected areas. The high-resolution TEM images show a perfect recovered ZnO lattice without any evidence of extended defects or secondary phases. Furthermore, the FFT images exhibit sharp spots, which are signatures of a nearly perfect wurtzite single crystal after the annealing. The spacing between the (0002)-planes determined from the TEM images is around 0.52 nm, which is in good agreement with the values obtained from the fittings of our EXAFS results. In some NWs, a very low density of stacking faults and dislocations remaining after the annealing were observed. This fact could explain the higher static disorder observed by EXAFS in some points of the NW. Therefore, the overall TEM results fully support the recovery of the radiation damaged ZnO lattice through the thermal annealing evidenced in our EXAFS results.

In summary, we have studied the local structure of single Co implanted ZnO NWs using a hard X-ray nanoprobe. Elemental maps showed Zn and Co ions homogeneously distributed along the NW. From the XRF spectra an estimation of the Co content in the wire was reported, with an average $[Co] = (0.3 \pm 0.1)$ atom %. Polarization dependent XANES showed that there was no structural disorder induced neither in the radial nor axial directions of the implanted NWs. XANES around the Co K edge displayed the substitutional incorporation of Co^{2+} ions into the Zn sites of the wurtzite host lattice. EXAFS data analysis supported the tetrahedral configuration of Zn in the hexagonal host lattice without pronounced distortion in the interatomic distances of the two nearest neighbor shells. Our EXAFS results gave no evidence of large structural defects induced in the ZnO host lattice by the Co incorporation and confirm the annealing mediated recovery of the ZnO structure. Although the presence of defects cannot be completely ruled out, within the sensitivity of our experimental techniques neither secondary phases or oxygen vacancies were observed. Our findings are fully supported by the TEM analysis of implanted single NWs.

■ ASSOCIATED CONTENT

S Supporting Information. Figures showing midmagnification and high-resolution TEM images of Co implanted ZnO NWs, along with their electron diffraction pattern and the fast Fourier transform (FFT) of selected areas. This material is available free of charge via the Internet at <http://pubs.acs.org>.

■ AUTHOR INFORMATION

Corresponding Author

*E-mail: seguraru@esrf.fr.

■ ACKNOWLEDGMENT

The authors thank Steffen Milz and Irina Snigireva for their help with the TEM and SEM measurements, respectively. We thank Remi Tocoulou and Peter Cloetens for their help and the ESRF for the beam time allocated. We also thank Claudia Schnohr for the valuable discussions and Gary Admans for the critical reading of the manuscript. This work has been partially supported by the NANOWIRING Marie Curie ITN (EU project no. PITN-GA-2010-265073).

■ REFERENCES

- (1) Tulapurkar, A. A.; Suzuki, Y.; Fukushima, A.; Kubota, H.; Maehara, H.; Tsunekawa, K.; Djayaprawira, D. D.; Watanabe, N.; Yuasa, S. *Nature* **2005**, *438*, 339–342.
- (2) Sankey, J. C.; Braganca, P. M.; Garcia, A. G. F.; Krivorotov, I. N.; Buhman, R. A.; Ralph, D. C. *Phys. Rev. Lett.* **2006**, *96*, 227601.
- (3) Mourachkine, A.; Yazyev, O. V.; Ducati, C.; Ansermet, J.-P. *Nano Lett.* **2008**, *8*, 3683–3687.
- (4) Heo, Y. W.; Norton, D.; Tien, L.; Kwon, Y.; Kang, B.; Ren, F.; Pearton, S.; LaRoche, J. *Mater. Sci. Eng., R* **2004**, *47*, 1–47.
- (5) Cui, J. B.; Gibson, U. J. *Appl. Phys. Lett.* **2005**, *87*, 133108.
- (6) Müller, S.; Zhou, M.; Li, Q.; Ronning, C. *Nanotechnology* **2009**, *20*, 135704.
- (7) Chen, C.-H.; Chang, S.-J.; Chang, S.-P.; Li, M.-J.; Chen, I.-C.; Hsueh, T.-J.; Hsu, A.-D.; Hsu, C.-L. *J. Phys. Chem. C* **2010**, *114*, 12422–12426.
- (8) Urban, A.; Malindretos, J.; Seibt, M.; Rizzi, A. *Nano Lett.* **2011**, *11*, 398–401.
- (9) Song, Y.-W.; Kim, K.; Ahn, J. P.; Jang, G.-E.; Lee, S. Y. *Nanotechnology* **2009**, *20*, 275606.
- (10) Chen, I.-J.; Ou, Y.-C.; Wu, Z.-Y.; Chen, F.-R.; Kai, J.-J.; Lin, J.-J.; Jian, W.-B. *J. Phys. Chem. C* **2008**, *112*, 9168–9171.
- (11) Cui, J.; Gibson, U. *Phys. Rev. B* **2006**, *74*, 045416.
- (12) Liao, L.; Li, J. C.; Wang, D. F.; Liu, C.; Peng, M. Z.; Zhou, J. M. *Nanotechnology* **2006**, *17*, 830.
- (13) Yuhua, B. D.; Fakra, S.; Marcus, M. A.; Yang, P. *Nano Lett.* **2007**, *7*, 905–909.
- (14) Busgen, T.; Hilgendorff, M.; Irsen, S.; Wilhelm, F.; Rogalev, A.; Goll, D.; Giersig, M. *J. Phys. Chem. C* **2008**, *112*, 2412–2417.
- (15) Hrauda, N.; Zhang, J.; Wintersberger, E.; Etzelstorfer, T.; Mandl, B.; Stangl, J.; Carbone, D.; Holý, V.; Jovanović, V.; Biasotto, C.; Nanver, L. K.; Moers, J.; Grützmacher, D.; Bauer, G. *Nano Lett.* **2011**, *11*, 2875–2880.
- (16) Xiong, G.; Huang, X.; Leake, S.; Newton, M. C.; Harder, R.; Robinson, I. *New J. Phys.* **2011**, *13*, 033006.
- (17) Chamard, V.; Stangl, J.; Carbone, G.; Diaz, A.; Chen, G.; Alfonso, C.; Mocuta, C.; Metzger, T. H. *Phys. Rev. Lett.* **2010**, *104*, 165501.
- (18) Segura-Ruiz, J.; Martínez-Criado, G.; Sans, J. A.; Tucoulou, R.; Cloetens, P.; Snigireva, I.; Denker, C.; Malindretos, J.; Rizzi, A.; Gomez-Gomez, M.; Garro, N.; Cantarero, A. *Phys. Status Solidi RRL* **2011**, *9*, 95–97.
- (19) Chu, M. H.; Segura-Ruiz, J.; Martínez-Criado, G.; Cloetens, P.; Snigireva, I.; Geburt, S.; Ronning, C. *Phys. Status Solidi RRL* **2011**, *283*–285.
- (20) Jian, W. B.; Wu, Z. Y.; Huang, R. T.; Chen, F. R.; Kai, J. J.; Wu, C. Y.; Chiang, S. J.; Lan, M. D.; Lin, J. J. *Phys. Rev. B* **2006**, *73*, 233308.
- (21) Ronning, C.; Borschel, C.; Geburt, S.; Niepelt, R. *Mater. Sci. Eng., R* **2010**, *70*, 30–43 (3rd IEEE International NanoElectronics Conference (INEC)).
- (22) Tucoulou, R.; Martínez-Criado, G.; Bleuet, P.; Kieffer, I.; Cloetens, P.; Labouré, S.; Martin, T.; Guilloud, C.; Susini, J. *J. Synchrotron Radiat.* **2008**, *15*, 392–398.
- (23) Tröger, L.; Arvanitis, D.; Baberschke, K.; Michaelis, H.; Grimm, U.; Zschech, E. *Phys. Rev. B* **1992**, *46*, 3283–3289.

- (24) Solé, V.; Papillon, E.; Cotte, M.; Walter, P.; Susini, J. *Spectrochim. Acta, Part B* **2007**, *62*, 63–68.
- (25) Newville, M. J. *Synchrotron Radiat.* **2001**, *8*, 322–324.
- (26) Somogyi, A.; Martínez-Criado, G.; Homs, A.; Hernandez-Fenollosa, M. A.; Vantelon, D.; Ambacher, O. *Appl. Phys. Lett.* **2007**, *90*, 181129.
- (27) Borschel, C.; Ronning, C. *Nucl. Instrum. Methods Phys. Res., Sect. B* **2011**, *269*, 2133–2138.
- (28) Stöhr, J. *NEXAFS Spectroscopy*; Springer: Berlin, 1992.
- (29) Ney, A.; Ollefs, K.; Ye, S.; Kammermeier, T.; Ney, V.; Kaspar, T. C.; Chambers, S. A.; Wilhelm, F.; Rogalev, A. *Phys. Rev. Lett.* **2008**, *100*, 157201.
- (30) Martínez-Criado, G.; Segura, A.; Sans, J. A.; Homs, A.; Pellicer-Porres, J.; Susini, J. *Appl. Phys. Lett.* **2006**, *89*, 061906.
- (31) Ankudinov, A. L.; Ravel, B.; Rehr, J. J.; Conradson, S. D. *Phys. Rev. B* **1998**, *58*, 7565–7576.
- (32) Cicero, G.; Ferretti, A.; Catellani, A. *Phys. Rev. B* **2009**, *80*, 201304.
- (33) Geurts, J.; Schumm, M.; Koerdel, M.; Ziereis, C.; Müller, S.; Ronning, C.; Dynowska, E.; Gołacki, Z.; Szuszkiewicz, W. *Phys. Status Solidi B* **2010**, *247*, 1469–1471.
- (34) Decremps, F.; Datchi, F.; Saitta, A. M.; Polian, A.; Pascarelli, S.; Di Cicco, A.; Itié, J. P.; Baudelet, F. *Phys. Rev. B* **2003**, *68*, 10410.

■ NOTE ADDED AFTER ASAP PUBLICATION

This paper was published on the Web on October 26, 2011. The word "irradiation" has been changed to "radiation" in four places. The correct version was published on November 7, 2011.

Supplementary information

Nano-X-ray Absorption Spectroscopy of Single Co Implanted ZnO Nanowires

J. Segura-Ruiz,[†] G. Martínez-Criado,[†] M. H. Chu,[†] S. Geburt,[‡] and C. Ronning[‡]

[†] *European Synchrotron Radiation Facility, 38043 Grenoble, France*

[‡] *Institute of Solid State Physics, University of Jena, D-07743 Jena, Germany*

In order to corroborate our nano-EXAFS findings, transmission electron microscope (TEM) images were acquired in several Co implanted NWs. Figure S1(a) shows a mid-magnification image of one of the implanted ZnO NWs analysed. The roughened surface observed in the NWs, which gives origin to the irregular contrast of the image towards the core of the NW, is most likely due to ion beam induced surface modification. Figure S1(b) shows the high-resolution TEM image of the same NW, where a perfect recovered ZnO lattice without any evidence of extended defects or secondary phases is observed. The fast Fourier transformed image of Figure S1(b) is shown in Figure S1(c). The sharp spots obtained are a signature of a nearly perfect wurtzite single crystal after the annealing. The spacing between the (0002)-planes determined from the TEM images is around 0.52 nm, in good agreement with the values obtained from the fittings of our nano-EXAFS results.

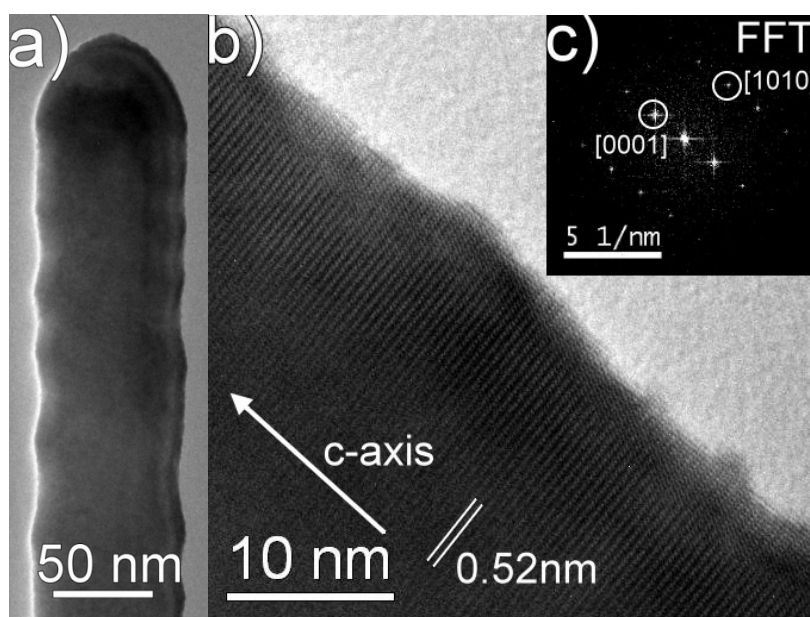


Figure S1. (a) Mid-magnification TEM image of a 75 nm-thick Co implanted ZnO NW. (b) High-resolution TEM image of the same NW shown in (a) and fast Fourier transform of a selected area (c).

In some NWs, a very low density of stacking faults and dislocations remaining after the annealing are observed. For instance, in the inverse fast Fourier transform image of a second NW shown in Figure S2(d), two arrows indicates this kind of defects.

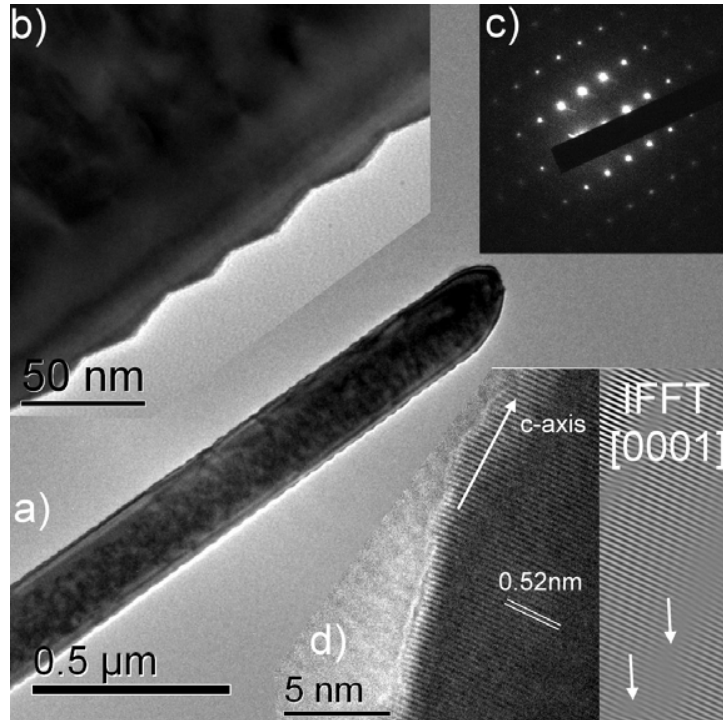


Figure S2. Low (a) and mid-magnification (b) TEM images of a 190 nm-thick Co implanted ZnO NW, and its corresponding electron diffraction pattern (c). (d) High-resolution TEM image along with the inverse fast Fourier transform of a selected area.

5

Local lattice distortions in single Co-implanted ZnO nanowires

M. H. Chu, G. Martínez-Criado, J. Segura-Ruiz, S. Geburt, and C. Ronning

Local lattice distortions in single Co-implanted ZnO nanowires

M. H. Chu,^{1,a)} G. Martínez-Criado,^{1,a)} J. Segura-Ruiz,¹ S. Geburt,² and C. Ronning²

¹Experiments Division, European Synchrotron Radiation Facility, 38043 Grenoble, France

²Institute of Solid State Physics, University of Jena, D-07743 Jena, Germany

(Received 16 July 2013; accepted 19 September 2013; published online 2 October 2013)

This work reports on the local structure of as-implanted and thermally-treated single Co:ZnO nanowires studied using a hard X-ray nanoprobe. Although the Co ions are incorporated into the wurtzite ZnO lattice, X-ray absorption near edge structure data show high structural disorder in the as-implanted nanowires compared with the annealed ones. In particular, extended X-ray absorption fine structure from single wires reveals a lattice distortion around Zn sites of the as-implanted nanowires, which involves an expansion of the stable wurtzite lattice. The observed local lattice response confirms good recovery of the implantation-induced damage within the ZnO lattice through a thermal treatment. © 2013 AIP Publishing LLC. [<http://dx.doi.org/10.1063/1.4824117>]

Cobalt (Co) implanted ZnO nanowires (NWs) are one of the most promising wide band gap semiconductors for spintronics and optoelectronics nanodevices.^{1,2} Beside the interesting magnetic properties, such as predicted room-temperature ferromagnetism, Co-implanted ZnO NWs also offer promising optical properties by sharp-intra 3d emission in ZnO.^{2,3} The combination of the magnetic with optical properties would enhance the functionality of nanodevices.⁴ So far, ion implantation process has proven to be an effective and easy way to incorporate Co into the ZnO host lattice; but it generally produces unwanted structural defects in the NWs.⁵ Although nonlocal and averaged data collected over large ensembles of implanted NWs using conventional diffraction methods have revealed a crystal lattice distortion induced by the ion implantation process,^{6–9} its direct observation from individual NWs has only been addressed recently by grazing incidence X-ray diffraction using an X-ray beam of $300 \times 500 \text{ nm}^2$.¹⁰ Owing to the use of a smaller hard X-ray nanobeam ($110 \times 110 \text{ nm}^2$), we show the resulting local crystallographic order spatially resolved in single Co implanted ZnO NWs. In order to achieve more detailed insight into the unavoidable local lattice distortions generated purely by the ion implantation process, our approach exploited different X-ray absorption based analytical techniques. Owing to the high brilliance of a synchrotron radiation nanoprobe, our measurements present exceptional attributes: element-specificity, polarization selectivity, and chemical traces sensitivity at the nanometer length scale.

In the present work, we have studied a set of ZnO NWs grown on *p*-Si (100) substrates via vapor-liquid-solid growth.¹¹ The as-grown NW samples, which possessed a spaghetti-type morphology, were implanted with Co ions at room temperature. A total ion fluence of $1.57 \times 10^{16} \text{ cm}^{-2}$ and ion energies ranging from 60 to 300 keV were used in order to obtain nominal concentration in the range of 0.35–0.85 at. %, as calculated using the *iradina* code.¹² The concentration variations are due to the sample morphology, as the angle between the ion beam and nanowires was not defined. For comparison, after Co implantation some NWs

undergo a thermal annealing at 750°C in air for 4 h. More details about the growth and ion implantation can be found elsewhere.^{5,11}

Since NW ensembles with a fully randomly “spaghetti” fashion were produced by vapor-liquid-solid growth, to allow the analysis of single nanostructures, the NWs were transferred on a clean Si substrate via imprint⁵ that simplified the localization of single NWs by scanning electron microscopy (SEM) prior to the synchrotron measurements. Then, dispersed NWs (selected formerly by SEM) were examined using the hard X-ray nanoprobe. The X-ray fluorescence (XRF) and X-ray absorption spectroscopy measurements were carried out at the beamline ID22 of the European Synchrotron Radiation Facility (ESRF).¹³ The end-station ID22NI was equipped with a pair of Kirkpatrick-Baez Si multilayer mirrors, providing a spot size of $110 \times 110 \text{ nm}^2$ with a photon flux of 10^{10} ph/s at 12 keV, allowing the efficient investigation of single nanowires. The XRF signal was detected using a Si drift detector placed at 15° with respect to substrate surface. The XRF spectra were fitted to quantify the elemental composition using PyMca code.¹⁴ X-ray absorption near edge structure (XANES) and extended X-ray absorption fine structure (EXAFS) data were acquired in XRF mode with a step size of 1 eV and integration times determined by the counting statistics. The data analysis was performed using the IFEFFIT package.¹⁵

Figures 1(a) and 1(b) show the SEM images of representative annealed and as-implanted Co:ZnO NWs. The wire lengths and average diameters were about $7 \mu\text{m}$ and 200 nm , respectively. It is well known that the NWs can morphologically be curved under ion beam irradiation¹⁶ if an unbalance of induced defects between different regions in the nanowires is formed. After thermal annealing, this unbalance of defects is reduced, resulting in a more straight shape. Figure 1(c) displays the average XRF spectra collected on both NWs. Apart from the Zn and Co signals, and Ar from the air, the peaks associated with Ca and Fe are only observed on the spectrum from the annealed NW. But, XRF elemental maps [not shown here] show that these two residual elements are not originating from the NW, as they are detected all over the substrate.¹⁷ The escape peak produced by the Si drift detector at 1.74 keV below Zn parent lines is also

^{a)}Authors to whom correspondence should be addressed. Electronic addresses: mchu@esrf.fr and gmartine@esrf.fr

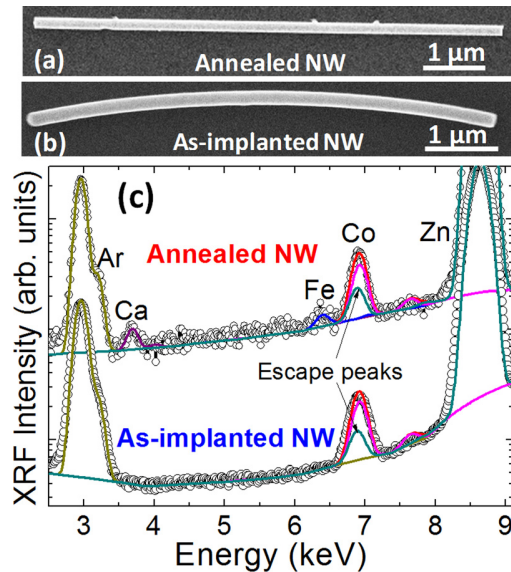


FIG. 1. SEM images of (a) annealed and (b) as-implanted Co:ZnO nanowires and (c) XRF spectra corresponding to both NWs. The XRF intensity of the as-implanted NW has been divided by one hundred for clarity.

indicated. Although XRF shows no difference between both NWs, the resulting fit performed on the different X-ray characteristic lines (which included the escape peaks) is also displayed. The XRF quantification yields average concentrations of Co for the annealed and as-implanted NWs of about (0.33 ± 0.04) and (0.37 ± 0.03) at. %, respectively. The Co contents are in good agreement with those values obtained from the simulations using the *iradina* program, which is a Monte Carlo and TRIM-based code taking the 3D structure of the nanowire into account.¹² The similarity of both Co estimations implies that Co is not diffused out from the NW during the thermal annealing process.

Figure 2(a) displays the XANES spectra around the Zn K-edge (solid circles) and Co K-edge (open circles) for both annealed and as-implanted NWs. For comparison, the energy has been rescaled to the respective absorption K-edges. Despite the low Co content, the XANES spectra around the Co K-edges show the same features and oscillations as the Zn K-edge for both cases, strongly indicating the incorporation of Co on Zn sites in the wurtzite host lattice.¹⁸ Although addressed later, it is worth to highlight already here the superior intensity of the Co K-edge white line (WL) peak for the annealed NW. Further insight into the Co chemical configuration can be also provided by comparison with the XANES spectrum of a high quality $\text{Zn}_{0.9}\text{Co}_{0.1}\text{O}$ epitaxial film taken from Ref. 19 [the graph is not shown here] as well as with a Co foil and Co_3O_4 standard [not shown here either]. The good match between XANES data of both NWs and $\text{Zn}_{0.9}\text{Co}_{0.1}\text{O}$ film corroborates an oxidation state of 2+ for Co ions in the NWs.

In order to obtain a detailed picture of the as-implanted situation and annealing, the Co K-edge spectra were fitted by a step function, which represents the electronic transition from the Co 1s states to the continuum, and four Gaussians designated by Roman numerals I to IV as shown in Fig. 2(b), which simulate electronic transition to final bound states with a *p* component. The fitting results are listed in Table I. While the

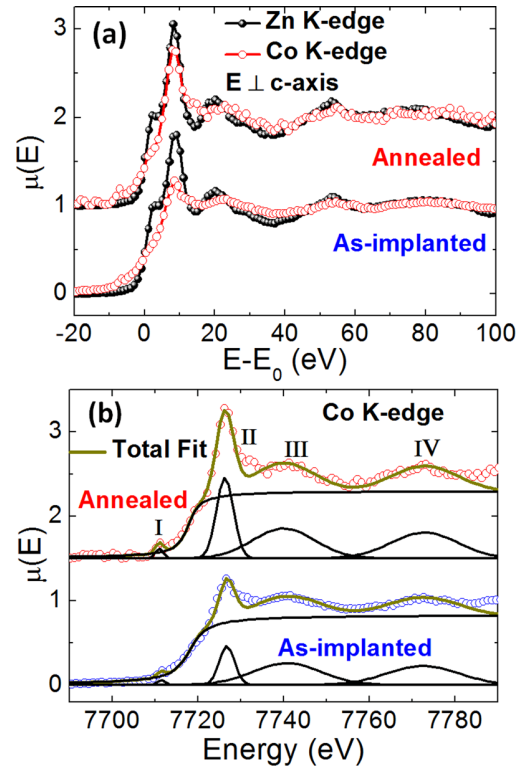


FIG. 2. Superposition of XANES spectra around the Zn K-edge (solid black circles) and Co K-edge (open red circles) for annealed and as-implanted NWs. The energy has been rescaled to the respective absorption K-edges. (b) XANES fitting of Co K edge spectra for both NWs. The spectra were fitted by a step function and four Gaussians I to IV to simulate transitions to final *p*-states. The spectra of the annealed NW were vertically shifted for clarity in both figures.

peak energy positions and full width at half maximums (FWHMs) are identical within the experimental errors for both NWs, the peak amplitudes for the annealed NW are higher than the ones for the as-implanted NW. The tiny but measurable pre-edge peaks (I) are due to the electronic transitions from 1s states to unfilled 3*d*-like states, which can occur without inversion symmetry.^{20,21} Thus, their amplitudes are proportional to the hybridization between 3*d*-Co and 2*p*-O orbitals. Therefore, our observations can be linked to the thermal annealing in air. During the treatment, either interstitial oxygen atoms or oxygen vacancies can be diffused within the crystal structure, and in any case result into annihilation of the defects. As a consequence, more 2*p*-O orbitals are available in the annealed NW for the hybridization with 3*d*-Co orbitals than in the as-implanted NW, resulting in a more pronounced pre-edge peak. The peaks labeled II, III, and IV are due to the electronic transitions from 1s states to unoccupied final 4*p* states. All three peaks also exhibit higher intensities in the annealed case than in the as-implanted one. These findings can be attributed to the lattice damage around Co atoms in the as-implanted NW, which prevents electronic transitions to the unfilled 4*p* states. Typically, a number of implantation-induced defects, such as vacancies and interstitials, are reduced through the thermal annealing process, leading to a higher degree of structural order.

However, according to Table I, the WL intensity (peak II) increases much more than peaks III and IV for the annealed NW than for the as-implanted one. This observation can be

TABLE I. Summary of the peak positions, FWHMs and intensities of the four transition peaks obtained from the multi-Gaussian fits applied to Co K-edge XANES spectra of both NWs.

Peaks	As-implanted NW			Annealed NW		
	Position (eV)	FWHM (eV)	Height (a.u.)	Position (eV)	FWHM (eV)	Height (a.u.)
I	7711	1	0.1	7711	1	0.2
II	7727	2	0.9	7727	2	1.9
III	7740	9	0.5	7740	9	0.7
IV	7773	10	0.4	7773	9	0.6

attributed to multiple factors. Apart from the reduction of the static crystal disorder that improves the line height, this effect could be also associated with a more intense hybridization between $2p$ -O and $3d$ -Co in the annealed NW compared with the as-implanted one.²² But, the increase of the pre-edge peak (indicator of p - d hybridization) is quite small compared with the observed increase in the WL intensity. Another possible explanation would be a larger surface-to-bulk ratio effect, namely, the presence of surface sites (e.g., oxygen terminated surfaces). However, a recent calculation found that the observed increase of the WL peak intensity for ZnO NWs cannot be associated with the surface, because the main XANES peak intensities corresponding to atoms at the surfaces are smaller than those of bulk ZnO.²³ Finally, it should be mentioned that a polarization related effect, where the XANES signals present a strong orientation dependence, might be also

the origin.^{18,24} Summarizing, crystal disorder strongly influence the amplitude of the main peak.

In order to gain a better understanding of the local structure of both situations, as-implanted and after annealing, EXAFS spectra were collected at the Zn K-edge for the single nanowires. Figure 3(a) shows the EXAFS $k^3\chi(k)$ spectra around Zn K-edge of the annealed and as-implanted Co:ZnO NWs and their best fits in the interval $[0-8.1 \text{ \AA}^{-1}]$. The k^3 -weighted EXAFS spectra were Fourier transformed with a Hanning window to real (R) space. The EXAFS spectra were modeled theoretically using FEFF8 code using the program ARTEMIS.²⁵ The model assumed a wurtzite ZnO cluster with lattice parameters $a = 3.2498 \text{ \AA}$ and $c = 5.2066 \text{ \AA}$.²⁶ The EXAFS fitting was restricted to the first two coordination shells in the R-range from 1.0 \AA to 3.7 \AA . The amplitude $S_0^2 = 0.7307$ was used as determined from measurement of a metallic Zn foil as well as the coordination number around the Zn absorbing atom of 4 O nearest neighbor and 12 Zn second nearest neighbor atoms were fixed. The fitting results are summarized in Table II.

Figure 3(b) displays the corresponding magnitude of the Fourier transforms (FTs) of Zn K-edge EXAFS functions for both annealed and as-implanted NWs. The first and second peaks correspond to the 4 oxygen and 12 zinc atoms, respectively. The spectra show similar contributions but with slight differences. While the first shell amplitude is similar for both NWs. There is a decrease in the second shell amplitude for the as-implanted NW compared with the annealed one. The lower amplitude of the second neighbor peaks for the as-implanted NW is accounted for by the higher static disorder; namely, increase of the respective DW factor as shown in Table II. The fitting results reveal a detectable change in the first and second neighbor distances between the as-implanted and annealed NWs. As expected for the annealed NW, the interatomic lengths of the first and second shells are equal to those of pure ZnO within the error bars (1.95 ± 0.02 and $3.23 \pm 0.02 \text{ \AA}$),²⁷ suggesting no local atomic distortion

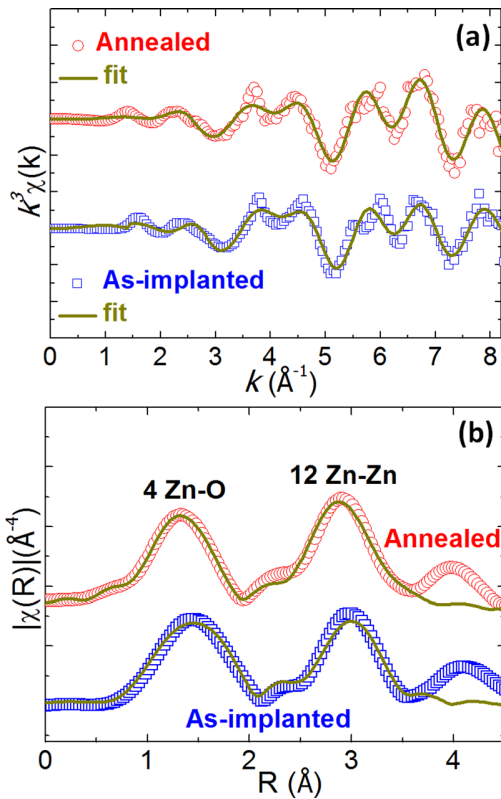


FIG. 3. (a) Zn K-edge EXAFS oscillation functions $k^3\chi(k)$ of the annealed NW (circle symbols) and the as-implanted NW (square symbols) accompanied with their best fits (solid lines). (b) Magnitude of the Fourier-transformed Zn K-edge EXAFS functions for both NWs (open symbols) and their best fits (solid lines). The spectrum of annealed NW was shifted vertically for clarity.

TABLE II. Summary of the interatomic distances (R_i), Debye-Waller (DW) factors (σ_i^2), and R-factors obtained from the fittings of FT Zn K-edge EXAFS.

Co:ZnO NWs	As-implanted	Annealed
$R_{\text{Zn-O}} (\text{\AA})$	1.99 ± 0.01	1.96 ± 0.01
$\sigma_{\text{Zn-O}}^2 \times 10^{-3} (\text{\AA})$	1.3 ± 1.0	1.4 ± 1.0
$R_{\text{Zn-Zn}} (\text{\AA})$	3.26 ± 0.02	3.22 ± 0.01
$\sigma_{\text{Zn-Zn}}^2 \times 10^{-3} (\text{\AA})$	8.9 ± 1.7	5.0 ± 1.3
R	0.008	0.004

around the Zn sites. Once more, our data analysis supports the good recovery of the implantation-induced damage of the ZnO host lattice through the post-implantation thermal annealing process.¹⁸ For the as-implanted NW, our results directly reveal a lattice expansion through the increase of Zn-O and Zn-Zn lengths compared with the corresponding interatomic distances for the pure ZnO. This local lattice distortion around Zn sites also affects the WL peak intensity of the XANES spectrum around Zn K-edge (see above). An EXAFS study of ion implanted GaN layers, which is a similar material system to ZnO, reported also elongations around the Ga atoms for the first and second shells (about 0.01 Å).²⁸ Complementary methods, like X-ray diffraction, applied to either implanted ZnO or GaN films have also exhibited a lattice expansion by implantation induced defects.^{29–32} Interatomic lengths deduced from a representative diffractogram of Ca-implanted GaN film pointed out an increase of around 0.01 and 0.02 Å for the first and second shells, respectively.³⁰ In those cases, the lattice expansion was caused by the incorporation of larger ionic radius atoms into the host lattice and/or by the formation of defects during the implantation process.^{28–32} In our case, however, we can exclude the former effect because the ionic radius of Co²⁺ (~0.56 Å) is smaller than that of Zn²⁺ (~0.60 Å).³³ Therefore, the resulting lattice expansion must be attributed to structural defects, such as vacancies and interstitials, generated during the ion implantation. Our results highlight the crucial role played by the severe stoichiometric imbalance in the detailed local structure of single NWs.

In conclusion, we have studied the local structural disorder induced by the ion implantation process in single cobalt doped ZnO NWs using a hard X-ray nanoprobe. An estimation of the average Co content was deduced through XRF acquisitions. XANES analyses revealed that the incorporation of Co²⁺ ions into the wurtzite ZnO lattice is accompanied by a higher structural disorder. This observation is further supported by EXAFS results around the Zn K-edge, which once more showed a fully crystal structure recovery by the thermal annealing. Most important, the EXAFS data analysis showed not only a significant increase in the Debye-Waller factor, but also a local lattice expansion induced by the ion implantation process. Our findings provided direct evidence of the structural atomic distortions present in single NWs at the nanoscale, which could affect the performance of advanced optoelectronics and spintronics nanodevices.

The authors thank R. Tucoulou and S. Labouré for their help with the experimental setup and I. Snigireva for the SEM measurements. This work has been partially supported by the NANOWIRING Marie Curie ITN EU project (No. PITN-GA-2010-265073) and the DFG research unit FOR1616.

- ¹T. Dietl, *Nature Mater.* **9**, 965 (2010).
- ²S. Müller, M. Zhou, Q. Li, and C. Ronning, *Nanotechnology* **20**, 135704 (2009).
- ³Y. W. Heo, D. Norton, L. Tien, Y. Kwon, B. Kang, F. Ren, S. Pearton, and J. Laroche, *Mater. Sci. Eng., R* **47**, 1 (2004).
- ⁴W. Liang, B. D. Yuhas, and P. Yang, *Nano Lett.* **9**, 892 (2009).
- ⁵C. Ronning, C. Borschel, S. Geburt, and R. Niepelt, *Mater. Sci. Eng., R* **70**, 30 (2010).
- ⁶S. H. Park, S. H. Kim, and S. W. Han, *J. Korean Phys. Soc.* **50**, 1557 (2007).
- ⁷J. Wang, M. J. Zhou, S. K. Hark, Q. Li, D. Tang, M. W. Chu, and C. H. Chen, *Appl. Phys. Lett.* **89**, 221917 (2006).
- ⁸Y. Shen, J. I. Hong, Z. Peng, H. Fang, S. Zhang, S. Dong, R. L. Snyder, and Z. L. Wang, *J. Phys. Chem. C* **114**, 21277 (2010).
- ⁹Y. B. Lee, C. H. Kwak, S. Y. Seo, S. H. Kim, C. I. Park, B. H. Kim, S. H. Park, Y. D. Choi, and S. W. Han, *J. Korean Phys. Soc.* **56**, 2050 (2010).
- ¹⁰G. Bussone, R. Schott, A. Biermanns, A. Davydok, D. Reuter, G. Carbone, T. U. Schüllli, A. D. Wieck, and U. Pietsch, *J. Appl. Crystallogr.* **46**, 887 (2013).
- ¹¹C. Borchers, S. Muller, D. Stichtenoth, D. Schwen, and C. Ronning, *J. Phys. Chem. B* **110**, 1656 (2006).
- ¹²C. Borschel and C. Ronning, *Nucl. Instrum. Methods Phys. Res. B* **269**, 2133 (2011).
- ¹³G. Martínez-Criado, R. Tucoulou, P. Cloetens, P. Bleuet, S. Bohic, J. Cauzid, I. Kieffer, E. Kosior, S. Laboure, S. Petitgirard, A. Rack, J. Angel Sans, J. Segura-Ruiz, H. Suhonen, J. Susini, and J. Villanova, *J. Synchrotron Radiat.* **19**, 10 (2012).
- ¹⁴V. A. Solé, E. Papillon, M. Cotte, Ph. Walter, and J. Susini, *Spectrochim. Acta, Part B* **62**, 63 (2007).
- ¹⁵B. Ravel and M. Newville, *J. Synchrotron Radiat.* **12**, 537 (2005).
- ¹⁶C. Borschel, R. Niepelt, S. Geburt, C. Gutsche, I. Regolin, W. Probst, F. J. Tegude, D. Stichtenoth, D. Schwen, and C. Ronning, *Small* **5**, 2576 (2009).
- ¹⁷M. H. Chu, J. Segura-Ruiz, G. Martínez-Criado, P. Cloetens, I. Snigireva, S. Geburt, and C. Ronning, *Phys. Status Solidi (RRL)* **5**, 283 (2011).
- ¹⁸J. Segura-Ruiz, G. Martínez-Criado, M. H. Chu, S. Geburt, and C. Ronning, *Nano Lett.* **11**, 5322 (2011).
- ¹⁹A. Ney, K. Ollefs, S. Ye, T. Kammermeier, V. Ney, T. C. Kaspar, S. A. Chambers, F. Wilhelm, and A. Rogalev, *Phys. Rev. Lett.* **100**, 157201 (2008).
- ²⁰C. Song, K. W. Geng, F. Zeng, X. B. Wang, Y. X. Shen, F. Pan, Y. N. Xie, T. Liu, H. T. Zhou, and Z. Fan, *Phys. Rev. B* **73**, 024405 (2006).
- ²¹Z. L. Lu, H. S. Hsu, Y. H. Tzeng, F. M. Zhang, Y. W. Du, and J. C. A. Huang, *Appl. Phys. Lett.* **95**, 102501 (2009).
- ²²T. Mizoguchi, I. Tanaka, S. Yoshioka, M. Kunitsu, T. Yamamoto, and W. Y. Ching, *Phys. Rev. B* **70**, 045103 (2004).
- ²³O. Šipr and F. Rocca, *J. Phys.: Condens. Matter* **23**, 315501 (2011).
- ²⁴T. Kuykendall, P. J. Pauzauskie, Y. Zhang, J. Goldberger, D. Sirbully, J. Denlinger, and P. Yang, *Nature Mater.* **3**, 524 (2004).
- ²⁵M. Newville, *J. Synchrotron Radiat.* **8**, 96 (2001).
- ²⁶A. Zeuner, H. Alves, D. M. Hofmann, B. K. Meyer, M. Heuken, J. Blasing, and A. Kros, *Appl. Phys. Lett.* **80**, 2078 (2002).
- ²⁷J. Haug, A. Chassé, M. Dubiel, Ch. Eischenschmidt, M. Khalid, and P. Esquinazi, *J. Appl. Phys.* **110**, 063507 (2011).
- ²⁸M. Katsikini, F. Pinakidou, E. C. Paloura, F. Boscherini, E. Wendler, and W. Wesch, *Mater. Sci. Eng., B* **152**, 132 (2008).
- ²⁹S. Zhou, Q. Xu, K. Potzger, G. Talut, R. Grötzschel, J. Fassbender, M. Vinnichenko, J. Grenzer, M. Helm, H. Hochmuth, M. Lorenz, M. Grundmann, and H. Schmidt, *Appl. Phys. Lett.* **93**, 232507 (2008).
- ³⁰C. Liu, B. Mensching, M. Zeitler, K. Volz, and B. Rauschenbach, *Phys. Rev. B* **57**, 2530 (1998).
- ³¹C. Liu, B. Mensching, K. Volz, and B. Rauschenbach, *Appl. Phys. Lett.* **71**, 2313 (1997).
- ³²M. Mamor, V. Matias, A. Vantomme, A. Colder, P. Marie, and P. Ruterana, *Appl. Phys. Lett.* **85**, 2244 (2004).
- ³³B. D. Yuhas, S. Fakra, M. A. Marcus, and P. Yang, *Nano Lett.* **7**, 905 (2007).

5. LOCAL LATTICE DISTORTIONS IN SINGLE CO-IMPLANTED ZNO NANOWIRES

6

Structural order in single Co-implanted ZnO nanowires

M. H. Chu, G. Martínez-Criado, J. Segura-Ruiz, S. Geburt, and C. Ronning

Structural order in single Co-implanted ZnO nanowires

M. H. Chu^{*1}, G. Martínez-Criado^{**1}, J. Segura-Ruiz¹, S. Geburt², and C. Ronning²

¹ Experiments Division, European Synchrotron Radiation Facility, 38043 Grenoble, France

² Institute of Solid State Physics, University of Jena, 07743 Jena, Germany

Received 29 June 2013, revised 28 August 2013, accepted 20 December 2013

Published online 3 February 2014

Keywords co-implanted ZnO, nanowires, XANES, XRD

* Corresponding author: e-mail mchu@esrf.fr, Phone: +33 476 882 916, Fax: +33 476 882 785

** e-mail gmartine@esrf.fr, Phone/Fax: +33 476 882 931

In this work, we report on the short and long range order of single room temperature-implanted and high temperature-implanted Co:ZnO nanowires using hard X-ray nanoprobe-based techniques. X-ray fluorescence maps reveal a homogeneous distribution of the Co ions implanted along the nanowires. X-ray absorption near edge structure data indicate a substitutional incorporation of Co²⁺ into the wurtzite ZnO host lattice. The room temperature-implanted nanowires

present a higher structural disorder around Co atoms compared to the high temperature-implanted ones. X-ray diffraction results show a crystal lattice expansion induced by the ion implantation process in the room temperature-implanted nanowires. Micro-photoluminescence data corroborate these findings and exhibit an excellent optical activation of the incorporated Co ions in the high temperature-implanted nanowires.

© 2014 WILEY-VCH Verlag GmbH & Co. KGaA, Weinheim

1 Introduction Much effort has been devoted to the investigation of dilute magnetic semiconductors in recent years due to their potential applications in spintronics nanodevices [1, 2]. In particular, Co-doped ZnO nanowires (NWs) offer unique advantages owing to the large aspect ratio and theoretically predicted room temperature ferromagnetism [3]. Cobalt is known to be optically active in semiconductors through the Co 3d intra-shell transition [4], thus Co-doped ZnO NWs could also provide promising optical properties for future optoelectronic nanodevices [5]. However, doping of NWs with transition metals during growth remains a challenge [6]. Due to the self-organized growth mechanisms, the NWs are sensitive to changes in the growth conditions. Up to date, ion implantation process has proven to be an effective way for doping with Co in a controlled manner ZnO NWs [7, 8]. However, the implanted sample has to be thermally treated to recover from the ion implantation-induced defects and to make the implanted ions optically active [9]. Despite previous studies [10], a structural picture of the symmetry of single Co-implanted ZnO at nanometer levels remains incomplete. Some open questions concern the existence of secondary phases in the thermally annealed NWs implanted with Co at high temperature; whether the ion implantation-induced damage

causes a short and/or long-range orientational disorder; and whether the implantation temperature produces relevant atomic distortions. In this work, these questions are addressed using four different techniques: nano-X-ray fluorescence (XRF), X-ray absorption near edge structure (XANES), X-ray diffraction (XRD), and micro-photoluminescence (μ PL).

2 Experimental details In this work, we have studied single ZnO NWs grown on p-Si(100) substrates using vapor–liquid–solid process. The as-grown ZnO NWs which are randomly orientated with respect to the Si substrate surface, were implanted with Co ions at room and high (700 °C) temperature with a dose of $1.57 \times 10^{16} \text{ cm}^{-2}$ and an angle of the incidence of 45° off the substrate surface normal. The ion energies ranged from 60 to 300 keV in order to obtain a homogeneous nominal concentration in the range of 0.30–0.85 at.%, as calculated by the *iradina* Monte Carlo code [11]. The concentration variations are due to the different angle between incident ion beam and nanowires. After Co implantation, the nanowire sample with high temperature (HT) implantation was thermally annealed at 750 °C in air for 4 h. More details about sample growth and implantation processes can be found elsewhere [8, 12]. For

the X-ray analysis, the room temperature (RT)-implanted and HT-implanted NWs were dispersed on either clean p-Si(100) substrates or 200 nm thick SiN membranes. The morphology of the single NWs was examined *ex situ* using a Zeiss Leo 1530 scanning electron microscopy (SEM) operated at 20 kV. The hard X-ray nanoprobe based measurements were carried out at the nanoimaging station ID22NI of the European Synchrotron Radiation Facility (ESRF) [13]. XRF measurements were performed using a 17 keV pink beam ($\Delta E/E \approx 10^{-2}$) with a total flux $\sim 10^{12}$ photons per second focused down using a pair of Kirkpatrick–Baez multilayer coated Si mirrors. The vertical and horizontal beam profiles are shown in Fig. 1a. From the Gaussian fitting, a beam size of $83 \times 86 \text{ nm}^2$ ($V \times H$) was obtained. The detection limits of the system were also estimated as shown in Fig. 1b by measuring the XRF of a NIST reference material 1577b (Bovine Liver) at 17 keV. The XRF signal was detected using a Si drift detector placed at 15° with respect to substrate surface. The XRF maps were taken with a pixel size of $25 \times 25 \text{ nm}^2$ and an accumulation time of 0.5 s per pixel. To quantify the elemental composition, the XRF spectra were fitted using the PyMca software [14]. XANES and XRD measurements were performed using a monochromatic beam ($\Delta E/E \approx 10^{-4}$), with a spot size of around $110 \times 110 \text{ nm}^2$ and a total flux of $\sim 10^{10}$ photons per second. XANES spectra were recorded in XRF mode with a step size of 1 eV and integration times determined by the counting statistics. The XRD signal was measured using a fast readout low noise (FReLoN) CCD detector [15]. The XANES and XRD data were analyzed using the IFEFFIT and the Fit2D packages, respectively [16–18]. Micro-photoluminescence (μPL) measurements of single NWs were carried out at low temperature (4 K) using a self-built epifluorescence microscope with excitation by a continuous wave 325 nm HeCd laser [19].

3 Results Figure 2a shows the average XRF spectra of the RT-implanted and HT-implanted Co:ZnO NWs. The data exhibit the $K\alpha$ and $K\beta$ fluorescence lines of Zn and Co generated from both NWs and Ar from the air. The escape peaks produced by the Si drift detector at 1.74 (Si $K\alpha$ energy) below Zn parent lines are indicated in the graph.

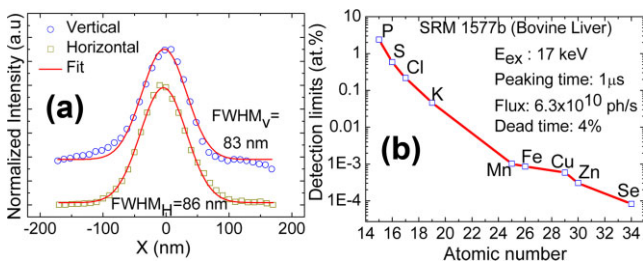


Figure 1 (a) Vertical and horizontal beam size evaluation using Au knife edge pattern. The vertical spectrum was shifted vertically for clarity. (b) Detection limits of the XRF measurements calculated using the signal from the NIST reference material 1577b (Bovine Liver) at 17 keV.

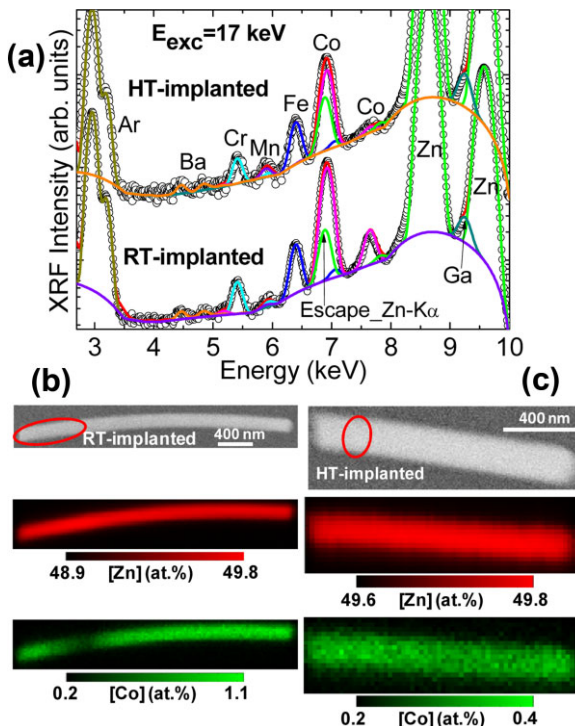


Figure 2 (a) XRF spectra of the RT-implanted and HT-implanted Co:ZnO NWs. The XRF intensity of HT-implanted NW has been multiplied by a factor of 50 for clarity. (b) and (c) SEM images of both RT-implanted and HT-implanted NWs, respectively, as well as the associated maps of Zn and Co for each NW. The atomic fraction of Zn and Co elements are shown respectively in each elemental map. The red circles indicate the positions where nano-XRD patterns were acquired.

The measurements also show the presence of residual Cr, Mn, Fe, Ga, and Ba elements in both spectra. Upper parts of Fig. 2b and c display the SEM images of the representative RT-implanted and HT-implanted Co:ZnO NWs, respectively. The wire length and diameter are $3.1 \mu\text{m}$ and 160 nm for the RT-implanted NW, and $1.4 \mu\text{m}$ and 210 nm for the HT-implanted NW, respectively. The RT-implanted NW is morphologically bent under ion beam irradiation due to the formation of an unbalance of defects between different regions in the NWs [20]. The unbalance of defects is reduced through thermal treatment, resulting in more straight shape for the HT-implanted NW.

To examine the compositional homogeneity in the NWs, the XRF spectrum of each pixel was fitted to build the elemental distribution maps shown in Fig. 2b and c. Both Zn and Co maps with the respective concentrations show a homogeneous distribution along the RT-implanted and HT-implanted NWs. From the Co map of the RT-implanted NW, the appearance of a small dark region on the left of the NW is neither a segregation nor inhomogeneous incorporation of Co, but nanowire overlapping-induced shading effects during the Co implantation process. Fluorescence maps of the residual Cr, Mn, Fe, Ga, and Ba (not shown here) reveal a uniform distribution in all the scanned area, without any

preferential variation along the NWs. Within our detection limits, our findings confirm that these elements are not incorporated into the NWs. They most likely come from contamination of the substrates where the NWs are dispersed. The XRF quantification yields average concentrations of Co for the RT-implanted and HT-implanted NWs of about (0.8 ± 0.3) and (0.3 ± 0.1) at%. The Co contents are in good agreement with those values obtained from simulation using the *iradina* Monte Carlo code [11]. The different concentrations of both NWs are due to the different angle of the ion beam with respect to the NW's main axis, rather than the out-diffusion of Co during the annealing process.

Figure 3a displays the XANES spectra around Zn and Co K-edges for the RT-implanted and HT-implanted Co:

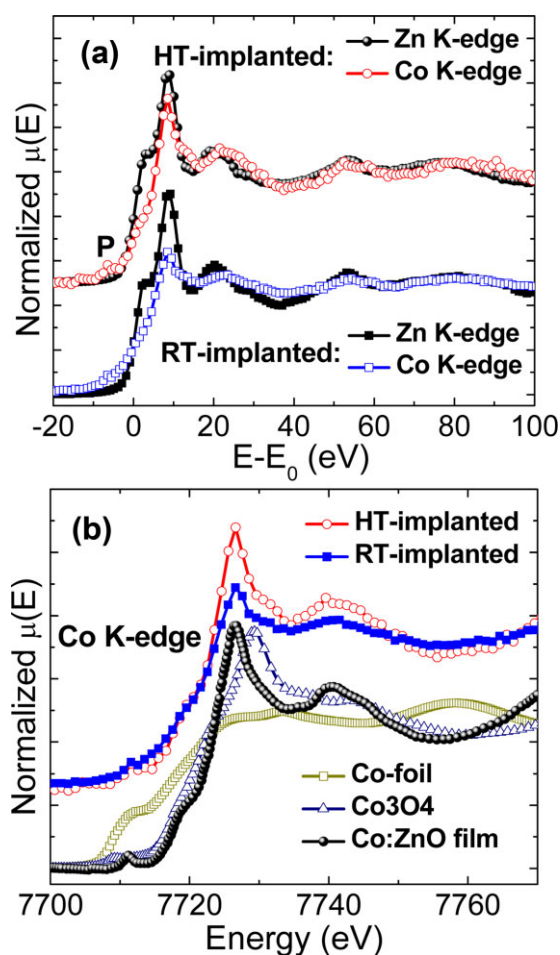


Figure 3 (a) XANES spectra around Zn and Co K-edges for the RT-implanted (square symbols) and HT-implanted (circle symbols) Co:ZnO NWs. The energy has been rescaled to respective absorption K-edges. XANES spectra of the HT-implanted NW were shifted vertically for clarity. (b) XANES spectra around Co K-edge for both RT-implanted (solid squares) and HT-implanted (open circles) NWs, a high quality wurtzite $\text{Zn}_{0.9}\text{Co}_{0.1}\text{O}$ film (solid circles), a mixed valence Co_3O_4 (open triangles), and a metallic Co foil (open squares). The spectra of the RT and HT-implanted NWs were vertically shifted for clarity.

ZnO NWs. For comparison, the energy has been rescaled to respective absorption K-edges calculated from the first derivative of the XANES spectra. The XANES spectra correspond to electronic transitions from 1s states to unoccupied final 4p states, except for the weak pre-edge peak [labeled by P in the graph] of the Co K-edge spectra, which corresponds to electronic transitions from 1s states to unfilled 3d-like states [21]. The XANES spectra around Co K-edge shows similar features and oscillation compared to Zn K-edge for both NWs. This result points toward the incorporation of Co in the wurtzite ZnO host lattice on Zn sites [10]. Co K-edge XANES spectrum of the HT-implanted NW shows higher peak intensities than the RT-implanted one. This can be due to the implantation-induced lattice damage around Co atoms in the RT-implanted NW, which prevents the electronic transitions to the unoccupied 4p states. In the case of the HT-implanted one, the number of implantation-induced defects is reduced either by post-thermal treatment or during the HT-implantation. As a result, there is a higher crystal order degree for the HT-implanted NW than for the RT-implanted one. This observation is in good agreement with the one obtained in thermally annealed NWs implanted with Co ions at room temperature reported in a previous work [10].

Further insight into the Co chemical configuration is obtained from the comparison of the Co K-edge XANES spectra of both NWs with some reference samples having different oxidation states. Figure 3b shows the comparison between the Co K-edge XANES spectra of the RT-implanted (solid squares) and HT-implanted (open circles) NWs, with those from a high quality wurtzite $\text{Zn}_{0.9}\text{Co}_{0.1}\text{O}$ epitaxial film (solid circles) [22], a mixed valence Co_3O_4 (open triangles), and a metallic Co foil (open squares). The best match for both NWs is found with the spectrum of the $\text{Zn}_{0.9}\text{Co}_{0.1}\text{O}$ film, indicating a Co oxidation state of 2+.

Figure 4a illustrates a representative XRD peak from the left part of the RT-implanted Co:ZnO NW (marked on SEM image of Fig. 2b). The signal is dominated by a peak labeled A and a shoulder (peak B), whose positions were fitted by two Gaussian contributions. In comparison with the reported lattice parameters for wurtzite ZnO ($a = 3.2498 \text{ \AA}$ and $c = 5.2066 \text{ \AA}$) [23], the peak A at 9.84° is assigned to the ZnO (0002) reflection. The peak B at 9.67° is due to structural modifications induced by the ion implantation. In principle, it would also indicate a ZnO lattice expansion along the c -axis. An expansion of the c -lattice parameter of around 0.09 \AA could be estimated from the difference in 2θ between both peaks A and B, however, further measurements are necessary to confirm our observation. So far, similar lattice expansions have been reported for implanted ZnO and GaN films [24, 25]. The expansion of host lattice is attributed to the structural defects, such as vacancies and interstitials generated by the ion implantation process [24, 25]. On the other hand, Fig. 4b shows a representative XRD reflection obtained from the left part of the HT-implanted Co:ZnO NW (marked on SEM image of Fig. 2c). This reflection can be fitted using a single Gaussian

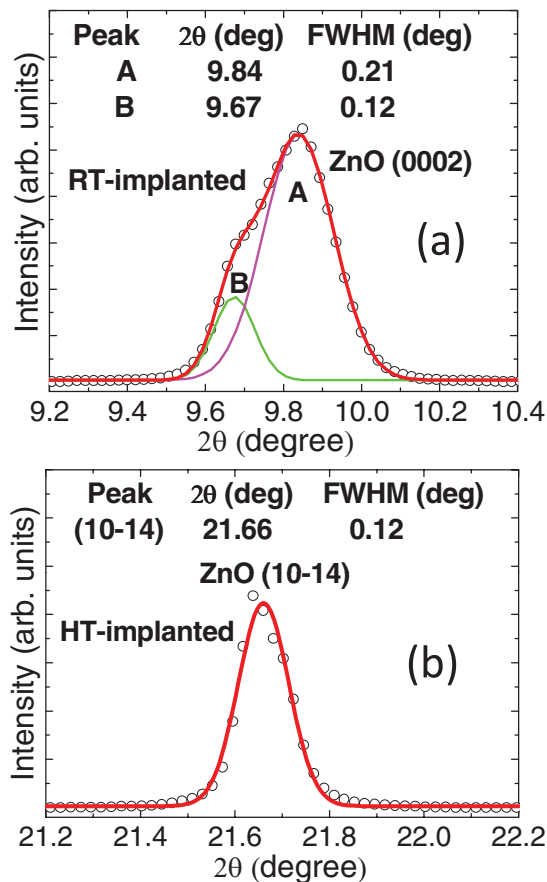


Figure 4 (a) (0002) and (b) (10–14) XRD peaks along with their best Gaussian fits for the RT-implanted and HT-implanted Co:ZnO NWs, respectively. The peak position and FWHM obtained from the fitting are indicated for each peak.

contribution and its maximum corresponds to the wurtzite ZnO (10–14) reflection. Likewise, its position would suggest that the ion implantation-induced lattice expansion is well recovered through either post-implantation thermal annealing or dynamic annealing during the implantation process. In addition to the peak position, the full width at half maximum (FWHM) of the XRD peak for the HT-implanted NW is smaller than that of the main peak of the RT-implanted NW. It confirms a better crystal structure for the HT-implanted NW compares with the RT-implanted one. XRD data on single ZnO NW implanted with Co at RT and followed by the thermal annealing (annealed NW), were also acquired to support these findings. A representative XRD peak of the annealed NW [not shown here] reveals only ZnO (0002) reflection at 9.79° with FWHM of 0.18° without any expanded peak from the main ZnO (0002). This is another signature of the good recovery of the ion implantation-induced lattice expansion through the thermal annealing.

In order to complement the results obtained from X-ray based characterization, μ PL measurements of representative RT-implanted and HT-implanted Co:ZnO NWs were performed at 4 K with an excitation wavelength of

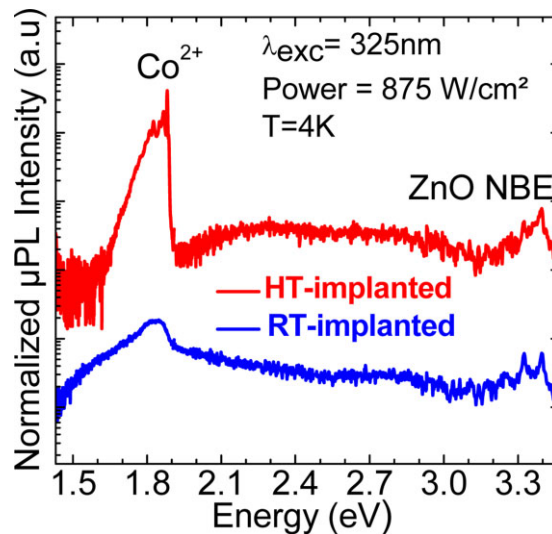


Figure 5 μ PL spectra of single RT-implanted and HT-implanted Co:ZnO NWs. The measurements were taken at 4 K using the continuous wave 325 nm HeCd laser.

325 nm. Figure 5 shows μ PL spectra of both RT-implanted and HT-implanted NWs. The spectra show two dominant peaks corresponding to ZnO near band edge (NBE) emission (~ 3.37 eV) and Co intra-3d-emission (Co^{2+} ~ 1.88 eV). The PL signal shows lower overall emission intensity of the RT-implanted NW than the HT-implanted one, indicating a high concentration of defects in the RT-implanted NW. The PL spectrum of the RT-implanted NW shows broader Co^{2+} emission and lower intensity compared to the HT-implanted one. Thus, a higher disorder is present around Co ions in the RT-implanted NW, in good agreement with the XANES results around Co K-edge. The PL spectrum of the HT-implanted NW shows low NBE emission and high Co^{2+} emission, confirming an excellent activation and also a good energy transfer to Co ions.

4 Conclusions We have characterized the RT-implanted and HT-implanted Co:ZnO NWs by the combination of four different and complementary techniques XRF, XANES, XRD and μ PL. The concentration and homogeneity of Zn and Co elements inside the NWs were studied through XRF nanoanalysis. The short range order was examined by nano-XANES, which revealed the substitutional incorporation of Co^{2+} ions into the Zn sites of the wurtzite host lattice, but with a high structural disorder for the RT-implanted NW. Preliminary XRD measurements suggested a lattice expansion for RT-implanted NW and a good recovery of implantation-induced damage for the HT-implanted NW. μ PL data analysis confirmed the highly distorted surrounding of Co ions in the RT-implanted NWs and the best optical activation of the HT-implanted Co.

Acknowledgements The authors thank R. Tucoulou and S. Labouré for their help with the experimental setup and I. Snigireva for the help with SEM imaging. This work has been partially

supported by the NANOWIRING Marie Curie ITN EU project (no. PITN-GA-2010-265073) and the DFG research unit FOR1616.

References

- [1] H. Ohno, *Science* **281**, 951 (1998).
- [2] P. Sharma, A. Gupta, K. V. Rao, F. J. Owens, R. Sharma, R. Ahuja, J. M. O. Guillen, B. Johansson, and G. A. Gehring, *Nature Mater.* **2**, 673 (2003).
- [3] Y. W. Heo, D. Norton, L. Tien, Y. Kwon, B. Kang, F. Ren, S. Pearton, and J. Laroche, *Mater. Sci. Eng. R* **47**, 1 (2004).
- [4] H. A. Weakliem, *J. Chem. Phys.* **36**, 2117 (1962).
- [5] S. Müller, M. Zhou, Q. Li, and C. Ronning, *Nanotechnology* **20**, 135704 (2009).
- [6] D. E. Perea, E. R. Hemesath, E. J. Schwalbach, J. L. Lensch-Falk, P. W. Woorhees, and L. J. Lauhon, *Nature Nanotechnol.* **4**, 315 (2009).
- [7] I. J. Chen, Y. C. Ou, Z. Y. Wu, F. R. Chen, J. J. Kai, J. J. Lin, and W. B. Jian, *J. Phys. Chem. C* **112**, 9168 (2008).
- [8] C. Ronning, C. Borschel, S. Geburt, and R. Niepelt, *Mater. Sci. Eng. R* **70**, 30 (2010).
- [9] C. Ronning, C. Borschel, S. Geburt, R. Niepelt, S. Müller, D. Stichtenoth, J.-P. Richters, A. Dev, T. Voss, L. Chen, W. Heimbrod, C. Gutsche, and W. Prost, *Phys. Status Solidi B* **247**, 2329 (2010).
- [10] J. Segura-Ruiz, G. Martínez-Criado, M. H. Chu, S. Geburt, and C. Ronning, *Nano Lett.* **11**, 5322 (2011).
- [11] C. Borschel and C. Ronning, *Nucl. Instrum. Methods Phys. Res. B* **269**, 2133 (2011).
- [12] C. Borchers, S. Müller, D. Stichtenoth, D. Schwen, and C. Ronning, *J. Phys. Chem. B* **110**, 1656 (2006).
- [13] G. Martínez-Criado, R. Tucoulou, P. Cloetens, P. Bleuet, S. Bohic, J. Cauzid, I. Kieffer, E. Kosior, S. Laboure, S. Petitgirard, A. Rack, J. Angel Sans, J. Segura-Ruiz, H. Suhonen, J. Susini, and J. Villanova, *J. Synchrotron Radiat.* **19**, 10 (2012).
- [14] V. A. Solé, E. Papillon, M. Cotte, Ph. Walter, and J. Susini, *Spectrochim. Acta B* **62**, 63 (2007).
- [15] J. C. Labiche, O. Mathon, S. Pascarelli, M. A. Newton, G. G. Ferre, C. Curfs, V. Vaughan, and A. Homs, *Rev. Sci. Instrum.* **78**, 091301 (2007).
- [16] B. Ravel and M. Newville, *J. Synchrotron Radiat.* **12**, 537 (2005).
- [17] A. P. Hammersley, S. O. Svensson, A. Thompson, H. Graafsma, Å. Kvick, and J. P. Moy, *Rev. Sci. Instrum.* **66**, 2729 (1995).
- [18] A. P. Hammersley, S. O. Svensson, M. Hanfland, A. N. Fitch, and D. Häusermann, *High Press. Res.* **14**, 235 (1996).
- [19] S. Geburt, A. Thielmann, R. Röder, C. Borschel, A. McDonnell, M. Kozlik, J. Kühnel, K. A. Sunter, F. Capasso, and C. Ronning, *Nanotechnology* **23**, 365204 (2012).
- [20] C. Borschel, R. Niepelt, S. Geburt, C. Gutsche, I. Regolin, W. Prost, F. J. Tegude, D. Stichtenoth, D. Schwen, and C. Ronning, *Small* **5**, 2576 (2009).
- [21] C. Song, K. W. Geng, F. Zeng, X. B. Wang, Y. X. Shen, F. Pan, Y. N. Xie, T. Liu, H. T. Zhou, and Z. Fan, *Phys. Rev. B* **73**, 024405 (2006).
- [22] A. Ney, K. Ollefs, S. Ye, T. Kammermeier, V. Ney, T. C. Kaspar, S. A. Chambers, F. Wilhelm, and A. Rogalev, *Phys. Rev. Lett.* **100**, 157201 (2008).
- [23] A. Zeuner, H. Alves, D. M. Hofmann, B. K. Meyer, M. Heuken, J. Blasing, and A. Kros, *Appl. Phys. Lett.* **80**, 2078 (2002).
- [24] S. Zhou, Q. Xu, K. Potzger, G. Talut, R. Grötzschel, J. Fassbender, M. Vinnichenko, J. Grenzer, M. Helm, H. Hochmuth, M. Lorenz, M. Grundmann, and H. Schmidt, *Appl. Phys. Lett.* **93**, 232507 (2008).
- [25] C. Liu, B. Mensching, M. Zeitler, K. Volz, and B. Rauschenbach, *Phys. Rev. B* **57**, 2530 (1998).

7

Nano-X-ray diffraction study of single Co-implanted ZnO nanowires

M. H. Chu, G. Martínez-Criado, J. Segura-Ruiz, S. Geburt, and C. Ronning

Nano-X-ray diffraction study of single Co-implanted ZnO nanowires

M. H. Chu^{*1}, G. Martínez-Criado^{**1}, J. Segura-Ruiz¹, S. Geburt², and C. Ronning²

¹ Experiments Division, European Synchrotron Radiation Facility, 38043 Grenoble, France

² Institute of Solid State Physics, University of Jena, 07743 Jena, Germany

Received 15 March 2014, revised 29 May 2014, accepted 11 June 2014

Published online 10 July 2014

Keywords Co-implanted ZnO, nanowires, X-ray diffraction, X-ray fluorescence

* Corresponding author e-mail mchu@esrf.fr, Phone: +33 04 76882931, Fax: +33 04 76882785

** e-mail: gmartine@esrf.fr

This work reports on the long-range order of single as-implanted and annealed ZnO:Co nanowires studied using a hard X-ray nanoprobe. For all nanowires, nano-X-ray fluorescence maps reveal a homogeneous distribution of Co ions implanted along the nanowires. For the as-implanted nanowires, however, nano-X-ray diffraction data shows a larger deviation from the bulk ZnO lattice along the *c*-axis induced by the ion implantation

process. For the thermally annealed nanowires, on the other hand, the *c* lattice parameter is similar to the one of bulk wurtzite ZnO. The structural analysis of individual nanowires highlights the importance of the subsequent thermal annealing and emphasizes the critical role of the unavoidable damage created by the ion-implantation process. Such defects ultimately limit the use of semiconductor nanowires.

© 2014 WILEY-VCH Verlag GmbH & Co. KGaA, Weinheim

1 Introduction Doping of semiconductor nanowires (NWs) is a critical step to produce materials with novel properties and functionalities for new devices [1]. In the context of spintronic nano-devices, transition metals (TMs) doped ZnO NWs have attracted much attention due to their predicted ferromagnetic behavior at a room temperature [2]. In addition, Co doped ZnO NWs have promising optical properties through the Co 3d intra-shell transitions for future optoelectronic applications [3]. One of the major challenges towards the successful use of NWs in emerging nanotechnologies is the controlled doping of the wires. Much effort has been endeavored for in-situ doping of NWs during the growth, for instance, via a wet chemical method [4], metal-organic chemical vapor deposition [5], and vapor–liquid–solid (VLS) [6]. However, an inhomogeneous dopant distribution and formation of secondary phases have been observed in the NWs. An alternative solution is *ex-situ* doping by ion implantation, which gives precise control of dopant homogeneity and concentration [7]. However, this method generally produces structural defects into the host structure, which can be reduced through a subsequent thermal annealing process. Therefore, a long lasting field of research is the understanding of the ion implantation induced lattice damage and further structural recovery during the post-implantation

thermal treatment, especially at the nanoscale [8]. For example, an extended X-ray absorption fine structure (EXAFS) study of ensemble of hydrogen and nitrogen ion-implanted ZnO nanorods has revealed an ion implantation-induced lattice distortion within the rods [9, 10]. Additionally, recent short-range order studies of single Co-implanted ZnO NWs have reported the local structural disorder induced by the ion implantation, as well as the structural recovery of the NWs by a thermal treatment [11, 12]. In this work, a detailed study on the long-range order of Co-implanted ZnO NWs is carried out using X-ray diffraction (XRD) technique at the nanoscale. The results provide a deeper insight into the ion-implantation-induced defects and the role of thermal treatments to recover structurally the single NWs.

2 Experimental details We have studied single Co-implanted ZnO NWs using a hard X-ray nanoprobe. The ZnO NWs were grown on p-Si (100) substrates using the VLS mechanism [13]. The synthesized NWs with fully random orientation on the substrates were implanted with Co ions at room temperature. For comparison, some implanted ZnO NWs were annealed at 750 °C in air for 4 h (labeled annealed ZnO:Co NWs) and some others do not undergo the thermal treatment (labeled as-implanted

ZnO:Co NWs). More details about the growth and Co implantation processes can be found elsewhere [13, 14].

For the X-ray characterization of single NWs, the as-implanted and annealed ZnO:Co NWs were dispersed on 200 nm thick SiN membranes in order to obtain isolated NWs. Prior to synchrotron measurements, the single NWs were located using an Olympus BX60F microscope and their morphology was studied using a Zeiss Leo 1530 scanning electron microscope (SEM) operated at 20 kV. The hard X-ray nanoprobe characterization was performed at the beamline ID22 of the European Synchrotron Radiation Facility [15]. The end-station ID22NI was equipped with a pair of Kirkpatrick–Baez multilayer coated Si mirrors, providing a spot size of $\sim 60 \times 60 \text{ nm}^2$ with a photon flux of $10^{12} \text{ ph s}^{-1}$ in pink beam mode, and $\sim 110 \times 110 \text{ nm}^2$, and $10^{10} \text{ ph s}^{-1}$ in monochromatic beam mode. The XRF data were analyzed with PyMca code [16]. The XRD signal was recorded by a fast readout low noise (FReLoN) CCD detector [17] at 28 keV in monochromatic beam mode. The XRD data reduction was performed with the Fit2D package [18].

3 Results Figure 1a displays the average XRF spectra of representative as-implanted and annealed ZnO:Co NWs. Both spectra show the $K_{\alpha,\beta}$ fluorescence signals of Co and Zn from the NWs, and Ar from the air. The escape peaks coming from the Si drift detector at 1.74 keV below the Zn parent lines are also observed. Several residual impurities such as Cr, Mn, Ba, Ga, and Fe are also present but, according to their homogeneous spatial distribution (not shown here), there is no incorporation into the NWs but contamination in the supporting SiN substrates [19].

To study the spatial distribution of the dopant in the NWs, the XRF spectra were fitted in a pixel-by-pixel approach. Figure 1c and e display the Co fluorescence maps with the corresponding concentrations for the as-implanted

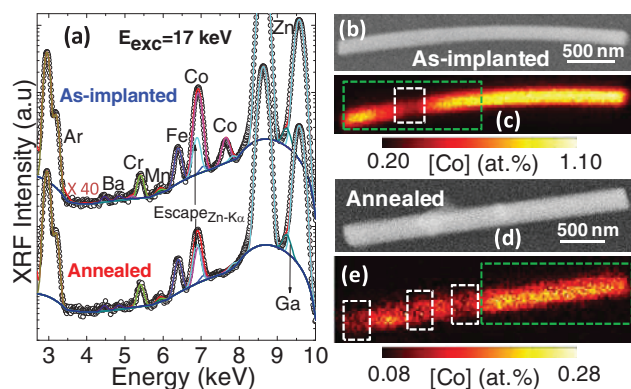


Figure 1 (a) Representative XRF spectra of an as-implanted ZnO:Co NW [shown in the SEM image Fig. 1b] and annealed NW [SEM image in Fig. 1d]. (c) and (e) are Co distribution maps with the estimation of the corresponding concentrations. White and green rectangles indicate positions with the overlapping of NWs during the ion implantation process, and regions where nano-XRD data were acquired, respectively.

and annealed ZnO:Co NWs, respectively. The Co maps show homogeneous distribution of the implanted ions along the NWs, except at some regions characterized by a lower Co concentration and indicated by white rectangles. These regions result from shadowing effects induced by NWs overlapping during the ion implantation process [12]. Through XRF quantification [16], the estimated Co concentration on the regions under the shadowing effects were (0.23 ± 0.03) and (0.10 ± 0.01) at.% for the as-implanted and annealed NWs, while outside these regions were (0.93 ± 0.14) and (0.24 ± 0.02) at.%, respectively. These concentrations on the regions without the shadowing effects are in good agreement with the simulated values obtained using the *iradina* code [20]. The different Co contents of both NWs are due to the different angle of the ion beam with respect to the NWs' axis as the NWs had a spaghetti-type geometry during the ion implantation [12].

In order to study the long-range order in the single as-implanted and annealed ZnO:Co NWs, nano-XRD data were acquired over the entire NWs in transmission mode with a step size of $100 \times 100 \text{ nm}^2$. The raw images from the CCD camera were corrected and integrated using the Fit2D program [18]. Figure 2 shows the XRD maps corresponding to the ZnO (002) reflection intensity acquired on the regions indicated by the green rectangles in Fig. 1 for the (a)

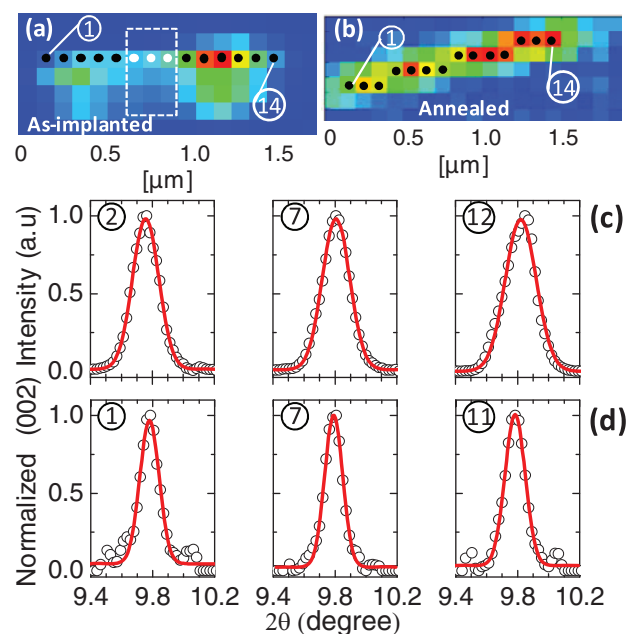


Figure 2 XRD (002) reflection intensity maps collected from the (a) as-implanted and (b) annealed NWs in the regions indicated by the green rectangles in Fig. 1. Solid black circles indicate the positions where 2θ XRD spectra were taken. Solid white circles show the positions under shadowing effects during the ion implantation process. Representative 2θ spectra of the ZnO (002) reflection (open circles) with the best single Gaussian fit (solid line) for the (c) as-implanted and (d) annealed NWs. Numbers on top of the spectra indicate the positions on the NWs [shown in Fig. 2a and b] where XRD spectra were acquired.

as-implanted and (b) annealed ZnO:Co NWs. The white rectangle of Fig. 2a represents the region affected by shadowing effects during ion implantation, characterized by a lower Co content. Figure 2c shows representative XRD data of ZnO (002) reflection acquired at the positions 2, 7, and 12 for the as-implanted ZnO:Co NW, according to the marks in the XRD map. Similarly, Fig. 2d displays the XRD at the positions 1, 7, and 11 for the annealed NW. Gaussian fitting values of these spectra are summarized in Table 1.

Figure 2c shows that at the regions with the lower [position 7] and higher [positions 2 and 12] Co concentrations of the as-implanted ZnO:Co NW the (002) reflection is dominated by a single Gaussian-like peak located at an average 2θ value of $(9.8 \pm 0.04)^\circ$. The XRD data of the as-implanted NW has been fitted with a single Gaussian curve. Similarly to Fig. 2c, Fig. 2d illustrates three representative 2θ spectra of the ZnO (002) reflection acquired at the positions 1, 7, and 11 [indicated in Fig. 2b] on the annealed ZnO:Co NW. For the latter case, all XRD also exhibit a single Gaussian contribution with narrower linewidths centered at an average 2θ position of $(9.79 \pm 0.03)^\circ$. Within the error bars, the average 2θ values of both as-implanted and annealed NWs are in agreement with the 2θ value of 9.77° obtained for the ZnO (002) reflection using the c lattice constant of bulk wurtzite ZnO (5.1948 \AA) [21]. However, the existence of a larger number of ion implantation-induced defects such as vacancies and interstitials in the as-implanted NW [26, 27] is clearly reflected in the FWHM values listed in Table 1. Such defects are reduced through the post-implantation thermal annealing, resulting in a better long-range order for the annealed NW.

To gain further insight into the defect distribution in the NWs, Fig. 3a reveals the FWHM values of the ZnO (002) reflections along the as-implanted (open squares) and annealed (open circles) NWs. As expected, the FWHM values along the as-implanted NW are larger than those of the annealed NWs. These confirm the higher density of defects along the as-implanted NW than along the annealed one. The FWHM values vary significantly along the as-implanted NWs, especially on the right region. This is due to the existence of an unbalance of the ion implantation induced defects between the different regions of the NW. Such unbalance of the induced defects is also the cause for the bending of the NW [shown in Fig. 1b] [12]. In contrast, the FWHM values along the annealed NW show a small change between one to the other. This indicates that the unbalance of defects is also reduced through the thermal

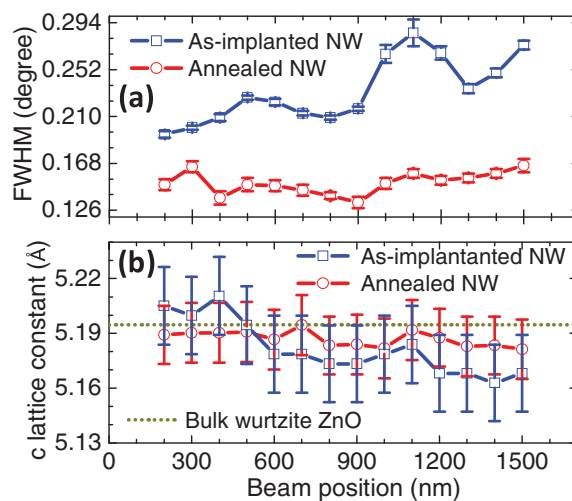


Figure 3 (a) FWHM and (b) estimated c lattice constant values from ZnO (002) reflections, respectively, along the as-implanted (open squares) and annealed (open circles) ZnO:Co NWs. The c lattice parameter of bulk wurtzite ZnO (dotted line) [21] is also shown in Fig. 3b.

treatment [the NW's shape is more straight as shown in Fig. 1d].

In order to obtain information on the lattice parameter of ZnO:Co along the NW, the relationship between the interplanar spacing (d_{hkl}) and the unit cell constants a and c in the hexagonal structure was used to estimate the c lattice constant from the symmetric (002) reflection: $1/d_{hkl}^2 = 4(h^2 + hk + k^2)/3a^2 + l^2/c^2$. Figure 3b shows the c lattice constants obtained from the ZnO (002) reflections of the as-implanted (open squares) and annealed (open circles) NWs. The c value is around $(5.19 \pm 0.02) \text{ \AA}$ along the annealed NW while it ranges from (5.16 ± 0.02) to $(5.21 \pm 0.02) \text{ \AA}$ along the as-implanted NW. By comparing the c lattice constants of both NWs with the one of 5.1948 \AA reported for bulk wurtzite ZnO (dotted line) [21], as shown in Fig. 3b, the deviation of the c lattice parameter values around the one of bulk ZnO is larger for the as-implanted NW than for the annealed one. However, the change of the lattice parameter reported in the present work is in excellent agreement with the values observed from ensembles of NWs and ZnO powder in previous reports [22, 23] and matches very well with EXAFS results [10, 24, 25]. Within the experimental accuracy, the c values of the annealed NW are

Table 1 Summary of 2θ peak positions and FWHMs obtained from single Gaussian fits of the ZnO (002) XRD of the as-implanted and annealed ZnO:Co NWs. Numbers in the round brackets are uncertainty values.

ZnO (002)	as-implanted NW			annealed NW		
	②	⑦	⑫	①	⑦	⑪
2θ (degrees)	9.76 (0.04)	9.81 (0.04)	9.82 (0.04)	9.78 (0.03)	9.79 (0.03)	9.78 (0.03)
FWHM (degrees)	0.200 (0.002)	0.209 (0.002)	0.235 (0.005)	0.149 (0.005)	0.139 (0.003)	0.153 (0.004)

equal to the value of 5.1948 Å for the bulk ZnO, indicating that the damaged crystal structure was restored through the thermal annealing [11, 12].

Based on EXAFS fitting results of both as-implanted and annealed NWs reported in a previous work [12], c lattice constants can be also deduced by using a simple calculation: $R_{\text{Zn-O}} = uc$, where the internal parameter $u = \sqrt{3}/8(a/c) = 0.38$ [28]. As a result, the calculated c lattice constants of the as-implanted and annealed NWs are (5.24 ± 0.03) and (5.16 ± 0.05) Å, respectively. Within the error bars, both c values are equal to the average values obtained from the XRD analyses. In addition, the Debye Waller factor of the second nearest neighbor shell is larger for the as-implanted NW $[(8.9 \pm 1.7) \times 10^{-3}]$ than for the annealed NW $[(8.9 \pm 1.7) \times 10^{-3}]$. It indicates a higher static disorder along the as-implanted NW compared to the annealed one, as corroborated by the larger FWHM values of the ZnO (002) reflections. A rough comparison of the findings obtained by XRD and EXAFS techniques results in a full agreement between the short- and long-range orders. On the other hand, for the annealed NW, the same c lattice constants obtained from the XRD and EXAFS data analyses, which are equal to the value of bulk ZnO, confirm the good recovery of the damaged structure through the thermal treatment.

4 Conclusion We have studied single Co-implanted ZnO NWs by synchrotron nanoprobe-based techniques. The nano-XRF data analysis has allowed to study the homogeneity and concentration of the implanted Co along the NWs. The nano-XRD findings revealed the structural modifications of the as-implanted NWs. In particular, a distortion of the c lattice constant along the c -axis was exhibited because of the ion implantation-induced defects, which were reduced through a thermal annealing process. Our results have highlighted the importance of the post-implantation thermal treatment and provided new insights into the implication of structural defect formation generated by the ion implantation process in single NWs. The overall results also open new avenues for the application of synchrotron based multi-techniques for detailed study of single semiconductor NWs at the nanometer length scale.

Acknowledgements The authors thank R. Tucoulou and S. Labor for their help with the experimental setup and I. Snigireva for the SEM measurements. This work has been partially supported by the NANOWIRING Marie Curie ITN EU project (No. PITN-GA-2010-265073) and the DFG research unit FOR1616.

References

- [1] T. J. Kempa, B. Tian, D. R. Kim, J. Hu, X. Zheng, and C. M. Lieber, *Nano Lett.* **8**, 3456 (2008).
- [2] T. Dietl, *Nature Mater.* **9**, 965 (2010).
- [3] S. Miiller, M. Zhou, Q. Li, and C. Ronning, *Nanotechnology* **20**, 135704 (2009).
- [4] B. D. Yuhas, D. O. Zitoun, P. J. Pauzuskie, R. He, and P. Yang, *Angew. Chem.* **45**, 420 (2006).
- [5] C.-H. Chen, S.-J. Chang, S.-P. Chang, M.-J. Li, I.-C. Chen, T.-J. Hsueh, A.-D. Hsu, and C.-L. Hsu, *J. Phys. Chem. C* **114**, 12422 (2010).
- [6] D. E. Perea, E. R. Hemesath, E. J. Schwalbach, J. L. Lensch-Falk, P. W. Voorhees, and L. J. Lauhon, *Nature Nanotechnol.* **4**, 315 (2009).
- [7] I.-J. Chen, Y.-C. Ou, Z.-Y. Wu, F.-R. Chen, J.-J. Kai, J.-J. Lin, and W.-B. Jian, *J. Phys. Chem. C* **112**, 9168 (2008).
- [8] A. Y. Azarov, B. G. Svensson, and A. Y. Kuznetsov, *Appl. Phys. Lett.* **101**, 222109 (2012).
- [9] Y.-B. Lee, C.-H. Kwak, S.-Y. Seo, S.-H. Kim, C.-I. Park, B.-H. Kim, S.-H. Park, Y. D. Choi, and S.-W. Han, *J. Korean Phys. Soc.* **56**, 2050 (2010).
- [10] C.-H. Kwak, Y.-B. Lee, S.-Y. Seo, S.-H. Kim, C.-I. Park, B.-H. Kim, D. Jeong, J. Kim, Z. Jin, and S.-W. Han, *Curr. Appl. Phys.* **11**, S328 (2011).
- [11] J. Segura-Ruiz, G. Martinez-Criado, M. H. Chu, S. Geburt, and C. Ronning, *Nano Lett.* **11**, 5322 (2011).
- [12] M. H. Chu, G. Martinez-Criado, J. Segura-Ruiz, S. Geburt, and C. Ronning, *Appl. Phys. Lett.* **103**, 141911 (2013).
- [13] C. Borchers, S. Miiller, D. Stichtenoth, D. Schwen, and C. Ronning, *J. Phys. Chem. B* **110**, 1656 (2006).
- [14] C. Ronning, C. Borschel, S. Geburt, and R. Niepelt, *Mater. Sci. Eng. R* **70**, 30 (2010).
- [15] G. Martínez-Criado, R. Tucoulou, P. Cloetens, P. Bleuet, S. Bohic, J. Cauzid, I. Kieffer, E. Kosior, S. Labouré, S. Petitgirard, A. Rack, J. A. Sans, J. Segura-Ruiz, H. Suhonen, J. Susini, and J. Villanova, *J. Synchrotron Radiat.* **19**, 10 (2012).
- [16] V. A. Solé, E. Papillon, M. Cotte, P. Walter, and J. Susini, *Spectrochim. Acta B* **62**, 63 (2007).
- [17] J.-C. Labiche, O. Mathon, S. Pascarelli, M. A. Newton, G. G. Ferre, C. Curfs, G. Vaughan, A. Homs, and D. F. Carreiras, *Rev. Sci. Instrum.* **78**, 091301 (2007).
- [18] A. P. Hammersley, S. O. Svensson, A. Thompson, H. Graafsma, A. Kvick, and J. P. Moy, *Rev. Sci. Instrum.* **66**, 2729 (1995).
- [19] M. H. Chu, J. Segura-Ruiz, G. Martinez-Criado, P. Cloetens, I. Snigireva, S. Geburt, and C. Ronning, *Phys. Status Solidi RRL* **5**, 283 (2011).
- [20] C. Borschel and C. Ronning, *Nucl. Instrum. Methods Phys. Res. B* **269**, 2133 (2011).
- [21] F. Decremps, F. Datchi, A. M. Saitta, A. Polian, S. Pascarelli, A. Di Cicco, J. P. Itié, and F. Baudelet, *Phys. Rev. B* **68**, 104101 (2003).
- [22] S. W. Han, H. J. Yoo, S. J. An, and G. C. Yi, *Appl. Phys. Lett.* **86**, 021917 (2005).
- [23] S. Maensiri, P. Laokul, and V. Promarak, *J. Cryst. Growth* **289**, 102 (2006).
- [24] J. U. Brehm, M. Winterer, and H. Hahn, *J. Appl. Phys.* **100**, 064311 (2006).
- [25] L. Y. Chen, Y. T. Yin, C. H. Chen, and J. W. Chiou, *J. Phys. Chem. C* **115**, 20913 (2011).
- [26] C. Liu, B. Mensching, M. Zeitler, K. Volz, and B. Rauschenbach, *Phys. Rev. B* **57**, 2530 (1998).
- [27] M. Mamor, V. Matias, A. Vantomme, A. Colder, P. Marie, and P. Ruterana, *Appl. Phys. Lett.* **85**, 2244 (2004).
- [28] E. H. Kisi and M. M. Elcombe, *Acta Cryst. C* **45**, 1867 (1989).

7. NANO-X-RAY DIFFRACTION STUDY OF SINGLE CO-IMPLANTED ZNO NANOWIRES

8

**Intense intra-*3d* luminescence and
waveguide properties of single
Co-doped ZnO nanowires**

S. Geburt, R. Röder, U. Kaise, L. Chen, M. H. Chu, J. Segura-Ruiz, G. Martínez-Criado, W. Heimbrodtt, and C. Ronning

Intense intra-3d luminescence and waveguide properties of single Co-doped ZnO nanowires

Sebastian Geburt¹, Robert Röder¹, Uwe Kaiser², Limei Chen³, Manh-Hung Chu⁴, Jaime Segura-Ruiz⁴, Gema Martínez-Criado⁴, Wolfram Heimbrodt², and Carsten Ronning^{*,1}

¹ Friedrich-Schiller-University Jena, Institute for Solid State Physics, Max-Wien-Platz 1, 07743 Jena, Germany

² Philipps-University Marburg, Institute of Physics and Material Science Center, Renthof 5, 35032 Marburg, Germany

³ Justus-Liebig-University Gießen, I. Physical Institute, Heinrich-Buff-Ring 16, 35392 Gießen, Germany

⁴ European Synchrotron Radiation Facility, Experiments Division, 6 rue Jules Horowitz, BP 220, 38043 Grenoble Cedex, France

Received 28 May 2013, revised 20 June 2013, accepted 21 June 2013

Published online 27 June 2013

Keywords ZnO, nanowires, ion implantation, doping, luminescence, waveguides

* Corresponding author: e-mail Carsten.Ronning@uni-jena.de, Phone: +49 3641 947 300, Fax: +49 3641 947 302

Successful doping of ZnO nanowires with the transition metal cobalt was achieved by ion implantation. Excellent optical activation of the incorporated Co ions was observed from nanowire ensembles after annealing. Efficient excitation of the Co ions occurs either by near resonant absorption or by energy transfer from the ZnO host. The excited Co ions decay

radiatively with a lifetime of 8 ns. Intense and homogeneous Co²⁺ intra-3d luminescence was observed from single nanowires with different Co concentrations in the range of 0.02–4 at% and at various excitation powers. Spatially resolved measurements allowed the characterization of the waveguide properties of single doped nanowires.

© 2013 WILEY-VCH Verlag GmbH & Co. KGaA, Weinheim

1 Introduction Doping of semiconductors is very attractive in order to create material systems with novel properties and functionalities. The doping of ZnO with transition metals has attracted an enormous interest in the past decade, as this material combination has the potential to act as a diluted magnetic semiconductor (DMS) [1]. However, transition metals like cobalt (Co) are also well-known optically active luminescence centers in semiconductors [2]; thus, this system is likewise very interesting also from an optical point of view. Especially in the form of nanowires, this material system would take advantage of photonic waveguiding and provide complete new possibilities for future optoelectronic nano-devices such as light-emitting diodes (LED) or nano-lasers [3].

Doping of semiconductor nanowires during growth is a challenging task, as the self-organized growth mechanisms are sensitive to changes in the growth conditions. Doping of ZnO nanowires with Co via wet chemical methods is possible [4], but the control of the dopant concentra-

tion is not precise and the crystal quality is worse compared to vapour–liquid–solid (VLS) grown nanowires [5]. In general it was observed that doping during VLS growth tends to provide only an inhomogeneous dopant distribution [6] and the dopant concentration is typically limited to the low solubility in the solid phase [7]. A successful alternative is the doping by ion implantation, which can overcome all the drawbacks and provides doping with nearly every element in the desired concentration [8]. However, the damage created by the high-energetic ions has to be recovered by optimized annealing procedures in order to obtain activation of the implanted impurities.

In this Letter, we will present a route for the successful ion beam doping and optical activation of the implanted Co ions in ZnO nanowires. The experiments focus on the novel optical properties of single Co-doped ZnO nanowires.

2 Experimental details ZnO nanowires (NW) with diameters of typically 100 to 500 nm and lengths of more

than 10 μm were synthesized by the VLS mechanism in a horizontal tube furnace [5]. The ion implantation was simulated using the Monte-Carlo package *iradina* [9], which takes into account the three-dimensional nanowire morphology. Several ion energies from 30 keV to 380 keV were simulated and their superposition yielded a homogeneous doping profile. Ion implantation was performed at room temperatures using ^{59}Co ion fluences of $7.8 \times 10^{14} \text{ cm}^{-2}$ to $1.2 \times 10^{17} \text{ cm}^{-2}$, resulting in concentrations of 0.02 at% to 4 at%, respectively. The irradiation damage was recovered by annealing in air at 750 $^{\circ}\text{C}$ for 120 min.

The morphology and luminescence properties were investigated using a JEOL JSM-6490 scanning electron microscope (SEM) equipped with Gatan MonoCL³⁺ cathodoluminescence (CL) unit. The electron energy of 10 keV used for all CL investigations was derived from simulations of the electron–solid interactions using the Monte-Carlo package Casino [10] to ensure the excitation of the entire nanowire volume by the electron beam. Monochromatic CL images were acquired using a high-sensitivity photomultiplier (PMT) coupled to a grating monochromator at a bandwidth of 5 nm. CL spectra were detected using a back-illuminated charged-coupled device (CCD) camera. The photoluminescence excitation (PLE) spectra were recorded using a halogen/Xe lamp combination attached to an excitation monochromator for wavelength-selective excitation. The PLE signal of the sample was detected by a high-sensitivity PMT mounted behind a prism monochromator. The PLE spectra were corrected for the emission characteristics of the lamps. Time-resolved photoluminescence (TRPL) measurements were performed using excitation by a frequency-tripled Nd:YAG laser (pulse FWHM 3 ns) and detection by a grating monochromator with an intensified CCD (iCCD) camera using a gate width of 5 ns [11]. The photoluminescence and waveguide properties of single nanowires were investigated using a self-built epifluorescence microscope [12] with excitation by a continuous-wave 325 nm HeCd laser. All luminescence measurements were performed at a sample temperature of 10 K or below.

3 Results and discussion The morphology and structural properties of the Co-implanted ZnO nanowires were extensively investigated in previous studies using a nano-sized X-ray beam and TEM [13]. Briefly summarizing the important facts for this study, the implanted Co atoms are homogeneously distributed along the wires and the measured cobalt content fits well to the *iradina* simulations. The Co atoms occupy Zn lattice sites in a 2⁺ charge state, and high structural order of the host lattice was observed and confirmed the recovery of the radiation-damaged ZnO structure through the subsequent annealing step.

The emission properties of such ZnO nanowires with a Co concentration of about 0.5 at% within an ensemble were investigated by cathodoluminescence. The respective spectrum in Fig. 1(a) is composed of the intense recombi-

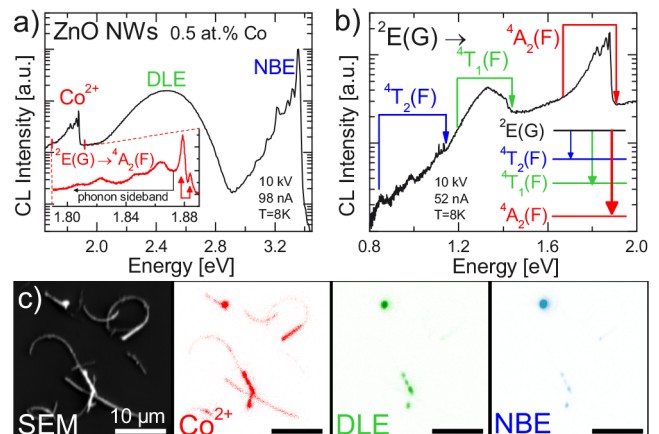


Figure 1 (a) Cathodoluminescence survey spectrum of a Co-implanted ZnO nanowire ensemble shows the Co^{2+} emission, which consists of sharp intra-3d transitions accompanied by a sideband of local phonon modes at the low-energy side (inset). (b) Several intra-3d transitions could be identified from the excited ${}^2\text{E}(\text{G})$ to the lower Co ${}^4\text{T}(\text{F})$ levels and the ${}^4\text{A}_2(\text{F})$ ground term. (c) The monochromatic CL images show the strong and homogeneous Co^{2+} emission from single dispersed NWs, while the ZnO excitonic and defect emission originates only from thick nanowire areas.

nation of free and bound excitons in the ZnO near-band-edge (NBE) emission above 3 eV [14] and a broad emission band around 2.5 eV associated with the recombination of carriers at intrinsic ZnO defects (deep-level emission, DLE) [15]. The sharp and structured emission feature at 1.88 eV is attributed to the Co^{2+} intra-3d luminescence [16], which could be identified in the high-resolution spectrum as a set of sharp transitions from the excited ${}^2\text{E}(\text{G})$ level to the ${}^4\text{A}_2(\text{F})$ ground term [16, 17] (marked by arrows in the inset of Fig. 1(a)) accompanied by a phonon side band on the low-energy side [18]. Thus, successful doping and optical activation of the Co ions was achieved for the implanted ZnO nanowires. Further emission peaks were observed in the near-infrared range shown in Fig. 1(b) and could be attributed to less intense Co^{2+} intra-3d transitions from the excited ${}^2\text{E}(\text{G})$ to the ${}^4\text{T}_1(\text{F})$ level at 1.4 eV and to the ${}^4\text{T}_2(\text{F})$ level from 0.85 eV to 1.13 eV [2, 16, 17].

Single implanted ZnO NWs with 0.5 at% Co were dispersed onto clean Si substrates in order to investigate the emission homogeneity. The respective SEM image was combined with monochromatic CL images of the Co^{2+} emission at 1.88 eV, the DLE emission at 2.5 eV and NBE emission at 3.3 eV in Fig. 1(c). The Co-implanted nanowires show an intense and uniform intra-3d luminescence, while the DLE and NBE emission are only locally emitted from thicker parts of the wires. In order to gain further information, the emission properties of single doped nanowires were investigated for different diameters between 100 nm and 500 nm. The CL spectra for nanowires between 100 nm and 300 nm (not shown) were similar and comparable to the μPL spectra of single wires in Fig. 3(a) at equivalent excitation power. For thicker nanowires, the

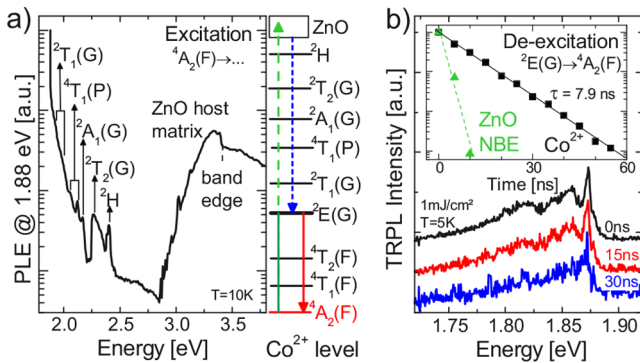


Figure 2 (a) The PLE spectrum of Co-doped ZnO nanowire ensemble shows the resonant excitation of higher Co^{2+} states and the effective energy transfer from the ZnO host matrix to the luminescent Co ion. (b) The time-resolved PL spectra exhibit no spectral change at different times after excitation for a NW ensemble with a Co concentration of 0.5 at%. The transient (inset) can be fitted using a mono-exponential function with a natural Co^{2+} lifetime of $\tau = 7.9$ ns.

ZnO-related emission increased and finally dominated the spectrum for diameters >500 nm. This can be understood as the maximum range for the implanted Co atoms is about 300 nm. Thus, thicker wires are not completely implanted; therefore, the ZnO emission originates mainly from the non-irradiated and unaffected areas of the nanowires.

The PLE spectrum of a Co-implanted ZnO NW ensemble (0.5 at%) shown in Fig. 2(a) was monitored at the ${}^2\text{E}(\text{G}) \rightarrow {}^4\text{A}_2(\text{F})$ intra-3d transition (1.88 eV). Several excitation pathways of the Co ions can occur: The strong PLE signal above 3.0 eV reveals the efficient energy transfer from the ZnO host to the Co ions. The modulations at lower energies can be assigned to direct excitations of higher Co^{2+} levels, where the excitation probability decreases with increasing level. This may be due to the multiple non-radiative decay down to the luminescent ${}^2\text{E}(\text{G})$ level [2, 19].

The temporal decay of the excited Co ions embedded in ZnO nanowires (0.5 at%) is presented in Fig. 2(b). No change in the emission line shape was detected within the examined time range, as it is expected for an intra-3d transition [20]. The integrated TRPL signal can be fitted using a mono-exponential function with a radiative lifetime of $\tau = 7.9$ ns, indicating that the Co intra-3d transition is strongly allowed [21]. The additionally monitored decay of the ZnO excitonic emission (NBE) is much faster (typically < 1 ns) [22], also shown in the inset of Fig. 2(b), and thus limited by the temporal resolution of our measuring system. The evaluated radiative lifetime of Co^{2+} ions in ZnO nanowires is slightly faster than the lifetime reported for diluted Co ions in a ZnO single crystal ($\tau \sim 15$ ns, [23]). For the used high doping level in this study, resonant energy transfers between the Co ions become important and significantly shorten the lifetime.

The emission properties of single NWs with typically 300 nm diameter and about 10 μm length were investi-

gated for different Co concentrations between 0.02 at% and 4 at%. The μPL spectra are displayed in Fig. 3(a). Nanowires with a low Co concentration show a strong ZnO excitonic emission and only a weak Co intra-3d luminescence. The optimum concentration for an intense Co^{2+} emission was found around 0.5 at%. At higher Co concentrations, the implantation damage could not be completely recovered, yielding a significant increase of the defect emission compared to the NBE and Co^{2+} emission.

The waveguide properties of one Co-doped ZnO nanowire (0.5 at%) was investigated using spatially resolved μPL spectroscopy. The emission from the location of the focused laser spot and the waveguided emission from the nanowire end (see inset) are plotted in Fig. 3(b). The respective red and black spectra are similar in shape, but the intensity of the NW-end emission is typically reduced by a factor of 3–5. Especially, the emission ratio, which is plotted also in Fig. 3(b) as a blue line, shows a reduced transmission for higher photon energies, which can be explained by absorption of the ZnO along the nanowire [24]. The dip at the energy of the Co emission is interpreted as resonant absorption and isotropic re-emission of the Co ions. Thus, the transmission is lower at the energy of the Co^{2+} emission than at energies below or above.

The emission of one single Co-doped ZnO nanowire with a diameter of 180 nm and length of 9 μm (see SEM inset of Fig. 4(b)) was investigated as a function of excitation power. The μPL spectra are dominated by the Co^{2+} emission at low excitation densities, as shown in Fig. 4(a). At elevated excitation powers, the ZnO excitonic and defect emission as well as the Co^{2+} emission increase in intensity with linear-power behavior. Differences appear above 1000 W/cm^2 , as the Co intra-3d emission shows a significant broadening and a deviation from the linear increase, which can be attributed to local heating by the focused cw laser beam and a saturation of the excited Co

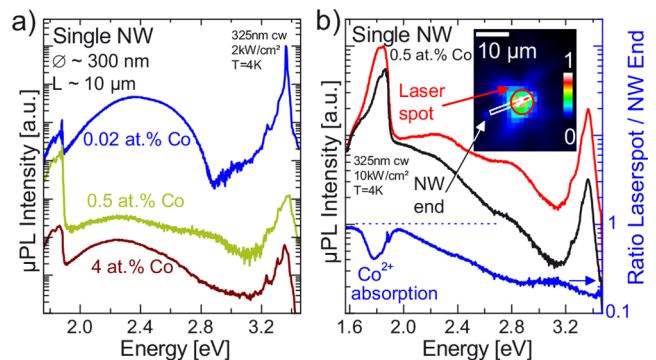


Figure 3 (a) The μPL spectra of representative single Co-doped ZnO nanowires with concentrations between 0.02 at% and 4 at% reveal the most intense Co^{2+} intra-3d emission for 0.5 at%. (b) Waveguiding of a single Co-implanted ZnO NW (0.5 at%). The ratio between the emission intensity at the laser spot and the emission at the nanowire end shows a strong absorption around 1.8 eV due to the incorporated Co ions.

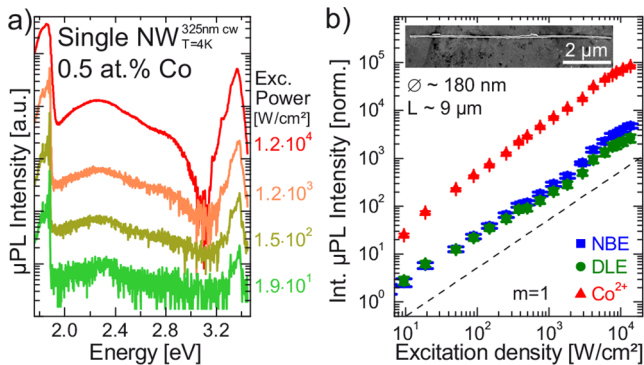


Figure 4 (a) The μ PL body emission spectra of one single ZnO:Co nanowire are plotted as a function of the excitation power. (b) The integrated emission intensity of the Co^{2+} emission emerges about linearly with pumping power. The inset shows the SEM image of the investigated nanowire.

ions, respectively. Thus, no light amplification was observed, but could be expected for higher power levels; however, the diameter of the investigated nanowire was too small to establish sufficient waveguiding and gain [12].

4 Conclusions ZnO nanowires can be successfully doped with Co by ion implantation. After annealing, the Co ions are on Zn lattice sites, in 2^+ charge state, in a recovered surrounding, optically activated and emit an intense intra-3d luminescence in the VIS and NIR range. Single doped nanowires show a homogeneous Co^{2+} emission, while the ZnO emission mainly originates from unimplanted parts within the nanowires. The Co ions can be efficiently excited by energy transfer from the ZnO host or resonant into higher levels and decay with a lifetime of ~ 8 ns. The most intense Co emission is found for doping concentrations of 0.5 at%. The Co-doped nanowires emit waveguided emission from their ends with an enhanced absorption in the range of the Co emission. The spectra of one single doped nanowire at different excitation powers follow a linear emission increase with power up to 1000 W/cm^2 .

Acknowledgements The authors acknowledge funding by the German Research Society DFG within the project FOR1616 and funding by the EU within the ITN Marie Curie program “Nanowiring”.

References

- [1] T. Dietl, *Nature Mater.* **9**, 965 (2010).
- [2] H. A. Weakliem, *J. Chem. Phys.* **36**, 2117 (1962).
- [3] Y. Huang, X. Duan, and C. Lieber, *Small* **1**, 142 (2005).
- [4] B. D. Yuhas, D. O. Zitoun, P. J. Pauzauskie, R. He, and P. Yang, *Angew. Chem.* **118**, 434 (2006).
- [5] C. Borchers, S. Müller, D. Stichtenoth, D. Schwen, and C. Ronning, *J. Phys. Chem. B* **110**, 1656 (2006).
- [6] D. E. Perea, E. R. Hemesath, E. J. Schwalbach, J. L. Lensch-Falk, P. W. Voorhees, and L. J. Lauhon, *Nature Nanotechnol.* **4**, 315 (2009).
- [7] D. Lide (ed.), *CRC Handbook of Chemistry and Physics* (CRC Press, Boca Raton, Florida, USA, 1996).
- [8] C. Ronning, C. Borschel, S. Geburt, and R. Niepelt, *Mater. Sci. Eng. R, Reports* **70**, 30 (2010).
- [9] C. Borschel and C. Ronning, *Nucl. Instrum. Methods B* **269**, 2133 (2011).
- [10] D. Drouin, A. R. Couture, D. Joly, X. Tastet, V. Aimez, and R. Gauvin, *Scanning* **29**, 92 (2007).
- [11] L. Chen, T. Niebling, W. Heimbrodt, D. Stichtenoth, C. Ronning, and P. J. Klar, *Phys. Rev. B* **76**, 115325 (2007).
- [12] S. Geburt, A. Thielmann, R. Röder, C. Borschel, A. McDonnell, M. Kozlik, J. Kühnel, K. A. Sunter, F. Capasso, and C. Ronning, *Nanotechnology* **23**, 365204 (2012).
- [13] J. Segura-Ruiz, G. Martinez-Criado, M. H. Chu, S. Geburt, and C. Ronning, *Nano Lett.* **11**, 5322 (2011).
- [14] B. K. Meyer, H. Alves, D. M. Hofmann, W. Kriegseis, D. Forster, F. Bertram, J. Christen, A. Hoffmann, M. Straßburg, M. Dworzak, U. Haboeck, and A. V. Rodina, *Phys. Status Solidi B* **241**, 231 (2004).
- [15] S. Müller, M. Lorenz, C. Czekalla, G. Benndorf, H. Hochmuth, M. Grundmann, H. Schmidt, and C. Ronning, *J. Appl. Phys.* **104**, 123504 (2008).
- [16] P. Koidl, *Phys. Rev. B* **15**, 2493 (1977).
- [17] R. S. Anderson, *Phys. Rev.* **164**, 398 (1967).
- [18] S. Müller, M. Zhou, Q. Li, and C. Ronning, *Nanotechnology* **20**, 135704 (2009).
- [19] H.-J. Schulz and M. Thiede, *Phys. Rev. B* **35**, 18 (1987).
- [20] J. J. Chen, M. H. Yu, W. L. Zhou, K. Sun, and L. M. Wang, *Appl. Phys. Lett.* **87**, 173119 (2005).
- [21] J. Donegan, T. Glynn, and G. Imbusch, *J. Lumin.* **45**, 23 (1990).
- [22] T. Koida, S. F. Chichibu, A. Uedono, A. Tsukazaki, M. Kawasaki, T. Sota, Y. Segawa, and H. Koinuma, *Appl. Phys. Lett.* **82**, 532 (2003).
- [23] R. M. Macfarlane and J. C. Viala, *Mater. Sci. Forum* **10–12**, 845 (1986).
- [24] J. F. Muth, R. M. Kolbas, A. K. Sharma, S. Oktyabrsky, and J. Narayan, *J. Appl. Phys.* **85**, 7884 (1999).

**8. INTENSE INTRA-3D LUMINESCENCE AND WAVEGUIDE
PROPERTIES OF SINGLE CO-DOPED ZNO NANOWIRES**

Appendix A

Synchrotron nanoimaging of single In-rich InGaN nanowires

J. Segura-Ruiz, G. Martínez-Criado, M. H. Chu, C. Denker, J. Malindretos, and
A. Rizzi

Synchrotron nanoimaging of single In-rich InGaN nanowires

J. Segura-Ruiz,^{1,a)} G. Martínez-Criado,¹ M. H. Chu,¹ C. Denker,² J. Malindretos,² and A. Rizzi²

¹European Synchrotron Radiation Facility, Experiments Division, 38043 Grenoble, France

²Georg-August-Universität Göttingen, IV. Physikalisches Institut, 37077 Göttingen, Germany

(Received 17 August 2012; accepted 21 February 2013; published online 29 March 2013)

This work reports on the elemental distribution and local structure of single $\text{In}_x\text{Ga}_{1-x}\text{N}$ nanowires (NWs) grown by molecular beam epitaxy on Si (111) substrates using X-ray fluorescence nanoprobe. Ga and In maps reveal an inhomogeneous elemental distribution along the NWs, with a higher Ga concentration at the bottom of the NW. Scanning electron microscopy images show that the inhomogeneous axial distribution is not correlated with a X-ray beam induced damage, and therefore, should be an intrinsic characteristic of the NWs arising from the growth process. Spatially resolved X-ray absorption near edge structure spectroscopy data acquired around the In K-edge show that the tetrahedral structure is preserved around the absorbing In-atoms all along the NW, and suggests that the compositional modulation could be affecting its long-range order. © 2013 American Institute of Physics. [<http://dx.doi.org/10.1063/1.4795544>]

I. INTRODUCTION

In recent years, special attention has been paid to $\text{In}_x\text{Ga}_{1-x}\text{N}$ alloy mainly due to their good optical and electrical properties for potential optoelectronic applications. In 2002, after the characterization of high quality InN layers grown by molecular beam epitaxy (MBE),^{1,2} its bandgap was reassigned to (0.67 ± 0.05) eV.^{3,4} This new value extended the range of tunability of the $\text{In}_x\text{Ga}_{1-x}\text{N}$ bandgap over nearly the entire solar spectrum.^{5,6} Therefore, multijunction solar cells could take advantage of $\text{In}_x\text{Ga}_{1-x}\text{N}$, promising very high conversion efficiencies. Despite the interest in this material, the growth of high crystalline quality $\text{In}_x\text{Ga}_{1-x}\text{N}$ in the entire compositional range without segregation effects remains a challenge. Indeed, there are several reports on the elemental segregation in $\text{In}_x\text{Ga}_{1-x}\text{N}$ layers and quantum wells.^{7,8} The nanowire (NW) morphology is a novel approach that can reduce the elemental segregation and improves the crystalline quality of this alloy. It is known that the NW morphology favours lateral elastic relaxation,⁹ allowing a larger lattice mismatch than in layers. For instance, vertically self-aligned GaN NWs grown spontaneously by MBE—no seeds or catalyst are required—are nearly dislocation free and present intense and narrow excitonic emission peaks in the UV range.^{10,11} Indeed, $\text{In}_x\text{Ga}_{1-x}\text{N}$ NWs have also been grown by low-temperature halide chemical vapour deposition technique, covering almost the full alloy compositional range.¹² However, these NWs are not well oriented, and the compositional modulation remains for high In-content. Furthermore, In-rich NWs grown by this technique exhibit blue shifted emission due to a high level of unintentional doping. On the other hand, $\text{In}_x\text{Ga}_{1-x}\text{N}$ NWs grown by MBE technique are well oriented and the oxygen-free and low-hydrogen environment could reduce the persistent unintentional doping. However, there are reports on the elemental segregation in ternary III-V NWs grown also by MBE and metal-organic vapor phase epitaxy^{13,14} that would indicate

this is a general problem that cannot be completely eliminated by the NW morphology. Despite the great interest attracted by the $\text{In}_x\text{Ga}_{1-x}\text{N}$ nanostructures, there are only few reports on the quantitative analysis of the elemental modulation of single $\text{In}_x\text{Ga}_{1-x}\text{N}$ NWs^{15–17} and many open questions, for instance the effect of the elemental modulation on the local atomic structure of the single NWs. We have recently demonstrated the usefulness of synchrotron X-ray nanoprobe-based techniques X-ray fluorescence (XRF) imaging and X-ray absorption near edge structure (XANES) spectroscopy in the characterization of the elemental distribution and local atomic structure of single Co-implanted ZnO NWs.^{18,19} However, these techniques have not been applied so far to single NWs of ternary alloys. In this work, we have investigated MBE-grown $\text{In}_x\text{Ga}_{1-x}\text{N}$ NWs using the high spatial resolution provided by the X-ray nanoprobe. The axial and radial elemental distribution, and the short-range order of several single NWs have been analysed by means of nano-XRF imaging and nano-XANES spectroscopy.

II. EXPERIMENTAL DETAILS

$\text{In}_x\text{Ga}_{1-x}\text{N}$ NWs were grown on bare n-Si (111) substrates using a Veeco GEN II MBE-system. The *ex-situ* preparation of the substrate is described elsewhere.²⁰ The NWs were grown under nitrogen rich conditions required to obtain a NW morphology, with a growth time of 200 min. The substrate temperature (determined by pyrometry) and the Ga/(Ga + In) flux ratio used during the growth were 462 °C and 0.07, respectively. Single NWs were transferred to an Al-covered sapphire substrate having a gold grid prepared by lithography. The morphology of the NWs was investigated using a Zeiss Leo 1550 scanning electron microscope (SEM) operated at 20 kV. More details about the growth process and the identification of single NWs for their characterization can be found in Ref. 22. The XRF measurements were collected at the nanoimaging station ID22NI of the European Synchrotron Radiation Facility.²³ The X-ray beam was

^{a)}Electronic mail: seguraru@esrf.fr

focused by a pair of Kirkpatrick-Baez multilayer mirrors²⁴ providing a spot size of $55 \times 55 \text{ nm}^2$ with a flux of 10^{12} ph/s at 17 keV in pink beam mode ($\Delta E/E \sim 10^{-2}$), and $110 \times 105 \text{ nm}^2$ spot size with a flux of 10^{10} ph/s in monochromatic beam mode ($\Delta E/E \sim 10^{-4}$), as shown in Fig. 1. The XRF signal was detected at 15° with respect to the sample surface, using an energy dispersive silicon drift detector. The XRF spectra were fitted to quantify the elemental composition using the PYMCA program.²⁵ XANES data were recorded in XRF mode with an energy step size of 1 eV and integration times determined by the counting statistics. The data processing was performed using ATHENA.²⁶

III. EXPERIMENTAL RESULTS AND DISCUSSIONS

Figure 2(a) shows lateral and top view scanning electron microscopy images of the $\text{In}_x\text{Ga}_{1-x}\text{N}$ NWs on the Si (111) substrate. Typical heights and diameters of the NWs range between (400 to 950) nm, and (100 to 180) nm, respectively. X-ray diffraction measurements (not shown here) show that the NWs are well oriented along the [0001] direction of the wurtzite crystal structure. Several NWs exhibit the baseball bat shape, a typical morphology observed in InN NWs.²⁰ This characteristic helps to identify the upper and lower parts of single NWs after their transfer to the Al-covered substrate. There is a thin parasitic rough layer covering the substrate

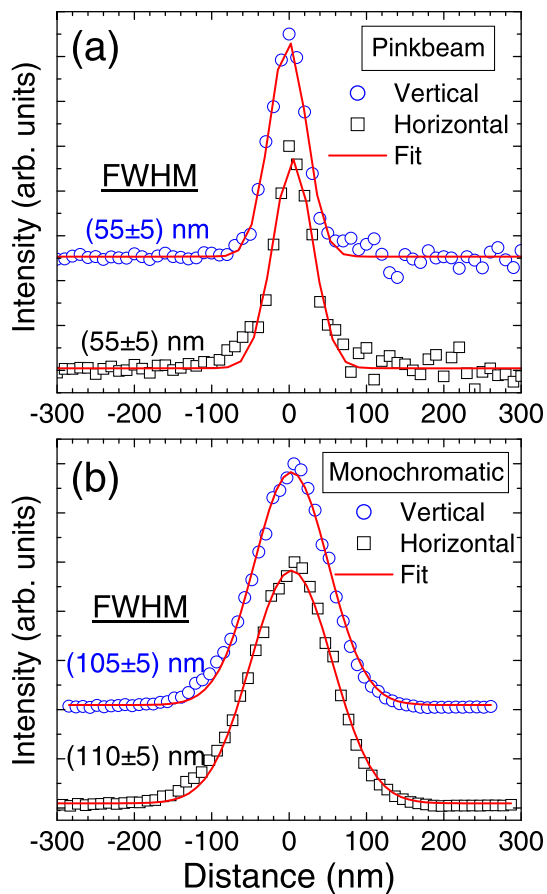


FIG. 1. Vertical (open circles) and horizontal (open squares) beam profiles of the focused (a) pink ($\Delta E/E \sim 10^{-2}$) and (b) monochromatic ($\Delta E/E \sim 10^{-4}$) X-ray beam.

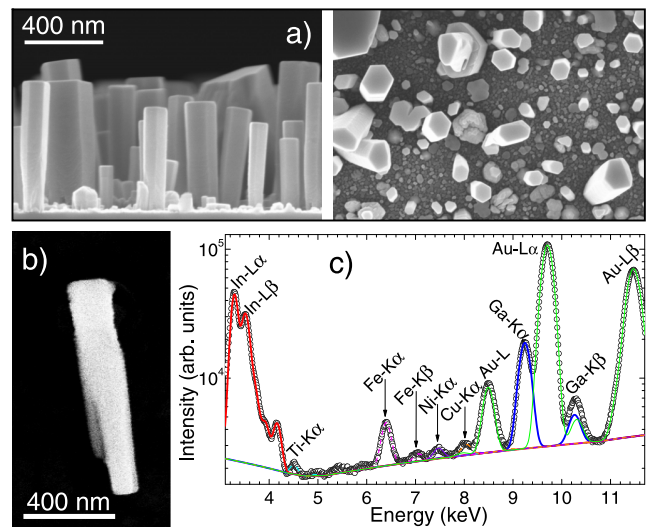


FIG. 2. (a) Lateral (left) and top (right) view SEM images of as-grown $\text{In}_x\text{Ga}_{1-x}\text{N}$ NWs on the Si (111) substrate. Heights and diameters of the NWs range between 400–950 nm and 100–180 nm, respectively. (b) SEM image of a representative $\text{In}_x\text{Ga}_{1-x}\text{N}$ NW studied here. (c) Average XRF spectrum of the full scanned area (open symbols) and fits obtained via PYMCA, indicating each elemental contribution.

surface which does not appear for pure InN NWs grown at the same temperature.²⁰ This parasitic layer is Ga-rich and appears as a consequence of the low growth temperature, which is around 170°C lower than the minimum temperature for the diffusion induced growth of GaN nanocolumns.²¹ Figure 2(b) shows the SEM image of one of the single $\text{In}_x\text{Ga}_{1-x}\text{N}$ NWs studied in this work. The NW length is ~ 940 nm and the diameter at the bottom (top) part is ~ 110 (180) nm. To examine the compositional homogeneity, we have scanned several single NWs, taking advantage of the high X-ray flux and high spatial resolution of ID22NI. The XRF maps were taken with a pixel size of $25 \times 25 \text{ nm}^2$ and an accumulation time of 1.5 s per pixel. Using the PYMCA program,²⁵ the average XRF spectrum was fitted to identify the different elements in the scanned area. The average spectrum obtained after a pixel by pixel sum and the corresponding fitting are shown in Fig. 2(c). Within the scanned area, apart from the In and Ga in the NW, the XRF signal from the Ar in the air, and the peaks associated with Au, Fe, Cu, Ni, and Ti are also observed.

To elucidate whether the elements observed in the scanned area are incorporated into the NW or not, the XRF spectrum of each pixel was fitted to build elemental distribution maps. Figure 3 shows the Au (a), Fe (b), Cu (c), Ni (d), In (e), and Ga (f) maps. The Au map exhibits a smooth spatial distribution without any correlation with the NW shape. The Au signal should come most likely from residual fractions of this element remaining on the substrate after the lithography process. On the other hand, Fe, Cu, Ni, and Ti (not shown) exhibit random distributions without any correlation with the NWs morphology. Therefore, the impurities are mostly in the Al layer deposited on top of the substrate, rather than incorporated into the NW. In the energy range explored and within our detection limit (down to 1 ppm for elements heavier than Ca), there is no evidence of

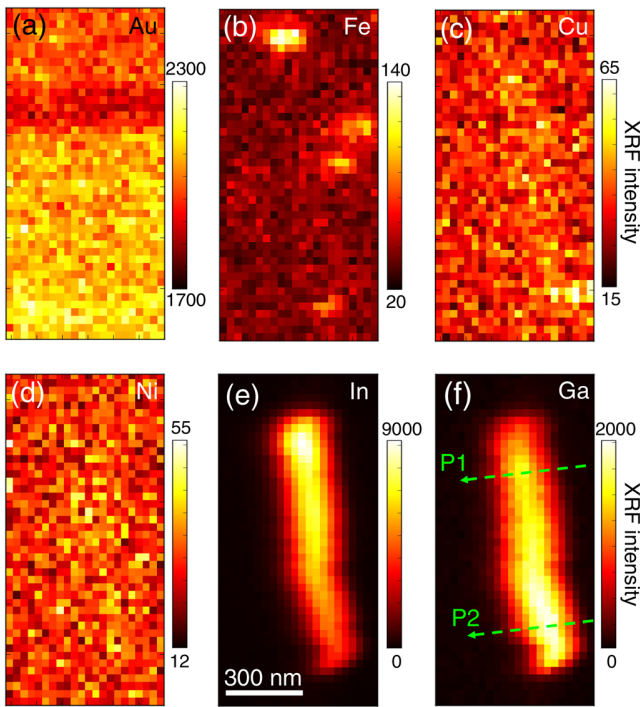


FIG. 3. Spatial distribution maps for (a) Au, (b) Fe, (c) Cu, (d) Ni, (e) In, and (f) Ga. The intensity ranges are indicated by their colour scale, where dark represents low and bright high photon counts. The XRF maps were taken with a pixel size of $25 \times 25 \text{ nm}^2$ and an accumulation time of 1.5 s per pixel.

unintentional doping in the NWs. Finally, while the In distribution reproduces the NW morphology very well, the Ga map suggests a non-uniform incorporation inside the single NWs. Based on the characteristic baseball bat shape of this NW, the Ga (In) concentration seems to be higher at the bottom (top) of the NW, as reported for other $\text{In}_x\text{Ga}_{1-x}\text{N}$ NWs.¹⁵ In general, when a monochromatic parallel beam is used to excite the characteristic X-rays of an element i within a matrix (neglecting enhancement effects due to an extra excitation of the element of interest by the characteristic radiation of other elements in the sample), the intensity of the X-ray fluorescent radiation is given by²⁷

$$I_i = \frac{I_0 \cdot G \cdot C_i \cdot \left(1 - e^{-\rho d \left[\frac{\mu(h\nu)}{\sin(\theta_1)} + \frac{\mu(E_i)}{\sin(\theta_2)} \right]} \right)}{\rho \left[\frac{\mu(h\nu)}{\sin(\theta_1)} + \frac{\mu(E_i)}{\sin(\theta_2)} \right]}, \quad (1)$$

where I_0 is the number of incoming photons, the factor G accounts for the XRF yield, solid angle, and detection efficiency, and C_i is the concentration of the element i in the material. d and ρ are the sample thickness and density, μ is the total mass attenuation coefficient, and E_i and $h\nu$ are the energies of the XRF and incoming radiation, respectively, while θ_1 and θ_2 are their respective angles relative to the sample surface. From this general expression, the Ga concentration calculated from the XRF spectra was 1.5 at. % at the bottom and 0.5 at. % at the top of the NW. These values are lower than the expected ones considering the Ga/(Ga + In) flux

ratio used during the growth was 0.07. Although In segregation is often reported in $\text{In}_x\text{Ga}_{1-x}\text{N}$ alloy,²⁸ our results show the same tendency for the Ga species in these NWs grown by MBE. This behaviour is due to a larger diffusion length for In than for Ga adatoms due to the low growth temperature, causing the observed decrease of the Ga content towards the top of the NWs. The almost negligible diffusion of Ga adatoms is also the origin of the Ga-rich thin parasitic rough layer covering the substrate surface, which was not observed for pure InN NWs.²⁹

To gain further insight into the elemental spatial distribution of the individual NW, Fig. 4 shows the radial In and Ga profiles across the single NW in the regions indicated by lines P1 (a) and P2 (b) in Fig. 3(f). For both regions, the profiles have Gaussian contours, originating from the convolution of the beam and the NW shapes. From Gaussian fits, along P1, we obtained full width at the half maximum (FWHM) values of (120 ± 2) for In and (130 ± 2) nm for Ga. Similarly, along P2, we obtain (110 ± 3) nm and (130 ± 4) nm for In and Ga profiles, respectively. Within the fitting error, the FWHM is smaller for In profiles than for Ga ones. The same feature has been observed in all the studied NWs, with only small differences between the FWHM values. This result would suggest the existence of a Ga-richer shell in the NWs, i.e., a tendency of Ga-species to accumulate in the near surface region of the NWs forming a self-assembled core-shell structure. Similar characteristics have been observed in MBE-grown Ga-rich $\text{In}_x\text{Ga}_{1-x}\text{N}$ by energy-dispersive X-ray spectroscopy.¹⁶ However, within the length scale of the beam size, we cannot confirm absolutely about the existence of such self-assembled heterostructure in our NWs.

The NWs morphology was examined by SEM after the XRF characterization to investigate any radiation induced damage. Figures 5(a) and 5(b) show the SEM images of two NWs after the nano-XRF analysis with a photon flux of about 10^{12} and 10^{11} ph/s, respectively. Figures 5(c) and 5(d) show the corresponding Ga fluorescence intensity maps of these two NWs. The NW studied using the higher X-ray flux exhibits partial amorphization reflected in the change of its

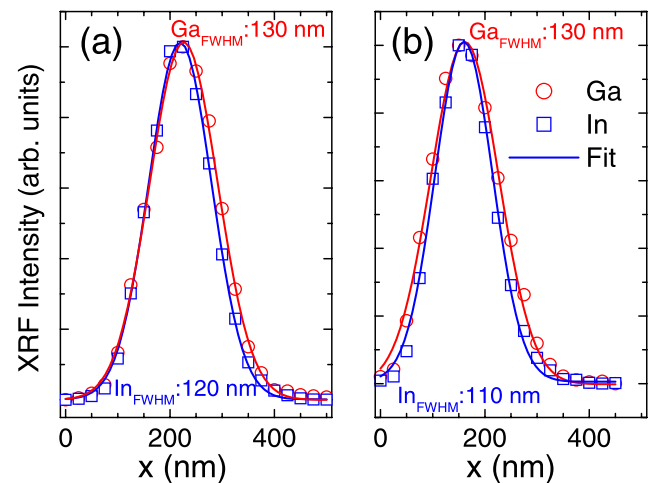


FIG. 4. Radial profiles across the single NW in the regions indicated by lines P1 (a) and P2 (b) in Fig. 3(f). Position zero corresponds to the arrow starting point.

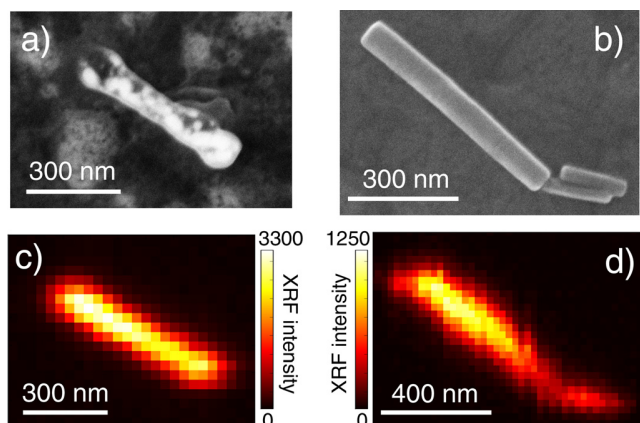


FIG. 5. SEM images of single NWs after the nano-XRF analysis with a photon flux of about 10^{12} (a) and 10^{11} ph/s (b), respectively. (c) and (d) The corresponding Ga fluorescence intensity maps of these two NWs.

morphology and corroborated by Raman spectroscopy (not shown here). On the other hand, the NW characterized with a lower dose does not show any sign of radiation damage neither in its morphology nor in its Raman spectrum. The detection of the XRF signal in Fig. 5(d) was improved by moving the silicon drift detector as close as possible to the sample, keeping always the deadtime below the limits of non-linear response. The former allows to have approximately the same signal-to-noise ratio with the same accumulation time as for those in the map shown in Fig. 5(c). In both cases, the inhomogeneous axial distribution of Ga is observed. Moreover, the radial profiles of both NWs (not shown) also showed FWHM values higher for Ga than for In profiles. This indicates that the inhomogeneous elemental distribution inside the single NWs is an intrinsic characteristic arising from the NWs growth process, and not from the X-ray beam.

In order to study the influence of the inhomogeneous axial elemental distribution on the local structure, XANES measurements around the In K-edge were performed at the bottom and top of the single NW shown in Fig. 3(b). In general, the K-edge XANES spectra probe the partial density of the empty states of the absorbing atoms. Thanks to the scalar product between the photon polarization and position of the electron vectors in the matrix element of the absorption cross section, a linearly polarized X-ray beam makes possible the investigation of the conduction band states distribution of a hexagonal structure separately in the ab and c plane of the crystal. In our experimental configuration, the c -axis of the NW was nearly perpendicular to the electric field vector of the linearly polarized synchrotron radiation. Therefore, our In K-edge XANES data are more sensitive to the symmetry of the ab -plane. Figure 6 displays the spectra acquired at the bottom (triangles) and top (circles) of the single NW. Furthermore, the XANES spectrum of a MBE-grown wurtzite InN layer (squares) acquired with the same experimental conditions as those used for the NW is included for comparison. In general, the features in the three spectra reflect the typical wurtzite structure of the InN lattice.³⁰ The NW spectra are quite similar between them, not reflecting the compositional variation found by nano-XRF imaging. They show

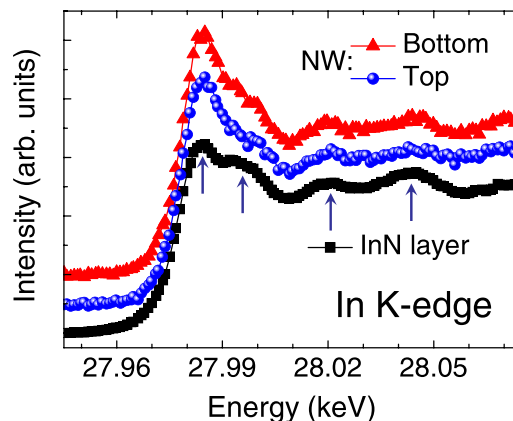


FIG. 6. XANES spectra acquired at the bottom (triangles) and top (circles) of the NW around the In K-edge. For comparison, the XANES spectra of a wurtzite InN layer is also included (squares).

all the XANES resonances in the layer spectrum (marked by arrows) at the same energy positions. This indicates that the tetrahedral structure is preserved around the absorbing In-atoms all along the NW. The detailed inspection reveals that the second, third, and fourth peaks are broader than those for the InN film. These spectral differences result from the lower order of symmetry of the structural unit in the NW. This suggests that the compositional modulation evidenced from the XRF analysis could be affecting the large-range order along the NW. However, the precise identification and quantification of such effects in the long-range order require further information. Finally, the first resonance in the NWs XANES spectra is stronger than in the InN film. The same behaviour has been observed in wurtzite GaN and AlN NWs, and was explained as due to a slight increase of the degree of localization of the cation p orbitals due to the confinement of the NW surfaces.³¹

IV. CONCLUSIONS

Single $\text{In}_x\text{Ga}_{1-x}\text{N}$ NWs grown by molecular beam epitaxy on Si (111) substrates were characterized by X-ray fluorescence nanoprobe. Ga and In elemental maps revealed an inhomogeneous elemental distribution along the single NWs, with a higher Ga concentration at the bottom of the NW. Radiation damage was ruled out as the origin of the inhomogeneous Ga maps, and therefore, it was suggested to be an intrinsic characteristic of the NWs arising from the growth process. Spatially resolved XANES data acquired around the In K-edge showed that the tetrahedral structure is preserved around the absorbing In-atoms all along the NW, and suggested that the compositional modulation in the NW affected its large-range order. Further experiments are required to precisely identify and quantify these effects in the long-range order of the NWs.

ACKNOWLEDGMENTS

The authors thank R. Tucoulou and P. Cloetens for their help with the experimental setup and I. Snirigeva for the

help with the SEM imaging. This work was partially supported by the NANOWIRING Marie Curie ITN (EU Project No. PITN-GA-2010-265073).

- ¹H. Lu, W. J. Schaff, J. Hwang, H. Wu, W. Yeo, A. Pharkya, and L. F. Eastman, *Appl. Phys. Lett.* **77**, 2548 (2000).
- ²H. Lu, W. J. Schaff, J. Hwang, H. Wu, G. Koley, and L. F. Eastman, *Appl. Phys. Lett.* **79**, 1489 (2001).
- ³V. Y. Davydov, A. A. Klochikhin, R. P. Seisyan, V. V. Emtsev, S. V. Ivanov, F. Bechstedt, J. Furthmüller, H. Harima, A. V. Mudryi, J. Aderhold, O. Semchinova, and J. Graul, *Phys. Status Solidi B* **229**, R1 (2002).
- ⁴J. Wu, W. Walukiewicz, K. M. Yu, J. W. Ager III, E. E. Haller, H. Lu, W. J. Schaff, Y. Saito, and Y. Nanishi, *Appl. Phys. Lett.* **80**, 3967 (2002).
- ⁵J. Wu, W. Walukiewicz, K. M. Yu, W. Shan, J. W. Ager III, E. E. Haller, H. Lu, W. J. Schaff, W. K. Metzger, and S. Kurtz, *J. Appl. Phys.* **94**, 6477 (2003).
- ⁶O. Jania, I. Ferguson, C. Honsberg, and S. Kurtz, *Appl. Phys. Lett.* **91**, 132117 (2007).
- ⁷Y. Narukawa, Y. Kawakami, M. Funato, S. Fujita, S. Fujita, and S. Nakamura, *Appl. Phys. Lett.* **70**, 981 (1997).
- ⁸Y.-L. Lai, C.-P. Liu, Y.-H. Lin, T.-H. Hsueh, R.-M. Lin, D.-Y. Lyu, Z.-X. Peng, and T.-Y. Lin, *Nanotechnology* **17**, 3734 (2006).
- ⁹F. Glas, *Phys. Rev. B* **74**, 121302(R) (2006).
- ¹⁰L. Cerutti, J. Ristić, S. Fernández-Garrido, E. Calleja, A. Trampert, K. H. Ploog, S. Lazic, and J. M. Calleja, *Appl. Phys. Lett.* **88**, 213114 (2006).
- ¹¹R. Songmuang, O. Landr, and B. Daudin, *Appl. Phys. Lett.* **91**, 251902 (2007).
- ¹²T. Kuykendall, P. Ulrich, S. Aloni, and P. Yang, *Nature Mater.* **6**, 951 (2007).
- ¹³M. Keplinger, T. Martensson, J. Stangl, E. Wintersberger, B. Mandl, D. Kriegner, V. Holy, G. Bauer, K. Deppert, and L. Samuelson, *Nano Lett.* **9**, 1877 (2009).
- ¹⁴M. Heiss, B. Ketterer, E. Uccelli, J. R. Morante, J. Arbiol, and A. Fontcuberta i Morral, *Nanotechnology* **22**, 195601 (2011).
- ¹⁵T. Kehagias, *Physica E* **42**, 2197 (2010).
- ¹⁶G. Tourbot, C. Bougerol, A. Grenier, M. Den Hertog, D. Sam-Giao, D. Cooper, P. Gilet, B. Gayral, and B. Daudin, *Nanotechnology* **22**, 075601 (2011).
- ¹⁷K. D. Goodman, V. V. Protasenko, J. Verma, T. H. Kosel, H. G. Xing, and D. Jena, *J. Appl. Phys.* **109**, 084336 (2011).
- ¹⁸M. H. Chu, J. Segura-Ruiz, G. Martínez-Criado, P. Cloetens, I. Snigireva, S. Geburt, and C. Ronning, *Phys. Status Solidi (RRL)* **5**, 283 (2011).
- ¹⁹J. Segura-Ruiz, G. Martínez-Criado, M. H. Chu, S. Geburt, and C. Ronning, *Nano Lett.* **11**, 5322 (2011).
- ²⁰J. Segura-Ruiz, N. Garro, A. Cantarero, C. Denker, J. Malindretos, and A. Rizzi, *Phys. Rev. B* **79**, 115305 (2009).
- ²¹J. Segura-Ruiz, G. Martínez-Criado, J. A. Sans, R. Tucoulou, P. Cloetens, I. Snigireva, C. Denker, J. Malindretos, A. Rizzi, M. Gomez-Gomez, N. Garro, and A. Cantarero, *Phys. Status Solidi (RRL)* **5**, 95 (2011).
- ²²G. Martínez-Criado, R. Tucoulou, P. Cloetens, P. Bleuuet, S. Bohic, J. Cauzig, I. Kieffer, E. Kosior, S. Labouré, S. Petitgirard, A. Rack, J. A. Sans, J. Segura-Ruiz, H. Suhonen, J. Susini, and J. Villanova, *J. Synchrotron Radiat.* **19**, 10 (2012).
- ²³R. Barret, R. Baker, P. Cloetens, Y. Dabin, C. Morawe, A. Rommeveaux, H. Suhonen, R. Tucoulou, and L. Zhang, *Proc. SPIE* **8139**, 813904 (2011).
- ²⁴V. A. Solé, E. Papillon, M. Cotte, Ph. Walter, and J. Susini, *Spectrochim. Acta B* **62**, 63 (2007).
- ²⁵B. Ravel and M. Newville, *J. Synchrotron Radiat.* **12**, 537 (2005).
- ²⁶R. Meijers, Ph.D. dissertation, Rheinisch-Westfälische Technische Hochschule Aachen, 2007.
- ²⁷*Handbook of X-Ray Spectrometry, Practical Spectroscopy Series*, Vol. 29, edited by R. E. Van Grieken and A. A. Markowicz (Marcel Dekker, New York, 2002).
- ²⁸A. Kar, D. Alexson, M. Dutta, and M. A. Stroschio, *J. Appl. Phys.* **104**, 073502 (2008).
- ²⁹C. Denker, Ph.D. dissertation, Georg-August-Universität Göttingen, 2012.
- ³⁰M. J. Ward, W. Q. Han, and T. K. Sham, *J. Phys. Chem. C* **115**, 20507 (2011).
- ³¹C. W. Pao, P. D. Babu, H. M. Tsai, J. W. Chiou, S. C. Ray, S. C. Yang, F. Z. Chien, W. F. Pong, M.-H. Tsai, C. W. Hsu, L. C. Chen, C. C. Chen, K. H. Chen, H.-J. Lin, J. F. Lee, and J. H. Guo, *Appl. Phys. Lett.* **88**, 223113 (2006).

Appendix B

Radial composition of single InGaN nanowires: a combined study by EDX, Raman spectroscopy, and X-ray diffraction

M. Gómez-Gómez, N. Garro, ¹, J. Segura-Ruiz, G. Martínez-Criado, M. H. Chu, A. Cantarero¹, C. Denker, J. Malindretos, and A. Rizzi

Radial composition of single InGaN nanowires: a combined study by EDX, Raman spectroscopy, and X-ray diffraction

M. Gómez-Gómez¹, N. Garro^{*1}, J. Segura-Ruiz^{**2}, G. Martínez-Criado², M. H. Chu², A. Cantarero¹, C. Denker³, J. Malindretos³, and A. Rizzi³

¹ Institut de Ciència dels Materials, Universitat de València, 46980 Paterna (València), Spain

² European Synchrotron Radiation Facility, Experiments Division, 38043 Grenoble, France

³ IV. Physikalisches Institut, Georg-August-Universität Göttingen, 37077 Göttingen, Germany

Received 31 May 2013, revised 19 June 2013, accepted 19 June 2013

Published online 25 June 2013

Keywords III-nitride semiconductors, compound semiconductors, nanowires, Raman spectroscopy, X-ray diffraction, EDX

* Corresponding author: e-mail nuria.garro@uv.es, Phone: +34 963543601, Fax: +34 963543633

** e-mail seguraru@esrf.fr, Phone: +33 438881906, Fax: +33 476882906

The radial alloy distribution of $\text{In}_x\text{Ga}_{1-x}\text{N}$ nanowires grown by plasma-assisted molecular beam epitaxy has been investigated by three different techniques with nanometric spatial resolution and capability to study single nanowires. Energy-dispersive X-ray spectroscopy radial line-scans revealed a gradient in the alloy composition of individual nanowires. Resonant Raman scattering and spatially resolved X-ray diffraction showed the existence of three distinctive regions with

different alloy composition. The combination of the three techniques provides robust evidence of the spontaneous formation of a core–shell structure with a thin Ga-rich shell wrapping an In-rich core at the bottom part of the nanowires. This composition-modulated nanostructure offers an attractive way to explore new device concepts in fully epitaxial nanowire-based solar cells.

© 2013 WILEY-VCH Verlag GmbH & Co. KGaA, Weinheim

1 Introduction Core–shell nanowires (NWs) based on $\text{In}_x\text{Ga}_{1-x}\text{N}$ are ideal candidates for light-harvesting devices thanks to the disentanglement of light absorption from radial collection of photogenerated carriers and to the perfect match between the solar spectrum and the ternary alloy direct band-gap [1, 2]. In the last few years, free-standing $\text{In}_x\text{Ga}_{1-x}\text{N}$ NWs have been grown successfully by molecular beam epitaxy (MBE) [3–9]. Despite of their improved crystalline quality, controlling the alloy composition has proven to be very difficult. Alloy fluctuations limit the energy tunability and give rise to large inhomogeneous broadenings, which are common features of $\text{In}_x\text{Ga}_{1-x}\text{N}$ NW emission [5, 6, 9]. Recent reports on the alloy distribution of individual $\text{In}_x\text{Ga}_{1-x}\text{N}$ NWs have evidenced variations in the composition not only along the NW axis but also across its radius [4–7]. These studies rely on two scanning nanoprobe, energy dispersive X-ray spectroscopy (EDX) and synchrotron-based X-ray fluores-

cence, which provide the average chemical composition of the excited volume with nanometric spatial resolution. Obtaining quantitative estimates of the radial alloy distribution is, nevertheless, particularly delicate, since the chemical composition and the sample thickness may vary simultaneously [10]. Other techniques, such as photoluminescence (PL), Raman scattering, and X-ray diffraction (XRD), are able to separate the contributions of regions with different alloy compositions within the probed volume to the detriment of the spatial resolution.

In this Letter, we show how the variation of the alloy composition along the radius of single $\text{In}_x\text{Ga}_{1-x}\text{N}$ NWs can be fully determined by combining three different techniques: EDX, resonant Raman scattering (RRS), and synchrotron-based XRD. All three have spatial resolution on the nanoscale and are able to resolve the non-intentional formation of a core–shell structure within single NWs.

2 Sample description and experimental details

$\text{In}_x\text{Ga}_{1-x}\text{N}$ NWs were grown on a rotating n-type Si(111) substrate by catalyst-free plasma-assisted MBE. A fixed Ga supply (defined as the Ga/(In + Ga) flux ratio) of 0.5, a substrate temperature of 550 °C, and nitrogen-rich conditions were kept during the NW growth time (200 min). A statistically meaningful number of single NWs were isolated and investigated by the three different techniques employed in this work. The average length and diameter of the NWs investigated were 1200 and 200 nm, respectively.

The EDX measurements were carried out in a transmission electron microscope (TEM) with a Schottky field emission electron gun operated at 200 kV. The sample holder was tilted by 30° with respect to the electron beam in order to optimize the X-ray fluorescence detection. The spatial resolution is given by the 3 nm diameter of the electron beam. The μ -RRS measurements were performed in backscattering geometry with the light from an Ar/Kr laser focused onto a 1 μm diameter spot. The nanoimaging station ID22NI of the European Synchrotron Radiation Facility (ESRF) hosted the nano-XRD measurements. The monochromatic X-ray beam was focused by a pair of Kirkpatrick–Baez multilayer coated Si mirrors providing a spot size of $150 \times 150 \text{ nm}^2$ with a photon flux of about 10^{10} ph/s at 28 keV ($\Delta E/E = 10^{-4}$).

3 Results

The elemental composition of individual $\text{In}_x\text{Ga}_{1-x}\text{N}$ NWs has been examined by EDX. The intensity profiles of the Ga K and the In L fluorescence lines obtained along the radial scan of a single NW are shown in Fig. 1(a). The trajectory of the EDX line-scan across the cross-section at the bottom of the NW is shown in the inset TEM micrograph and labeled as B. While the intensity of the In fluorescence appears to follow the cross-section thickness of the NW, the profile of the Ga line is lower in the central part and increases continuously towards the lateral surfaces of the NW. Such a profile has been consistently reproduced at different cross-sections along the NW axis and in all the NWs investigated, independently of their orientation with respect to the detector. Quantitative values for the alloy composition in the NW were obtained using the Cliff–Lorimer method [11] with the k -factors provided by the commercial software of the instrument. The relative uncertainty of the elemental concentrations is limited by the counting statistics and can be as high as 35% in the points closer to the lateral surfaces of the NWs, where the probed volume is reduced considerably [12].

The profile of the Ga concentration shown in Fig. 1(b) suggests the existence of a core–shell structure. Therefore, such a distribution should be taken into account in order to estimate the Ga content of the core and the shell regions. As a first approximation, a cylindrical NW with a sharp transition in the alloy composition between a core, of thickness t_1 and Ga concentration C_{Ga_1} , and two consecutive shells, of thicknesses t_2 and t_3 and concentrations C_{Ga_2} and C_{Ga_3} , has been assumed. This choice is motivated by the observation of three different contributions to the RRS

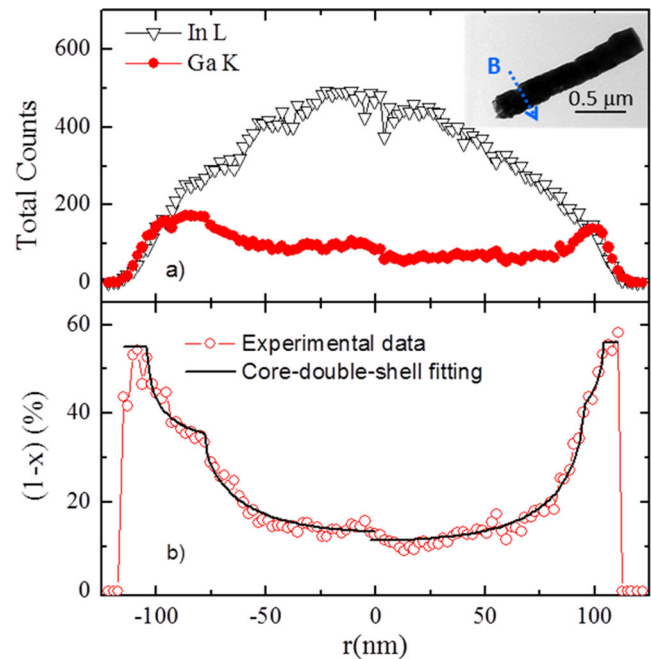


Figure 1 (a) Integrated fluorescence intensity of the Ga K and In L lines along the bottom cross-section, B, depicted in the TEM micrograph. (b) Ga content profile along B together with the best fit of the experimental profile (solid line) assuming a sharp core–double-shell NW.

and XRD spectra, as will be discussed later in this paper. The average Ga concentration of the EDX cross-section as a function of the radial coordinate, r , can be calculated as

$$(1-x)(r) = \frac{I_{\text{Ga}}(r)}{I_{\text{Ga}}(r) + I_{\text{In}}(r)}, \quad (1)$$

where, according to the core–double-shell model proposed in this work, the intensity of each element i at a given position, $I_i(r)$, is proportional to

$$\begin{aligned} I_i(r) &\propto C_{i3} \sqrt{(t_1 + t_2 + t_3)^2 - r^2} && \text{for } r > t_1 + t_2, \\ I_i(r) &\propto C_{i3} (\sqrt{(t_1 + t_2 + t_3)^2 - r^2} - \sqrt{(t_1 + t_2)^2 - r^2}) \\ &\quad + C_{i2} \sqrt{(t_1 + t_2)^2 - r^2} && \text{for } t_1 + t_2 > r > t_1, \\ I_i(r) &\propto C_{i3} (\sqrt{(t_1 + t_2 + t_3)^2 - r^2} - \sqrt{(t_1 + t_2)^2 - r^2}) \\ &\quad + C_{i2} (\sqrt{(t_1 + t_2)^2 - r^2} - \sqrt{t_1^2 - r^2}) + C_{i1} \sqrt{t_1^2 - r^2} && \text{for } t_1 > r. \end{aligned} \quad (2)$$

The experimental EDX profile has been fitted with Eq. (1) and the elemental intensities of Eq. (2). Due to the slight asymmetry, the right and left side have been fitted independently. This simple model succeeds in reproducing the experimental profiles for both sides as shown in Fig. 1(b). The average Ga concentrations and core and shell thicknesses obtained from the best fits are contained in Table 1 with their corresponding fitting errors. These results point

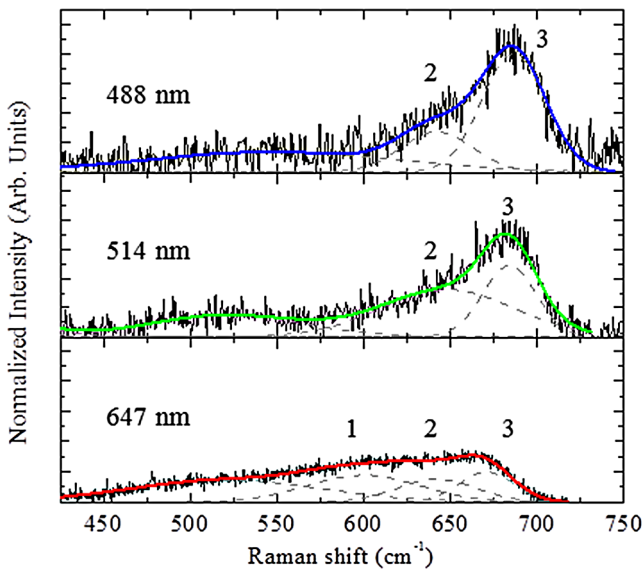


Figure 2 RRS spectra of a single $\text{In}_x\text{Ga}_{1-x}\text{N}$ NW for three different excitation wavelengths. The spectra are normalized with respect to the intensity of peak centred at 500 cm^{-1} and attributed to the non-polar E_{2h} mode. All measurements were carried out at room temperature in backscattering geometry, with the excitation entering the NW through its lateral surface.

out that a spontaneous phase separation occurs during the growth process.

In order to obtain direct prove of the core-shell structure, the RRS spectra of single NWs have been measured as a function of the excitation wavelength. In these experiments, the whole NW volume was illuminated and the regions with different alloy compositions appeared as separated peaks in the RRS spectra. Three representative spectra are shown in Fig. 2. Several weak peaks are resolved below 586 cm^{-1} that correspond to the E_{2h} and the transversal optical modes of the alloy. At higher frequencies, the longitudinal optical (LO) modes appear as a broader band that can be decomposed into two or three Gaussian peaks, depending on the excitation wavelength. The central frequency and the linewidths of these peaks reflect the alloy composition and the strain fields present in these heterogeneous NWs [13]. On the other hand, the intensity of the RRS peaks does not correlate with the alloy volume but with the proximity to an electronic resonance. The two peaks at higher frequencies, labelled 2 and 3 in Fig. 2, become more intense and blue-shift slightly with increasing excitation energy indicating the selective resonant excitation of regions with different Ga content within the axial and/or radial direction of each single NW.

Three regions with distinctive Ga concentration are derived from the RRS spectra, as gathered in Table 1. These results have been obtained assuming that the peaks correspond to $A_1(\text{LO})$ modes and after correcting for the strain-induced Raman shifts due to the core-shell structure of these NWs. The strain fields have been estimated by extending the analytical model developed by Hestroffer et al.

Table 1 Ga content, C_{Ga} , of the three different regions identified in the $\text{In}_x\text{Ga}_{1-x}\text{N}$ NWs derived from the different techniques. The RRS and XRD results have been corrected for the strain fields in the different regions of the NW. The Ga contents and thicknesses resulting from the analysis of the EDX radial profile are accompanied by the errors of the fitting function.

region	t_i (nm)	$C_{\text{Ga}_i}^{\text{EDX}}$ (%)	$C_{\text{Ga}_i}^{\text{RRS}}$ (%) [*]	$C_{\text{Ga}_i}^{\text{XRD}}$ (%)
1 (core)	86 ± 4	3 ± 3	0	2
2 (inner shell)	17 ± 4	30 ± 7	40	11
3 (outer shell)	16 ± 4	55 ± 5	75	72

^{*} Obtained from the spectra for 647 nm (peaks 1 and 2) and 514 nm (peak 3) excitations.

[14] to the case of a core-double-shell NW with the Ga contents and thicknesses deduced from the EDX analysis. This model assumes that the NW undergoes elastic relaxation and that the strain is given by the lattice mismatch between the different regions, weighted by their relative thickness and elastic constants. The lattice parameters, elastic constants, and phonon deformation potential of the alloys have been obtained applying the Vegard's law to those of the binary compounds [15, 16]. The calculated values of the dominant strain component, ε_{zz} (z being parallel to the NW axis and thus to the wurtzite c -axis), are -2.5% , 0.5% , and 2.2% which induce Raman shifts of 15 cm^{-1} , -3 cm^{-1} , and -17 cm^{-1} for the core and the two consecutive shells of the NW, respectively.

Finally, XRD measurements were carried out at the ESRF, combining the structural selectivity of this technique and sub-micron spatial resolution. Thus single $\text{In}_x\text{Ga}_{1-x}\text{N}$ NWs could be scanned along their axis. Figure 3(a) and (b) show the CCD image and the integrated 2θ spectrum of the (200) reflection obtained from the bottom part of a single NW, respectively. Three peaks can be identified in the pattern corresponding to regions with different Ga composition. If the $\text{In}_x\text{Ga}_{1-x}\text{N}$ NWs have a strained wurtzite structure, an average composition could be determined from each peak by means of the Vegard's law once the strain has been corrected theoretically, as described previously.

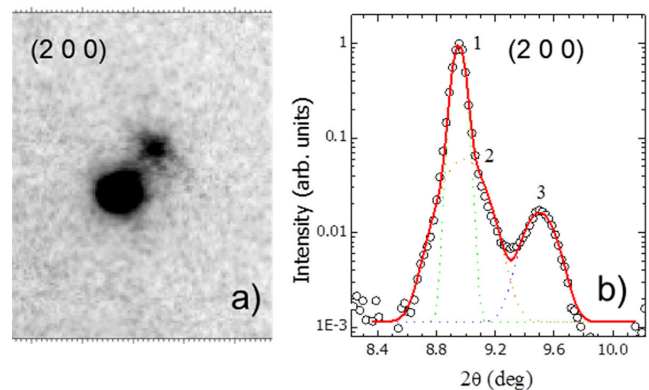


Figure 3 (a) CCD image of the (002) XRD reflection collected from the bottom part of a single NW. (b) 2θ spectrum obtained after integration of the CCD image.

The spectrum is dominated by the peak, labeled as 1, of a highly In-rich alloy. The lower intensities and larger linewidths of the secondary peaks, 2 and 3, reflect a more inhomogeneous composition and/or poorer crystal quality of the Ga-rich zone. The Ga contents derived from XRD are also gathered in Table 1.

The techniques employed in this study lead to different estimations for the Ga content of three distinctive regions within individual NWs, as summarized in Table 1. All three techniques agree on the existence of a first region close to pure InN which, according to its intensity in the XRD spectrum and to the EDX profile, should take most of the NW volume and correspond to the NW core. There is also good quantitative agreement on the Ga content of region 3 deduced from RRS and XRD, identified as the outer shell of the NW in the EDX profile. The main differences appear with the EDX value, which is the least reliable of the three measurements due to the reduction of the signal-to-noise ratio in the outer shell. Even though the thickness of the outer shell is rather small, its Raman signal gets resonantly enhanced by the 514 nm laser excitation. This wavelength matches the band-gap of an $\text{In}_x\text{Ga}_{1-x}\text{N}$ alloy with $1-x=0.7$ [2], in good agreement with the concentrations estimated by the three techniques. Finally, the Ga concentration in the transition region between the core and the outer shell, referred to as inner shell, presents more variations. The inner shell was introduced in the model of the EDX profiles and its contribution was also necessary in order to fit the RRS and XRD spectra. However, this appears as a broader peak mingled with the rest of the contributions and not as a distinctive peak in neither of the latter spectra. Therefore, this intermediate region is likely to present a smooth gradient of concentrations, which could also explain the difficulty in quantifying it by the current techniques.

In conclusion, the combination of three powerful techniques has provided sufficient chemical and spatial resolution as to resolve a core-shell structure spontaneously forming in the bottom part of $\text{In}_x\text{Ga}_{1-x}\text{N}$ NWs.

Acknowledgements This work has been supported by the European Union through the Grant Agreement No. 265073-NANOWIRING of the Seventh Framework Program and by projects MAT2012-33483 and GICSERV NGG-121 of the Spanish Ministry of Science.

References

- [1] B. Z. Tian, X. L. Zheng, T. J. Kempa, Y. Fang, N. F. Yu, G. H. Yu, J. L. Huang, and C. M. Lieber, *Nature* **449**, 885 (2007).
- [2] J. Wu, W. Walukiewicz, K. M. Yu, W. Shan, J. W. Ager III, E. E. Haller, H. Lu, W. J. Schaff, W. K. Metzger, and S. Kurtz, *J. Appl. Phys.* **94**, 6477 (2003).
- [3] A. P. Vajpeyi, A. O. Ajagunna, K. Tsagaraki, M. Androulidaki, and A. Georgakilas, *Nanotechnology* **20**, 325605 (2009).
- [4] T. Kehagias, *Physica E* **42**, 2197 (2010).
- [5] K. D. Goodman, V. V. Protasenko, J. Verma, T. H. Kosel, H. G. Xing, and D. Jena, *J. Appl. Phys.* **109**, 084336 (2011).
- [6] G. Tourbot, C. Bougerol, A. Grenier, M. Den Hertog, D. Sam-Giao, D. Cooper, P. Gilet, B. Gayral, and B. Daudin, *Nanotechnology* **22**, 075601 (2011).
- [7] J. Segura-Ruiz, G. Martínez-Criado, J. A. Sans, R. Tucoulou, P. Cloetens, I. Snigireva, C. Denker, J. Malindretos, A. Rizzi, M. Gómez-Gómez, N. Garro, and A. Cantarero, *Phys. Status Solidi RRL* **5**, 95 (2011).
- [8] F. Limbach, T. Gotschke, T. Stoica, R. Calarco, E. Sutter, J. Ciston, R. Cusco, L. Artus, S. Kremling, S. Höfling, L. Worschech, and D. Grützmacher, *J. Appl. Phys.* **109**, 014309 (2011).
- [9] S. Albert, A. Bengoechea-Encabo, P. Lefebvre, M. A. Sanchez-Garcia, E. Calleja, U. Jahn, and A. Trampert, *Appl. Phys. Lett.* **99**, 131108 (2011).
- [10] C. D. Bell, Y. Wu, C. J. Barrelet, S. Gradeak, J. Xiang, B. P. Timko, and C. M. Lieber, *Microsc. Res. Techn.* **64**, 373 (2004).
- [11] G. W. Lorimer, *Mineral. Mag.* **51**, 49 (1987).
- [12] M. Gómez-Gómez, N. Garro, J. Segura-Ruiz, G. Martínez-Criado, A. Cantarero, H. T. Mengistu, A. Garcia-Cristobal, S. Murcia-Mascaros, C. Denker, J. Malindretos, and A. Rizzi, to be published (2013).
- [13] S. Hernández, R. Cuscó, D. Pastor, L. Artús, K. P. O'Donnell, R. W. Martin, I. M. Watson, Y. Nanishi, and E. Calleja, *J. Appl. Phys.* **98**, 013511 (2005).
- [14] K. Hestroffer, R. Mata, D. Camacho, C. Leclere G. Tourbot, Y. M. Niquet, A. Cros, C. Bougerol, H. Renevier, and B. Daudin, *Nanotechnology* **21**, 415702 (2010).
- [15] A. F. Wright, *J. Appl. Phys.* **82**, 2833 (1997).
- [16] F. Demangeot, J. Frandon, M. A. Renucci, O. Briot, B. Gil, and R. L. Aulombard, *Solid State Commun.* **207**, 100 (1996).